Constraining Non-Standard Neutrino Interactions and Estimating Future Neutrino-Magnetic-Moment Sensitivity With COHERENT

by

Gleb Sinev

Department of Physics
Duke University

Date: ______________________________

Approved:

____

Kate Scholberg, Advisor

____

Joshua Socolar

____

Mark Kruse

____

Shailesh Chandrasekharan

____

Christopher Walter

Dissertation submitted in partial fulfillment of the
requirements for the degree of Doctor of Philosophy
in the Department of Physics
in the Graduate School of
Duke University

2020

ABSTRACT

Constraining Non-Standard Neutrino Interactions and Estimating Future Neutrino-Magnetic-Moment Sensitivity With COHERENT

by

Gleb Sinev

Department of Physics
Duke University

Date: ______________________
Approved:

____

Kate Scholberg, Advisor

____
Joshua Socolar

____
Mark Kruse

____
Shailesh Chandrasekharan

____
Christopher Walter

An abstract of a dissertation submitted in partial fulfillment of the
requirements for the degree of Doctor of Philosophy
in the Department of Physics
in the Graduate School of
Duke University

2020

Abstract

Neutrinos represent a rich field of physics that contains many theoretical problems that are yet to be solved and experimental results hinting at physics beyond the standard model (BSM) of particle physics. An experiment studying neutrino physics and that is the source of the data used in the studies presented here is COHERENT. Its primary goals are to measure and characterize coherent elastic neutrino-nucleus scattering (CEνNS). Studying CEνNS, a standard-model process, provides a direct way to constrain BSM theories. The area of neutrino physics that is primarily investigated in this work is non-standard neutrino interactions (NSI). I use the data taken by the CsI and CENNS-10 detectors of the COHERENT experiment to improve the constraint on the ϵ_{ee}^{dV} and ϵ_{ee}^{uV} NSI couplings. In addition to combining the data of those detectors, I use the Feldman-Cousins technique to improve the NSI limit, resulting in two bands of allowed couplings that together are 1.2 times narrower than the original COHERENT limit [A$^+$17c]. Multiple future improvements are discussed.

Another topic investigated here is non-zero neutrino magnetic moments, that, if measured, would point to BSM physics. I estimate the sensitivity of the future COHERENT program to μ_{ν_μ} by minimizing the likelihood function of observing nuclear recoils due to that neutrino magnetic moment in the COHERENT Ge detector. The obtained predicted sensitivity is $\mu_{\nu_\mu} < 8 \cdot 10^{-10} \mu_B$, which is not as strong as indirect limits, but is similar to existing direct constraints.

Contents

List of Figures

List of Tables

Acknowledgements

I am extremely grateful to my advisor, Kate Scholberg, for guiding me all the way from joining the program to my graduation. She has provided me with many opportunities to contribute to interesting and varied projects, learn a great amount about different aspects of experimental physics, and allowed a lot of freedom to pursue whatever I am interested in.

I also would like to thank my advisory committee, Josh Socolar, Shailesh Chandrasekharan, Mark Kruse, Chris Walter, for giving me valuable feedback and overseeing my journey from before I passed my preliminary examination through my thesis defense, and attending the defense despite multiple postponements and ending up in a situation where the only option was to hold it remotely.

I am grateful to the COHERENT collaboration for allowing me to use COHERENT data in my analyses and providing me with many options for exciting research and interactions with other physicists. I particularly want to thank Yuri Efremenko, without whom I would not have met my advisor and joined the Duke Physics department, and who helped me many times with great advice. Phil Barbeau and his students have been excellent to work with, and I am grateful for the opportunity to have performed multiple studies and tasks for the collaboration with them.

The COHERENT data used as input in this work were provided by Bjorn Scholz, Grayson Rich, Rex Tayloe, Jacob Zettlemoyer, Dmitry Rudik, as well as other members of the COHERENT CsI and CENNS-10 groups.

Oak Ridge National Laboratory has been a place I enjoyed visiting, its staff are outstanding and they have been an impressive host for many COHERENT meetings. In addition to hosting COHERENT, Oak Ridge has also provided valuable resources that I used in my work. Jason Newby has also been a great collaborator and Oak

Ridge representative, who provided a lot of help with using the laboratory's resources.

The first three years of being a Duke student, I primarily worked on the DUNE experiment and, even though I do not discuss my DUNE research here, I learned a great deal doing that and have very warm memories of being a part of the collaboration. That experience affected me tremendously and I hope that I have brought some of that useful expertise to COHERENT. I am looking forward to doing research with them again in several months.

Duke has been an amazing place to be a part of. I enjoyed my life here too much: from the incredible nature that the Piedmont region of North Carolina has to all the opportunities that Duke and the Research Triangle offer.

I am particularly glad to have met and spent a great amount of time with the Duke Physics students, with many of whom we went through a lot. Some of that was the tough physics courses in the first several years. However, the harder the courses were, the more I usually enjoyed them and now remember fondly. In addition, that allowed me to interact with many excellent instructors that I feel incredibly lucky to have known.

The Physics department has also been a superb place to work. I have been provided with a powerful workstation that I wrote and ran most of my analysis code on, and the computer grid was also very useful early on (and I definitely should have used more of it). The department made sure that I always had what I needed and have been very responsive. I specifically would like to thank Jenni Solis, the HEP administrative assistant, who always made sure that all our work trips were timely reimbursed and anything research-related is taken care of; Jimmy Dorff and Barry Wilson, the Physics computing staff, who promptly solved any computing issues I had and were a lot of fun to talk to about computer-related topics; Nancy Morgans and Katherine Siler, the former and current assistants to the director of graduate

studies, who made all graduate-school-related business much more straightforward than it would have been otherwise and helped organize our graduate-student life.

Finally, I am very grateful to the Duke Neutrino Group for having me as their member for this many years. My most important interactions were the ones I had in this group and I learned most from its other members. In addition to Kate being the excellent advisor she is, I learned a lot from being in meetings with Chris Walter, and was quite sad when our Neutrino and Cosmology Group became too large and had to split, since I greatly enjoyed learning about observational cosmology and having Chris providing feedback and his expertise to our part of the group. Despite that, I am certain that the new Duke Cosmology Group is an excellent addition to the Duke Physics Department and I am excited about their current and future research.

Our group has had many outstanding postdoctoral associates since I joined it. Alex Himmel probably taught me most about doing physics research and working as a member of a large collaboration. I still regret not following his advice enough and have been trying to pass his insights to other students working in the field of neutrino physics.

Mayra Cervantes was great to be around and work with. She started, with the help of Oak Ridge, the COHERENT data-monitoring system that I inherited and have been developing since she left. She also provided an interesting perspective of transitioning to working in industry, even though I still wish to keep working in academia.

Dan Pershey is a person without whom this work would be significantly harder. In less than two years, he has become an extremely valuable member of the COHERENT collaboration and our Neutrino group, proving to be a master of statistical analysis and possessing formidable physical intuition and ability to learn. He has been a great help elucidating how statistics works and overseeing all of the results presented here.

Certainly I cannot leave out other Duke Neutrino and Cosmology students that I got to know in the past seven years. They made my life at Duke much more enjoyable and helped me in many ways. It has been particularly fun to exchange our physics expertise that we have been gathering being students here.

Chapter 1

Introduction

The Standard Model of Particle Physics (SM) has been very successful in predicting experimental results for many decades. Despite that, a number of measurements exist that can not be fully explained by the SM.

Neutrino physics provides multiple examples of such discrepancies. Even neutrino masses are not included in the SM, in spite of being known to be non-zero since the discovery of neutrino oscillations in the nineties. One of the reasons for that has to be the difficulty in studying these particles due to their barely interacting with matter. However, nowadays, experiments specifically designed for detecting neutrinos observe them in large quantities, rapidly increasing our knowledge of neutrino physics. Some types of neutrino interactions are very well studied, while many others are still poorly known with no experimental data available.

Coherent elastic neutrino-nucleus scattering (CEνNS) [Fre74] was predicted over four decades ago, but is only entering its experimental era with the first observation being performed in 2017 [A$^+$17c]. Thus, this scattering has not yet been well constrained experimentally and could provide significant deviations from the SM.

COHERENT [A$^+$a] is a leading experiment in the field of CEνNS detection and characterization, producing the first CEνNS measurement three years ago [A$^+$17c] and currently releasing results from its second CEνNS detector [A$^+$20b].

This work attempts to constrain neutrino interactions using the COHERENT experiment's data and to study COHERENT's future capability to measure non-zero neutrino magnetic moments. I present the background information and my findings here.

First, I briefly describe the relevant physics in Chapter 2. This chapter includes a discussion of CEνNS, NSI, and neutrino magnetic moments. Current limits and the motivation for performing the work presented here are also included in that chapter.

In Chapter 3, I write about the COHERENT experiment. Particularly emphasized are the detectors that produced the data used for the studies in this work, CsI and CENNS-10, and the source of the neutrino used, Spallation Neutron Source (SNS). In addition, other COHERENT detectors, both those currently taking data and the ones still being designed or constructed, are mentioned.

Chapter 4 describes the procedures used in COHERENT to acquire data, as well as how those data are prepared for use in this work. In particular, this chapter describes the data-monitoring system to which the author significantly contributed.

Then the statistical tools used directly by the author are presented in Chapter 5. This is where the likelihood analysis and the Feldman-Cousins (FC) procedure are defined. The results are also shown in this chapter. The CsI and CENNS-10 data were used to constrain the ϵ_{ee}^{dV} and ϵ_{ee}^{uV} NSI couplings, and the design of the COHERENT Ge detector was assumed for estimating its μ_{ν_μ} sensitivity.

Lastly, I conclude with a discussion of the results and possible ways of improving them.

Chapter 2

Neutrino Physics

In the SM, neutrinos are neutral fermions that only interact via the weak interaction. They are assumed to be massless fundamental particles that form left electroweak SU(2) doublets with the corresponding charged leptons. Therefore, just as charged leptons, they exist in three flavors: electron (e), muon (μ), and tau (τ). Taking into account that their antiparticles, antineutrinos, interact differently with matter and can be distinguished from the corresponding neutrinos, the SM includes six types of neutrinos in total.

Because of the existence of the phenomenon of neutrino oscillations, we know that neutrinos actually have masses. They propagate in three mass states, which are different from the aforementioned flavor states, and the masses of at least two of those states are non-zero.

Neutrinos are also well known to be hard to measure due to weak-interaction couplings being orders of magnitude smaller than couplings associated with other SM forces. A typical neutrino-nucleus cross section at the MeV scale is around 10^{-41} cm^2 (see Figure 2.1), while the characteristic nuclear-interaction cross section is on the order of 10^{-24} cm^2 (approximately the area of an atomic nucleus). Thus, neutrino detectors are usually of considerable size and contain many tons of sensitive materials in order to survey enough nuclei for the probability of at least one neutrino interacting in the detector volume to be non-negligible.

Weak interactions are mediated by the electroweak bosons, $W^\pm$ and Z^0, which therefore serve as mediators for neutrino interactions. Neutrino reactions that involve the $W^\pm$ boson are called charged-current (CC) interactions, and reactions with the Z^0

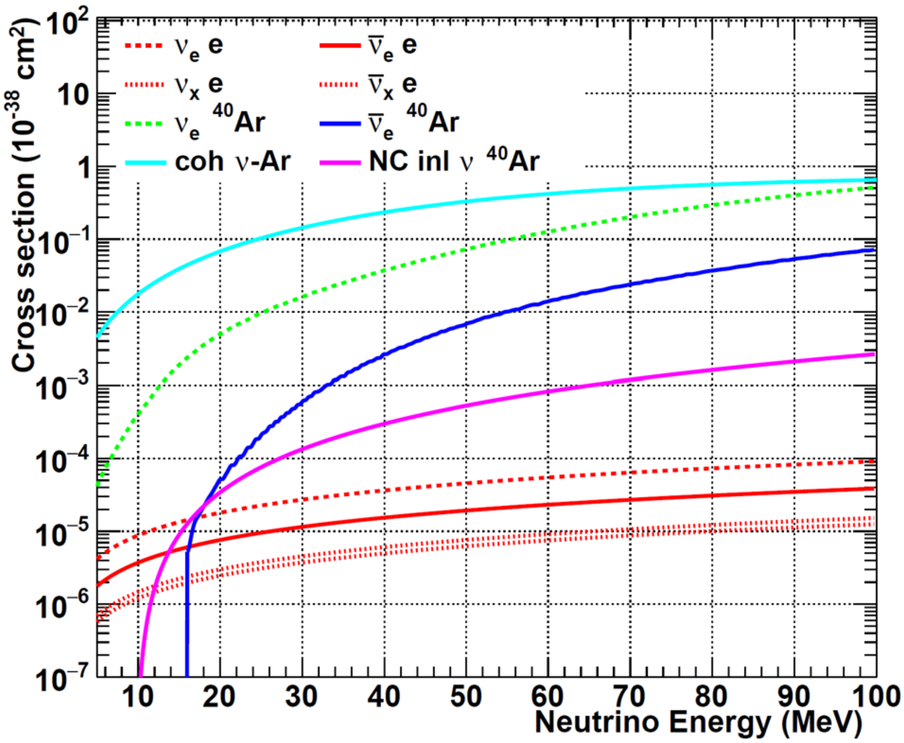

Figure 2.1: Neutrino cross sections in argon [A+c]. The red curves are elastic-scattering neutrino cross sections on electrons, the green and blue curves are CC interactions, the magenta curve is the NC interaction, and the teal curve is the CEνNS cross section on argon.

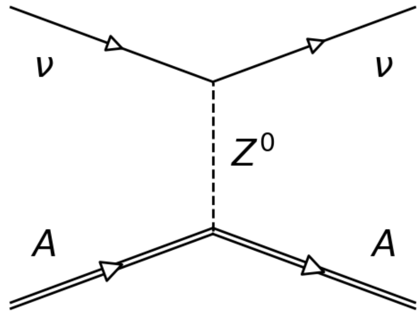

Figure 2.2: Feynman diagram representing CEνNS.

boson are neutral-current (NC) interactions. In a CC reaction, the incoming neutrino turns into the corresponding charged lepton, which can then be detected. A SM NC reaction does not change the neutrino type, so only the other participant's final state can be observed (for low energy neutrinos interacting with nuclei, the observable can be nuclear recoil, deexcitation gammas, etc.).

2.1 Coherent Elastic Neutrino-Nucleus Scattering

2.1.1 Standard-Model CEνNS

The SM allows for a neutrino to interact with a nucleus as a whole without changing its own or the nucleus' internal state. This interaction is CEνNS:

$$\nu + A \to \nu + A, \tag{2.1}$$

where ν is the neutrino and A is the nucleus it interacts with (see Figure 2.2).

If $\boldsymbol{p}_{\nu,A}$ and $\boldsymbol{p}'_{\nu,A}$ are the initial and the final momenta of the neutrino and the nucleus, respectively, and assuming that the target nucleus starts at rest ($p_A = 0$), then the momentum transfer is

$$\boldsymbol{Q} = \boldsymbol{p}_\nu - \boldsymbol{p}'_\nu = \boldsymbol{p}'_A \tag{2.2}$$

and its square is (using $E^2 - p^2 = m^2$)

$$Q^2 = \left(\boldsymbol{p}_A^{'}\right)^2 = (M+T)^2 - M^2 = 2MT + T^2 \approx 2MT, \tag{2.3}$$

where T is the nuclear recoil energy, M is the mass of the nucleus, and $T \ll 2M$.

The maximum momentum transfer (and maximum nuclear recoil) corresponds to the head-on collision, where the target nucleus recoils in the initial direction of the incoming neutrino. In this case, we can rewrite the law of conservation of four-momenta, $P_\nu + P_A = P_\nu^{'} + P_A^{'}$, as

$$P_\nu + P_A - P_A^{'} = P_\nu^{'} \tag{2.4}$$

and square it to get

$$0 = \left(P_\nu + P_A - P_A^{'}\right)^2 = -2T_{max}\left(M + E_\nu\right) + 2E_\nu\sqrt{T_{max}^2 + 2MT}. \tag{2.5}$$

Solving this equation for T_{max} gives us

$$T_{max} = \frac{2E_\nu^2}{2E_\nu + M}, \tag{2.6}$$

which can be plugged into the expression for Q:

$$Q_{max} = \sqrt{2MT_{max}} = 2E_\nu \frac{1}{\sqrt{1 + \frac{2E_\nu}{M}}} \approx 2E_\nu, \tag{2.7}$$

where the approximation assumes low-energy incoming neutrinos ($2E_\nu \ll M$).

For CEνNS to occur with relatively high probability, the neutrino has to be of sufficiently low energy. As the energy gets higher, the probability of interacting with individual nucleons rather than the whole nucleus increases (see section 2.1.2). Neutrinos scatter off a nucleus coherently when $\frac{h}{Q}$ is greater than the size of the nucleus, with h being the Planck constant and Q the momentum transfer. For a medium-size nucleus, this makes CEνNS more likely for $Q \lesssim 100$ MeV (using $c = 1$), and, since $0 < Q < 2E_\nu$, for neutrinos with $E_\nu \lesssim 50$ MeV. Considering argon with the nuclear radius $R = 1.2A^{\frac{1}{3}}$ fm $= 4.1$ fm (and using its diameter as the size of the nucleus), the coherency is expected for $Q \lesssim 150$ MeV (which scales with $A^{-\frac{1}{3}}$ for other nuclei).

CEνNS is an NC reaction and is mediated by the Z^0 boson. Since the Z^0 mass (91.1876 GeV [T$^+$18]) is much greater than the CEνNS energy scale (up to hundreds of MeV), the following four-fermion effective Lagrangian can be used for the interaction between the neutrino and a quark (approximated from J. Barranco et al. [BMR07]):

$$\mathcal{L}_{\nu q}^{NC} = -\frac{G_F}{\sqrt{2}} \left[\bar{\nu}\gamma^\mu \left(1-\gamma^5\right)\nu\right] \left(f^{qL}\left[\bar{q}\gamma_\mu\left(1-\gamma^5\right)q\right] + f^{qR}\left[\bar{q}\gamma_\mu\left(1+\gamma^5\right)q\right]\right), \quad (2.8)$$

where q is the up or down quark, G_F is the Fermi constant,

$$f^{uL} = \frac{1}{2} - \frac{2}{3}\sin^2\theta_W, f^{dL} = -\frac{1}{2} + \frac{1}{3}\sin^2\theta_W, f^{uR} = -\frac{2}{3}\sin^2\theta_W, f^{dR} = \frac{1}{3}\sin^2\theta_W,$$

θ_W is the Weinberg weak mixing angle.

2.1.2 CEνNS Cross Section

Using the Lagrangian in Equation 2.8, we can calculate the CEνNS differential cross section [BMR07]:

$$\frac{d\sigma}{dT} = \frac{G_F^2 M}{2\pi}\left\{(G_V+G_A)^2 + (G_V-G_A)^2\left(1-\frac{T}{E_\nu}\right)^2 - \left(G_V^2-G_A^2\right)\frac{MT}{E_\nu^2}\right\}, \quad (2.9)$$

where M is the mass of the nucleus, T is the nuclear recoil energy (taking values from 0 to $\frac{2E_\nu^2}{M+2E_\nu}$), E_ν is the neutrino energy,

$$G_V = \left[g_V^p Z + g_V^n N\right] F_{nucl}^V(Q^2),$$

$$G_A = \left[g_A^p \left(Z_+ - Z_-\right) + g_A^n \left(N_+ - N_-\right)\right] F_{nucl}^A(Q^2),$$

are the nuclear vector and axial-vector weak couplings, $g_V^p = \frac{1}{2} - 2\sin^2\theta_W$ and $g_V^n = -\frac{1}{2}$, are the vector weak couplings of the proton and the neutron, $g_A^p = -\frac{1}{2}$ and $g_A^n = \frac{1}{2}$, are the axial-vector weak couplings of the proton and the neutron, Z and N are the atomic number and the neutron number of the nucleus, Z_+ and Z_- are the numbers of spin-up and spin-down protons, N_+ and N_- are the numbers of spin-up and spin-down neutrons, and $F_{nucl}^V(Q^2)$ and $F_{nucl}^A(Q^2)$ are the vector and axial-vector nuclear form factors, respectively. The form factor is the Fourier transform of the corresponding density distribution.

For most nuclei, $(Z_+ - Z_-), (N_+ - N_-) \ll Z, N$ (the differences are 0 for symmetric isotopes), so the axial-vector component of the cross section can be neglected. In addition, $g_V^p = 0.0376 \ll g_V^n = 0.5$ (using the $\sin^2\theta_W$ value from M. Tanabashi et al. [T+18]). Disregarding these smaller contributions (along with the second-order $\frac{T}{E_\nu}$ term), Equation 2.9 simplifies to:

$$\frac{d\sigma}{dT} = \frac{G_F^2 M}{8\pi} N^2 F^2(Q^2)\left(2 - \frac{2T}{E_\nu} - \frac{MT}{E_\nu^2}\right), \tag{2.10}$$

where $F(Q^2) \equiv F_{nucl}^V(Q^2)$. The resulting N^2 scaling of the cross section is a characteristic feature of the CEνNS interaction.

The process is fully coherent when $Q^2 = 0$ and the nuclear form factor $F(Q^2) = 1$. For non-zero energy transfer, $F(Q^2) < 1$, and I use the Klein-Nystrand parameterization [KN99] here to quantify its value:

$$F(Q^2) = \frac{3\left(\sin(QR_n) - QR_n\cos(QR_n)\right)}{\left(QR_n\right)^3\left(1 + a_{kn}^2 Q^2\right)}, \tag{2.11}$$

where $R_n = 1.2A^{\frac{1}{3}}$ fm is the nuclear radius and $a_{kn} = 0.7$ fm is the Yukawa-potential range. Form factors for a range of isotopes are plotted in Figure 2.3. For most nuclei,

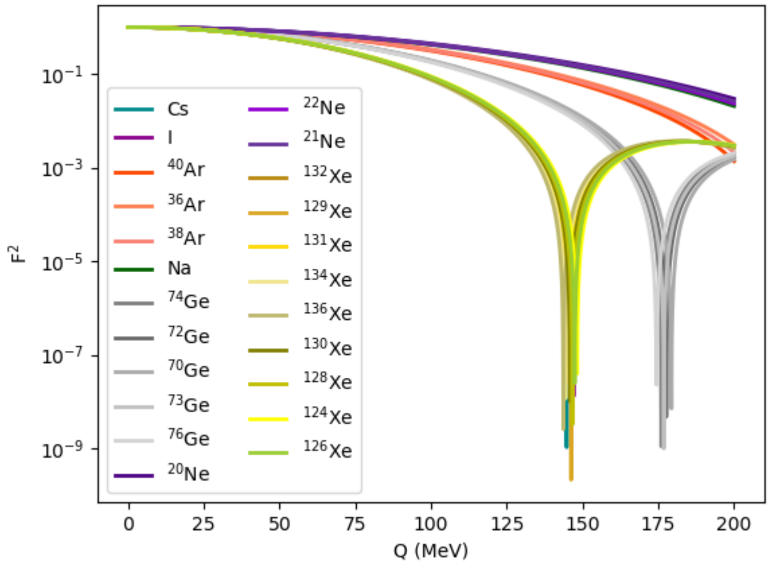

Figure 2.3: Klein-Nystrand form factors plotted against the momentum transfer (using $c = 1$) for multiple nuclei. Q does not exceed approximately 100 MeV for the neutrino sources considered in this work.

the form factor drops precipitously above around 100 MeV/c (the heavier the nucleus, the sharper the drop), drastically reducing the CEνNS cross section at high Q.

CEνNS experiments use neutrinos produced by either nuclear reactors or stopped-pion sources (πDAR), for which four-momentum difference values vary from 0 to $Q_{max} = \sqrt{2MT_{max}} \approx 2E_\nu^{max} \approx 10$ (100) MeV for nuclear reactors (πDAR). Therefore, the nuclear form factor is close to 1 for most neutrino interactions in the reactor experiments, while the πDAR experiments are expected to observe noticeable deviations from unity for their higher-energy neutrino interactions.

Equation 2.10 is plotted in Figure 2.4 for different nuclei and same neutrino energy. The figure shows the main challenge of CEνNS detection: as the total cross section quadratically increases with the neutron number, the end-point recoil energy drops, requiring detectors with exceedingly low energy thresholds to observe it.

The differential CEνNS cross section can be integrated over recoil energy to get

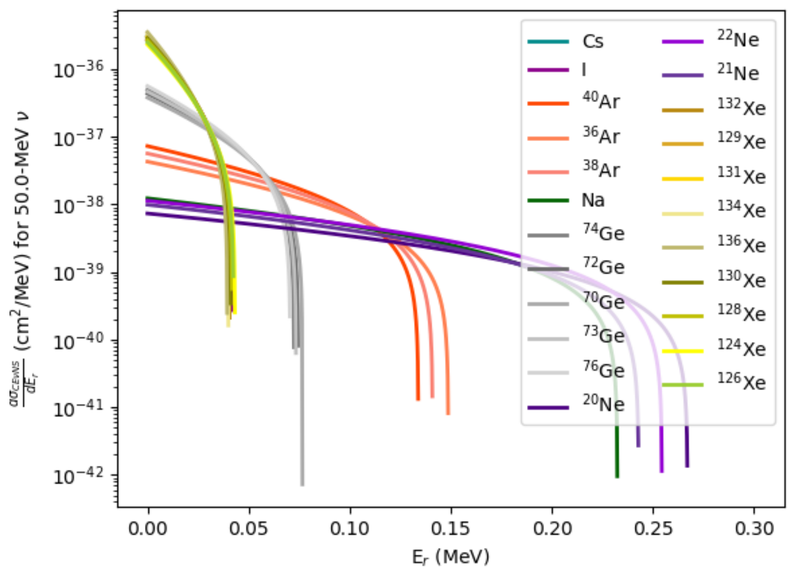

Figure 2.4: Differential CEνNS cross sections for multiple isotopes and neutrinos with $E_\nu = 50$ MeV.

a total cross section as a function of neutrino energy. Integrating Equation 2.10 and plotting the result produces Figure 2.5 showing the total CEνNS cross section for a number of isotopes. The cross-section values are larger than 10^{-40} cm^2 at 50 MeV even for the lighter nuclei.

2.1.3 Experimental Efforts

After CEνNS was predicted in 1974 by D. Z. Freedman [Fre74], multiple detection approaches have been put forward. Despite the variety of the proposed detectors, they all have to be extremely sensitive to nuclear recoils in the low-energy range. However, unlike conventional neutrino detectors that usually operate on the ton-to-Mton scale, CEνNS proposals often include kg-scale targets which is possible because of the relatively large cross section.

Table 2.1 compares the neutrino sources used by experiments discussed here: πDAR, nuclear reactors, Sun, supernovae. Figures 2.6, 2.7, 2.8, and 2.9 show their

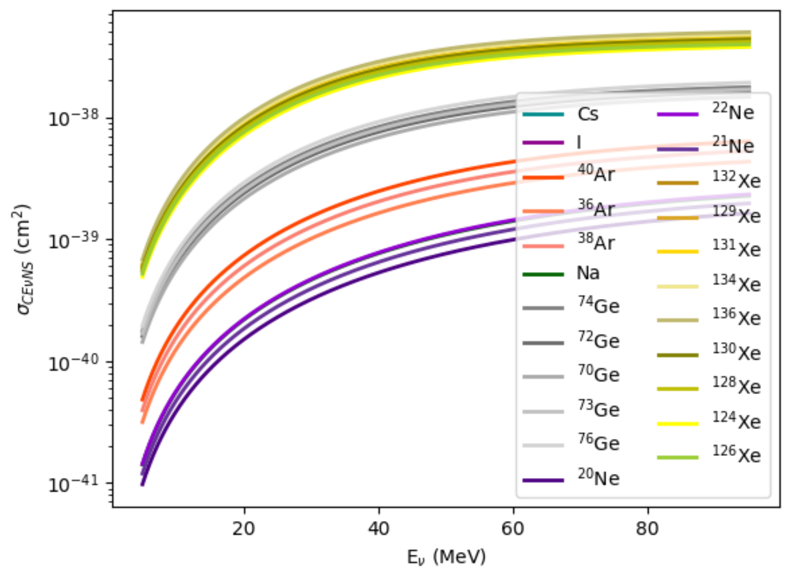

Figure 2.5: Total CEνNS cross sections for multiple isotopes.

Source	ν type	Timing
πDAR	ν_μ, $\bar{\nu}_\mu$, ν_e	pulsed
Reactor	$\bar{\nu}_e$	continuous
Sun	ν_e	continuous
Supernova	all ν	burst (O(10 s))

Table 2.1: Sources that produce neutrinos used in CEνNS studies.

respective energy and CEνNS-recoil spectra.

Detector technologies employed by CEνNS experiments include inorganic scintillators, liquid noble gases (both scintillators and single- and dual-phase time-projection chambers), bolometers, and semiconductors and are summarized in Table 2.2.

Dark-matter experiments have similar requirements for weakly-interacting-massive-particle (WIMP [Sch19]) searches, since WIMP interactions are also expected to produce low-energy nuclear recoils, making WIMP detectors also particularly well suited for CEνNS detection. However, those detectors are usually located deep underground and far from artificial sources of neutrinos to reduce backgrounds, which makes them impossible to use in a manner similar to the previously mentioned exper-

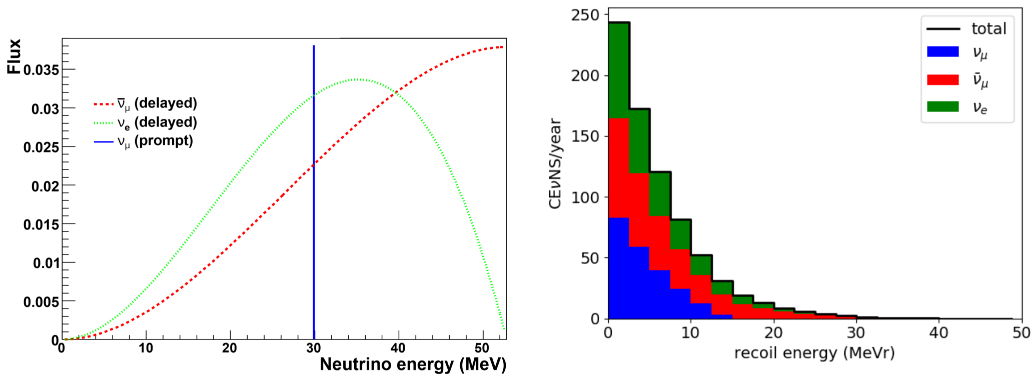

Figure 2.6: πDAR neutrino spectra [Sch06] (left) and CEνNS recoils (right) in a CsI detector in a COHERENT-like set-up (see Chapter 3).

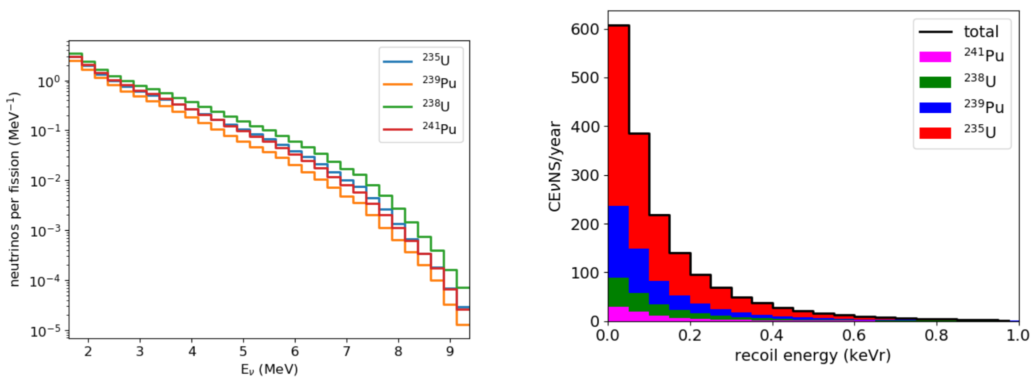

Figure 2.7: Nuclear-reactor electron antineutrino spectra (left, data from V. V. Sinev [Sin13]) and CEνNS recoils (right) in a 10-kg Ge detector located 10 m from a 1000-MW reactor (with reactor composition from V. V. Sinev [Sin13]).

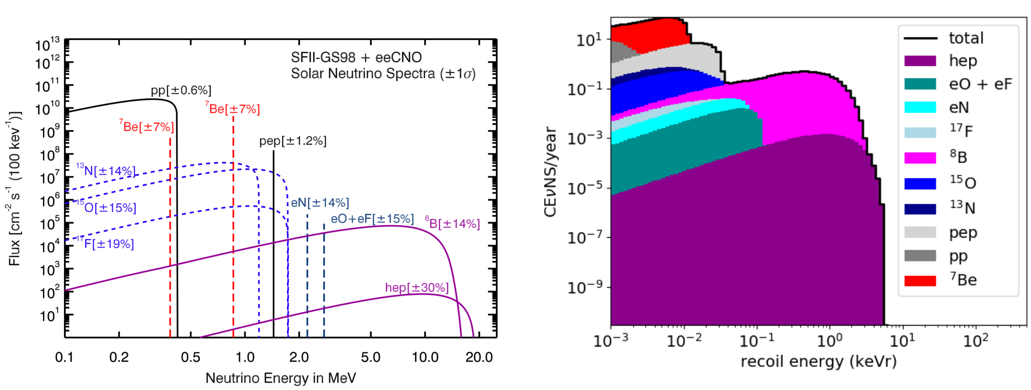

Figure 2.8: Solar neutrino spectra [Ser16] (left) and CEνNS recoils (right) in a 1-t Xe detector.

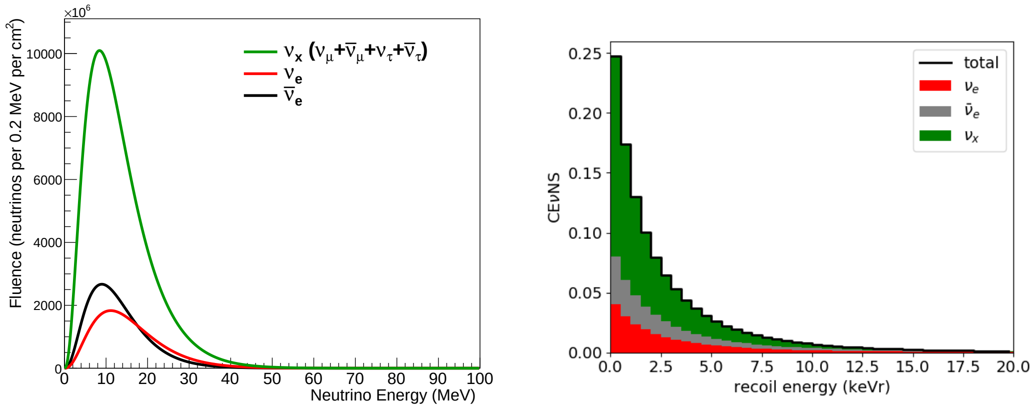

Figure 2.9: Supernova neutrino spectra [snb] (left) and CEνNS recoils (right) in a 1-t Xe detector.

Source	Experiment	Detector	Location
πDAR	COHERENT [A$^+$a]	CsI, LAr, HPGe, NaI, etc.	USA
πDAR	CCM [AA$^+$a]	LAr	USA
Reactor	CONNIE [AA$^+$19]	Si CCDs	Brazil
Reactor	CONUS [B$^+$20]	HPGe	Germany
Reactor	MINER [A$^+$17a]	Cryogenic Ge/Si	USA
Reactor	NEWS-G [A$^+$18c]	Spherical Proportional Counters	Canada/France
Reactor	NuCLEUS [S$^+$17]	Cryogenic $CaWO_4$	Germany
Reactor	RED-100 [A$^+$20c]	Dual-phase LXe	Russia
Reactor	RICOCHET [B$^+$17]	Ge, Zn bolometers	France
Reactor	TEXONO [S$^+$16]	p-PCGe	Taiwan
Sun, SN	Darkside-LM [A$^+$18a]	LAr	Italy
Sun, SN	LZ [A$^+$20a]	Dual-phase LXe	USA
Sun, SN	SuperCDMS [LA19]	Cryogenic Ge/Si	Canada
Sun, SN	Xenon NT [A$^+$17d]	Dual-phase LXe	Italy

Table 2.2: CEνNS-sensitive experiments.

iments. Nevertheless, WIMP detectors can study CEνNS using astrophysical neutrinos with current-generation ton-scale experiments having sensitivity for supernova-burst neutrinos [HCM03] and future multi-ton-scale experiments being able to observe solar neutrinos [HKM12] (which is being investigated as an important background for WIMP searches [BSFF14]).

2.1.4 COHERENT Measurements

The first observation of CEνNS was performed by the COHERENT collaboration in 2017 using a stopped-pion source [A$^+$17c] (see Chapter 3 for a detailed description of the experiment). The collaboration deployed a 14.6-kg CsI detector and neutrinos from a stopped-pion source and detected 134$\pm$22 CEνNS events at a 6.7-σ confidence level. Figure 2.10 shows the resulting energy and time distributions of the measured neutrinos. The most significant sources contributing to the total uncertainty are the CsI quenching-factor uncertainty (25%), statistics, and the neutrino-flux uncertainty (10%).

The COHERENT collaboration performed another measurement in 2020 with a 24-kg liquid-argon detector and observed 159$\pm$43 CEνNS events [A$^+$20b]. The statistical significance of the result is 3.5 σ. In this case, the total systematic uncertainty is dominated by the flux uncertainty (10%) and pulse-shape-discrimination calibration uncertainty (7.8%).

2.1.5 CEνNS Beyond Standard Model

CEνNS is a well-understood SM process, which makes it an excellent laboratory for studying physics beyond the SM (BSM). The number of ongoing and proposed CEνNS experiments (see section 2.1.3) should also result in multiple precision measurements of CEνNS on different nuclei.

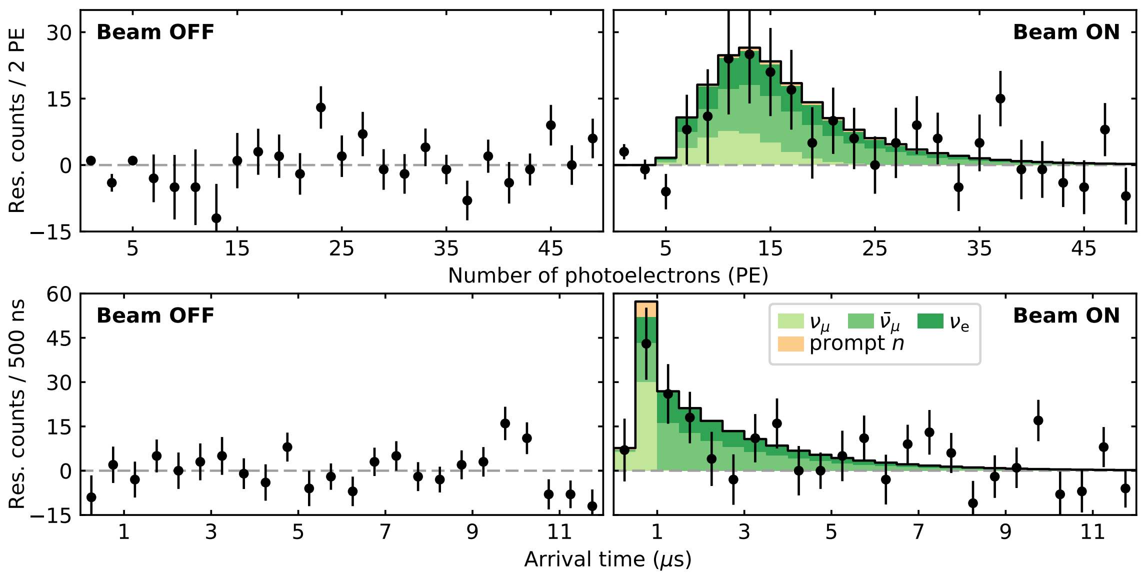

Figure 2.10: Energy and time distributions (after steady-state background subtraction) of the CEνNS measurement performed by the COHERENT collaboration [A$^+$17c]. The points are the data and the histograms are the distributions predicted by the SM. The right and the left columns show the distributions for the time periods when the source was and was not producing neutrinos, respectively.

2.1.6 Applications of CEνNS

The neutrino is a unique particle that, unlike other known particles, does not usually interact on its way from where it was produced to the detector. This property leads to a great number of possible applications. Unfortunately, this attribute also greatly limits the possibilities, because it makes neutrinos difficult to observe. Because the CEνNS cross section is orders of magnitude higher than other neutrino cross sections at the same energy (which is energy dependent and only true below about 50 MeV), there are enhanced applications.

Being an NC interaction, CEνNS is flavor independent and can also greatly complement other neutrino measurements, most of which detect charged-current reactions.

2.2 Non-Standard Neutrino Interactions

Non-standard neutrino interactions (NSI) are a category of BSM physics that includes modifications to the SM neutrino interactions. NSI can contribute to either CC or NC interactions, but in this work only NC-modifying NSI are considered because they can mimic SM CEνNS events.

2.2.1 Heavy-Mediator NSI

NSI discussed here are generated by a neutral electroweak boson with its mass much greater than the energy scale of the reaction. The resulting process is a new neutral-current interaction that in general allows the participating neutrino to change its flavor, as in:

$$\nu_\alpha + f \to \nu_\beta + f, \tag{2.12}$$

where ν_α is the incoming neutrino, ν_β is the outgoing neutrino, and f is the interacting fermion.

The Lagrangian term that describes such four-point NSI interaction is the following [CDGG$^+$17]:

$$\mathcal{L}_{\alpha\beta}^{fP} = -2\sqrt{2}G_F\epsilon_{\alpha\beta}^{fP}\left[\bar{\nu}_\alpha\gamma^\mu\left(1-\gamma^5\right)\nu_\beta\right]\left[\bar{f}\gamma_\mu Pf\right], \tag{2.13}$$

where P is the projection operator ($P_L = (1-\gamma^5)$ or $P_R = (1+\gamma^5)$), G_F is the Fermi constant, and $\epsilon_{\alpha\beta}^{fP}$ is the corresponding NSI coupling. The α and β flavors can be e, μ, or τ, and f is mostly e, u, or d for normal matter. A diagram for this process is shown in Figure 2.11.

2.2.2 NSI in Neutrino Oscillations

NSI affect both neutrino interactions and propagation in matter, the latter of which is able to modify neutrino oscillations. The Hamiltonian describing neutrino propa-

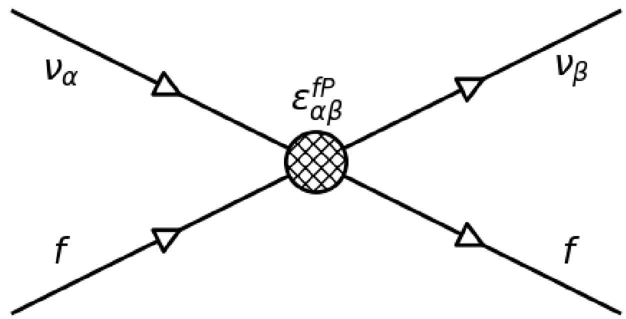

Figure 2.11: Diagram of NSI.

gation is the following [CDGG+17]:

$$H^\nu = H_{vac} + H_{mat} = \frac{1}{2E} U_{vac} \begin{pmatrix} 0 & & \\ & \Delta m_{21}^2 & \\ & & \Delta m_{31}^2 \end{pmatrix} U_{vac}^\dagger + \sqrt{2} G_F N_e(x) \begin{pmatrix} 1+\epsilon_{ee} & \epsilon_{e\mu} & \epsilon_{e\tau} \\ \epsilon_{e\mu}^* & \epsilon_{\mu\mu} & \epsilon_{\mu\tau} \\ \epsilon_{e\tau}^* & \epsilon_{\mu\tau}^* & \epsilon_{\tau\tau} \end{pmatrix}, \tag{2.14}$$

where H_{vac} and H_{mat} are the Hamiltonians for neutrino propagation in vacuum and matter respectively, E is the neutrino energy, $\Delta m_{ij}^2 = m_i^2 - m_j^2$ are the differences between squares of the respective neutrino-mass-state masses,

$$U_{vac} = \begin{pmatrix} c_{12}c_{13} & s_{12}c_{13} & s_{13}e^{-i\delta} \\ -s_{12}c_{23} - c_{12}s_{13}s_{23}e^{i\delta} & c_{12}c_{23} - s_{12}s_{13}s_{23}e^{i\delta} & c_{13}s_{23} \\ s_{12}s_{23} - c_{12}s_{13}c_{23}e^{i\delta} & -c_{12}s_{23} - s_{12}s_{13}c_{23}e^{i\delta} & c_{13}c_{23} \end{pmatrix} \tag{2.15}$$

is the vacuum neutrino mixing matrix [T+18] with $c_{ij} = \cos\theta_{ij}$, $s_{ij} = \sin\theta_{ij}$, and θ_{ij} the neutrino mixing angles, δ is the CP-violation phase, $N_e(x)$ is the cumulative electron density along the neutrino path at location x,

$$\epsilon_{\alpha\beta} = \sum_{f=u,d,e} Y_f(x)\epsilon_{\alpha\beta}^{fV} \tag{2.16}$$

are the effective NSI couplings with $Y_f(x)$ being the relative density of f (relative to electron density, so $Y_e(x) = 1$). The Hamiltonian for antineutrino propagation is $H^{\bar{\nu}} = (H_{vac} - H_{mat})^*$.

Adding a constant term to H^ν does not affect the propagation of neutrinos, making neutrino oscillations sensitive to differences of diagonal couplings, $\epsilon_{\alpha\alpha}-\epsilon_{\beta\beta}$, rather than their individual values.

The CPT symmetry results in identical neutrino evolution for both H^ν and $-(H^\nu)^*$. The following substitutions transform H^ν into $-(H^\nu)^*$:

$$\begin{aligned}
\Delta m_{31}^2 &\to -\Delta m_{31}^2 + \Delta m_{21}^2 = -\Delta m_{32}^2,\\
\sin\theta_{12} &\to \cos\theta_{12},\\
\delta &\to \pi - \delta,\\
(\epsilon_{ee} - \epsilon_{\mu\mu}) &\to -(\epsilon_{ee} - \epsilon_{\mu\mu}) - 2,\\
(\epsilon_{\tau\tau} - \epsilon_{\mu\mu}) &\to -(\epsilon_{\tau\tau} - \epsilon_{\mu\mu}),\\
\epsilon_{\alpha\beta} &\to -\epsilon_{\alpha\beta}^* \; (\alpha \neq \beta).
\end{aligned} \tag{2.17}$$

These changes flip the neutrino mass ordering, θ_{12} octant and the CP-violation phase, creating ambiguity in their determination if NSI couplings are not measured independently. This effect is called generalized mass ordering degeneracy [CS16] and cannot be resolved using only neutrino-oscillation measurements.

2.2.3 Neutrino Oscillation and Fixed-Target Results

NSI couplings have been constrained in neutrino oscillation and fixed-target experiments. A good summary of the NSI knowledge before the publication of the first COHERENT results is presented in P. Coloma et al. [CDGG$^+$17]. The paper did a global fit of the available neutrino-experiment data and produced Figure 2.12. The neutrino-oscillation fit included reactor (KamLAND, CHOOZ, Palo Verde, Double CHOOZ, Daya Bay, RENO, Bugey, ROVNO, Krasnoyarsk, ILL, Gösgen, and SRP), solar (Chlorine, Gallex/GNO, SAGE, Super-Kamiokande, Borexino, SNO), atmospheric (Super-Kamiokande), and long-baseline (MINOS and T2K) neutrino

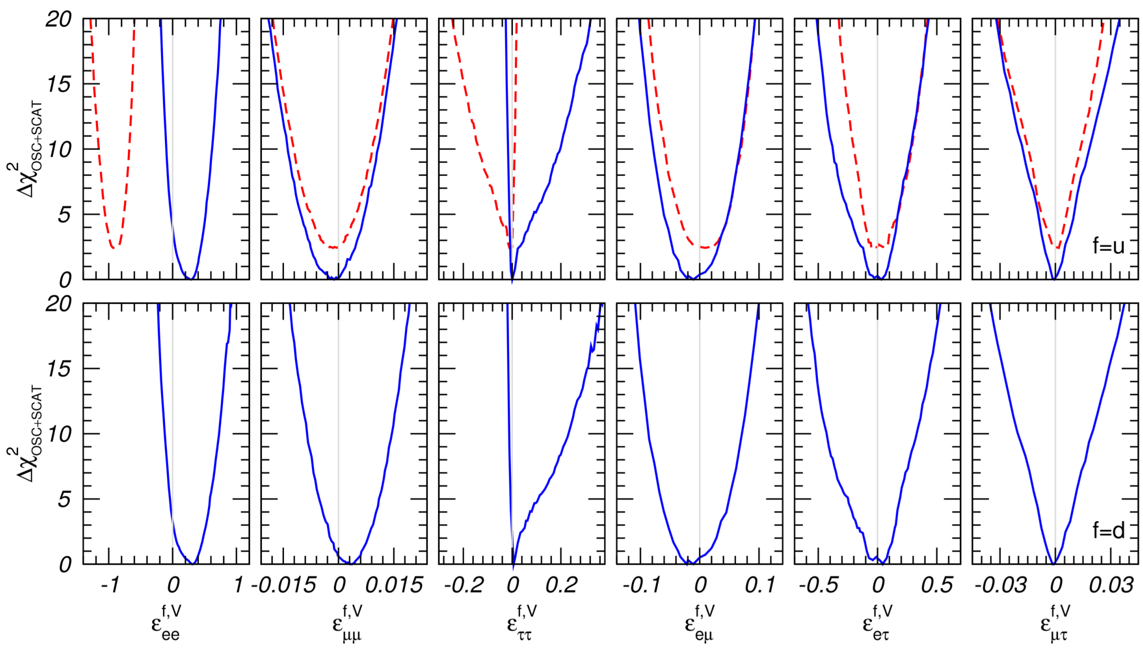

Figure 2.12: Global-fit χ^2 distributions for twelve NSI couplings from P. Coloma et al. [CDGG$^+$17]. The solid blue and dashed red lines correspond to the large-mixing-angle (LMA) and LMA-Dark solutions, respectively. The former is preferred by the SM interpretation of neutrino oscillation experiments, and the latter appears for certain values of NSI couplings [MTV06].

measurements. In addition to those results, the global fit included two neutrino scattering experiments: NuTeV and CHARM.

Based on that figure, the weakest constraints exist for the ϵ_{ee}^{dV} and ϵ_{ee}^{uV} couplings, since their χ^2 profiles are wider than the profiles corresponding to other NSI couplings. The only experiment that was used to unambiguously determine the ϵ_{ee}^{dV} and ϵ_{ee}^{uV} couplings is CHARM, resulting in a limit in Figure 2.13.

CHARM [D$^+$86] consisted of a calorimeter and muon spectrometer observing neutrinos produced by the 400-GeV CERN-SPS proton beam interacting with thick copper targets. The experiment measured charged- and neutral-current cross sections for electron neutrinos and antineutrinos and produced the following ratio:

$$R_e = \frac{\sigma(\nu_e N \to \nu_e X) + \sigma(\bar{\nu}_e N \to \bar{\nu}_e X)}{\sigma(\nu_e N \to e X) + \sigma(\bar{\nu}_e N \to \bar{e} X)} = 0.406 \pm 0.140, \tag{2.18}$$

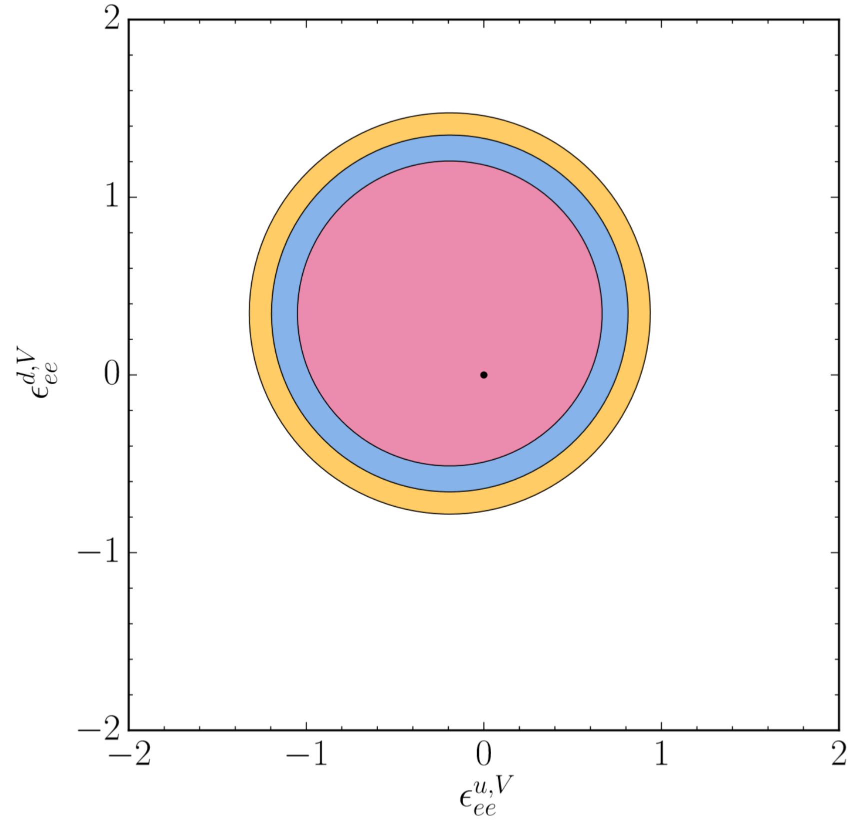

Figure 2.13: 1-σ, 2-σ, and 3-σ regions allowed by the CHARM data for the ϵ_{ee}^{dV} and ϵ_{ee}^{uV} NSI couplings from P. Coloma et al. [CDGG+17].

which can be rewritten as

$$R_e = (g_u^V + \epsilon_{ee}^{uV})^2 + (g_u^A)^2 + (g_d^V + \epsilon_{ee}^{dV})^2 + (g_d^A)^2, \tag{2.19}$$

where g_q^P are the SM electroweak couplings. Combining Equations 2.18 and 2.19 results in a constraint on the ϵ_{ee}^{dV} and ϵ_{ee}^{uV} couplings.

2.2.4 Constraining NSI with CEνNS

CEνNS experiments measure neutrino scatters off nuclei. If the source neutrinos are of electron flavor, they provide an opportunity for measuring the ϵ_{ee}^{dV} and ϵ_{ee}^{uV} NSI couplings.

The corresponding NSI modify the nuclear vector electroweak couplings in the CEνNS differential cross-section expression [BMR07],

$$\frac{d\sigma}{dT} = \frac{G_F^2 M}{2\pi} \left\{ (G_V + G_A)^2 + (G_V - G_A)^2 \left(1 - \frac{T}{E_\nu}\right)^2 - \left(G_V^2 - G_A^2\right) \frac{MT}{E_\nu^2} \right\}, \quad (2.20)$$

in the following way:

$$G_V = \left[\left(g_V^p + 2\epsilon_{ee}^{uV} + \epsilon_{ee}^{dV} \right) Z + \left(g_V^n + \epsilon_{ee}^{uV} + 2\epsilon_{ee}^{dV} \right) N \right] F_{nucl}^V(Q^2).$$

One method of visualizing the effect of the NSI on CEνNS is to plot the cross-section modification factor, $\frac{d\sigma_{CE\nu NS}}{dT}\left(\epsilon_{ee}^{dV}, \epsilon_{ee}^{uV}\right) / \frac{d\sigma_{CE\nu NS}^{SM}}{dT}$, as a function of the ϵ_{ee}^{dV} and ϵ_{ee}^{uV} couplings. This is done for the COHERENT CsI detector in Figure 2.14. As expected from Equation 2.20 and its quadratic dependence on the NSI couplings, the pairs of the NSI couplings resulting in the SM cross-section value form two lines. The NSI suppress the cross section between the lines and enhance it otherwise. Therefore, a measurement of the CEνNS cross section can put a limit on the allowed NSI couplings.

2.2.5 COHERENT NSI Result

The COHERENT collaboration used its CsI CEνNS result to constrain the ϵ_{ee}^{dV} and ϵ_{ee}^{uV} NSI couplings [A+17c], with the allowed values shown as the blue band in Figure 2.15.

The COHERENT measurement has been analyzed by other groups, some of which performed the following NSI studies:

- Ref. [Giu] used the COHERENT data (including the spectral and temporal information) to constrain other NSI couplings, producing Figure 2.16;
- Ref. [CGGMS17] added the COHERENT data to the global oscillation fit and plotted the result as solid lines in Figure 2.17.

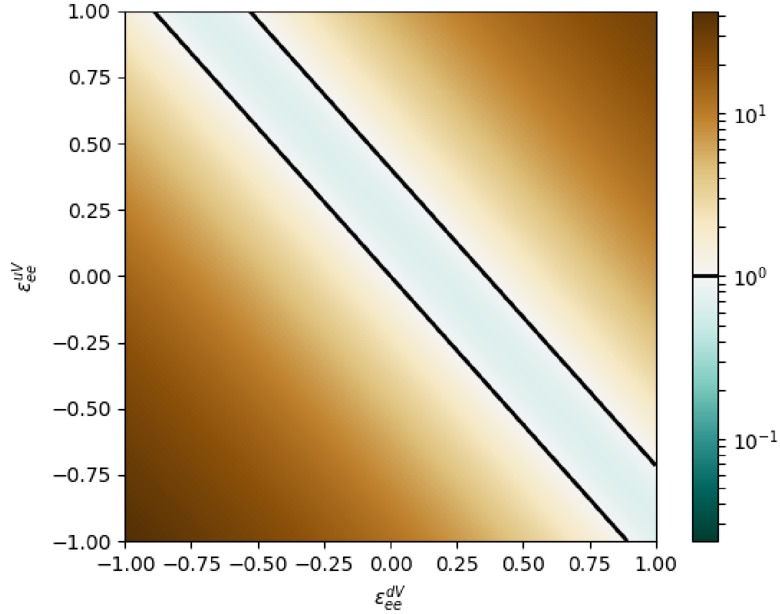

Figure 2.14: Cross-section modification dependence on the NSI couplings for the COHERENT CsI detector.

2.2.6 Light-Mediator NSI

It is also possible to remove the heavy-mediator assumption and instead consider NSI models produced by the following interaction Lagrangian [DDL$^+$17]:

$$\mathcal{L}_{\nu Z'}^{fP} = 2Z'_{\mu}\left(g_{\nu Z'}\bar{\nu}\gamma^{\mu}\left(1-\gamma^{5}\right)\nu + g_{fZ'}\bar{f}\gamma^{\mu}Pf\right), \tag{2.21}$$

where Z' is the new mediator, $g_{\nu Z'}$ and $g_{fZ'}$ are the interaction couplings of neutrinos and other fermions, respectively. This Lagrangian results in the following neutral-current reaction between a neutrino ν and a fermion f (shown in Figure 2.18):

$$\nu + f \rightarrow \nu + f. \tag{2.22}$$

This interaction can also contribute to CEνNS, modifying the nuclear electroweak couplings in Equation 2.20 and, unlike the heavy-mediator case, making them recoil-

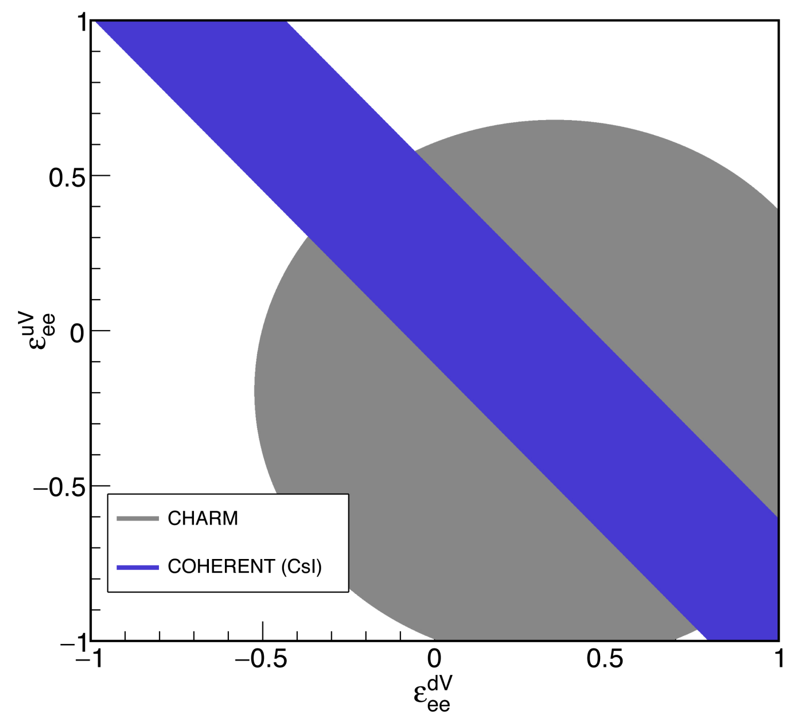

Figure 2.15: Regions of the ε_{ee}^{dV}–ε_{ee}^{uV} parameter space allowed by the COHERENT and CHARM experiments [A+17c]. NSI couplings not shown are set to 0.

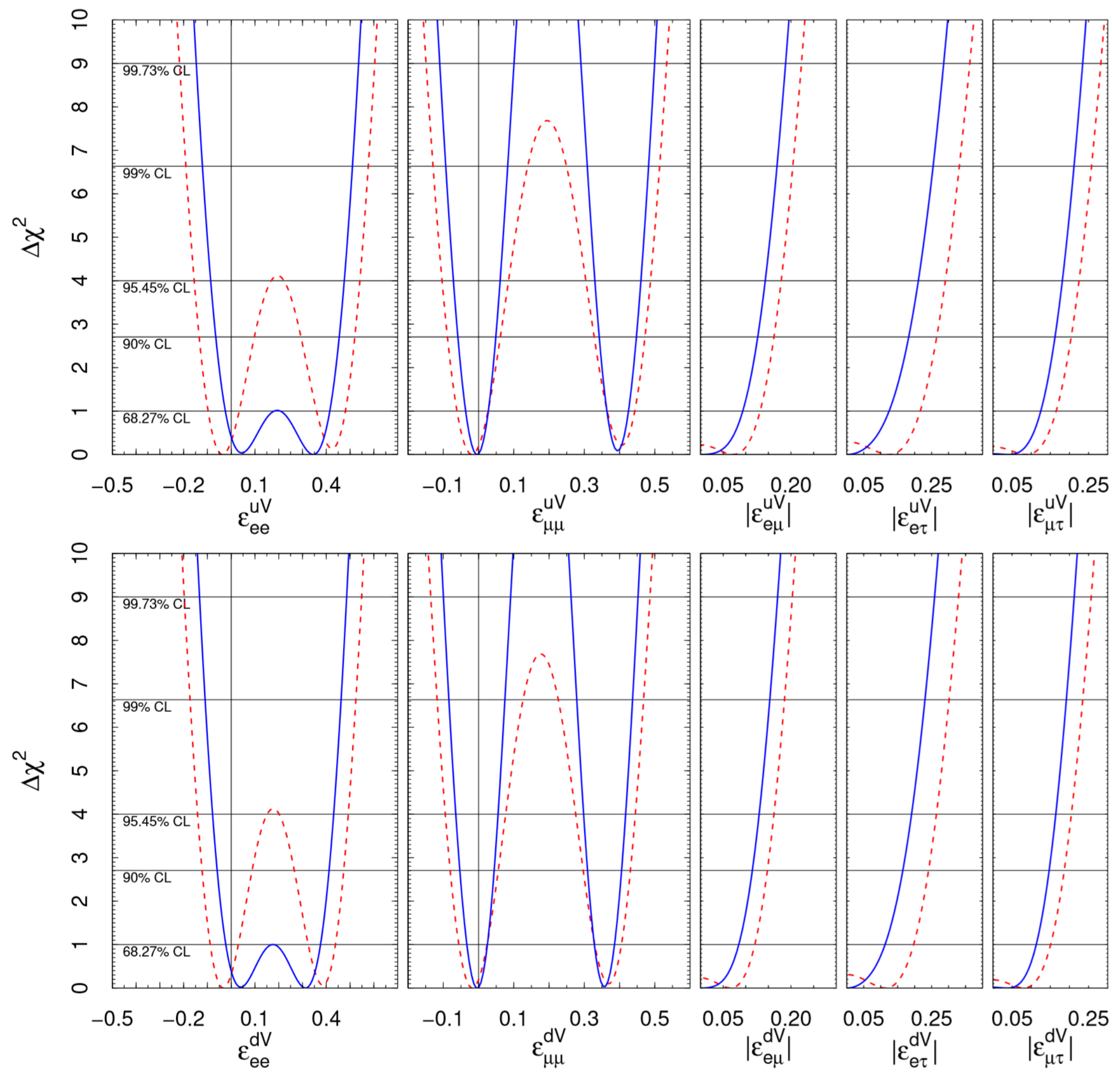

Figure 2.16: COHERENT fit χ^2 distributions for NSI couplings with (blue solid lines) and without timing information (red dashed lines) from C. Giunti [Giu].

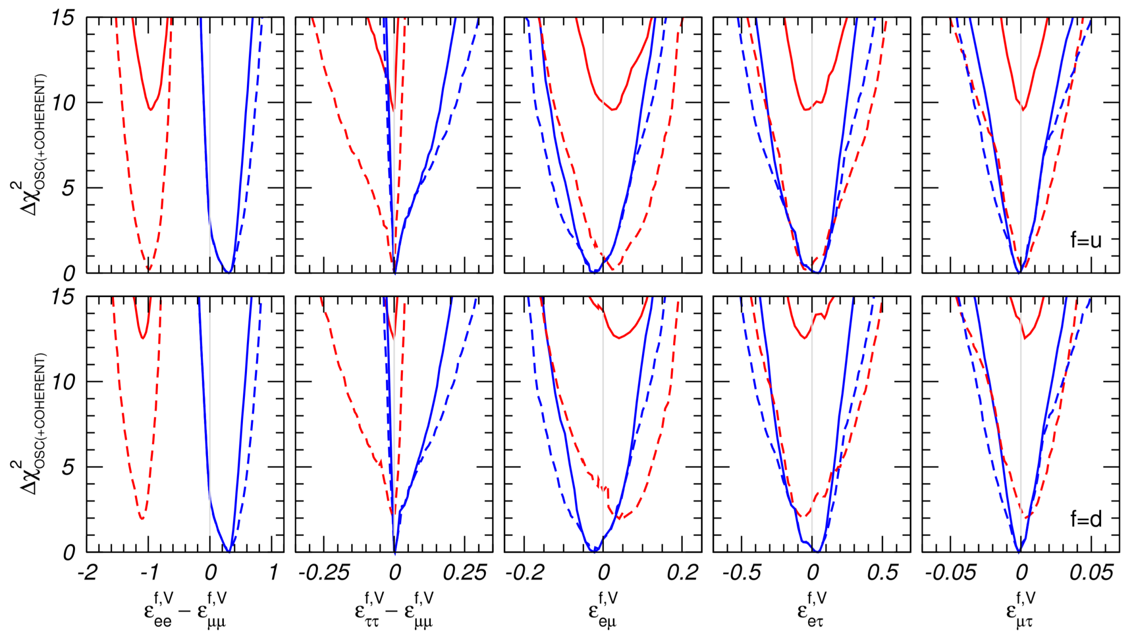

Figure 2.17: Neutrino-oscillation-fit χ^2 distributions for NSI couplings with (solid lines) and without COHERENT (dashed lines) from P. Coloma et al. [CGGMS17]. The blue and red lines correspond to the LMA and LMA-D solutions, respectively.

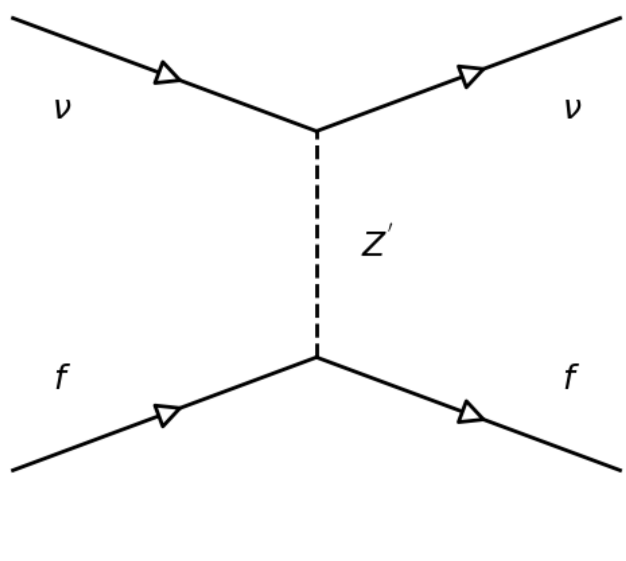

Figure 2.18: Diagram for light-mediator NSI.

energy-dependent as well:

$$G_V = \left[\left(g_V^p + \frac{g_{\nu Z'} g_{pZ'}}{\sqrt{2} G_F \left(2TM + M_{Z'}^2 \right)} \right) Z + \right.$$
$$\left. \left(g_V^n + \frac{g_{\nu Z'} g_{nZ'}}{\sqrt{2} G_F \left(2TM + M_{Z'}^2 \right)} \right) N \right] F_{nucl}^V(Q^2),$$

where $M_{Z'}$ is the mass of the mediator and $g_{pZ'}$ and $g_{nZ'}$ are the NSI couplings of the proton and the neutron, respectively.

The COHERENT collaboration plans to use COHERENT's data to constrain light-mediator NSI in a future analysis. Some of the analyses in the literature already performed include:

- Ref. [LM18] used the COHERENT data to study the coupling and mass of a Z' boson that interacts with neutrinos, first-generation quarks, and the muon and has a universal vector coupling;
- Ref. [ADD$^+$18] constrains models with a Z' boson using the COHERENT data and estimates the sensitivity of future CEνNS experiments;
- Ref. [DLSS19] performed a study with the COHERENT data and a Z' boson that couples to the up and down quarks and neutrinos with $g_u = g_d = g_\nu$.

2.3 Neutrino Magnetic Moment

Another example of BSM is enhancement of the neutrino magnetic moment. Neutrino physics currently predicts negligible neutrino magnetic moments, so an observation of a non-zero value would result in a significant disagreement between the SM prediction and the experimental result.

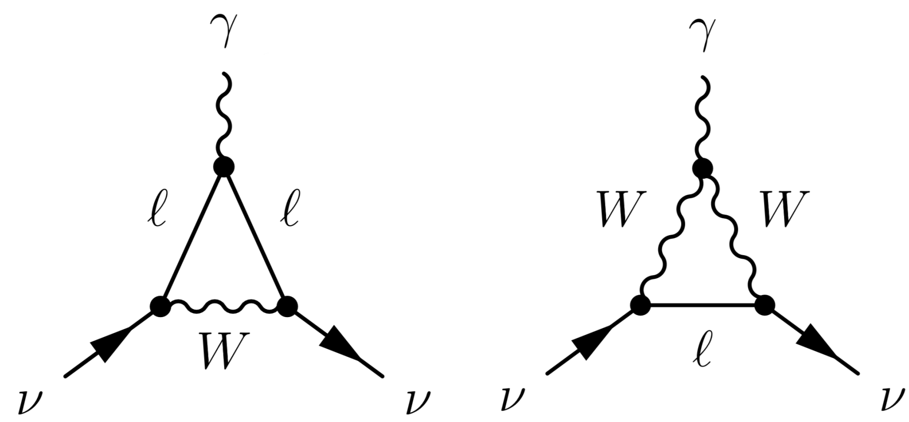

Figure 2.19: Loop SM diagrams contributing to the neutrino magnetic moment [GS15].

2.3.1 Neutrino Magnetic Moment in SM

In the SM, the dipole magnetic moment of the neutrino is calculated from the diagrams in Figure 2.19. The neutrino magnetic moment is strictly 0 in the absence of right-handed neutrinos, but minimal modifications to the SM that add right-handed neutrinos result in the following approximate value [GS15]:

$$\mu_\nu \approx \frac{3eG_{\mathrm{F}}m_\nu}{8\sqrt{2}\pi^2} \approx 3.2 \cdot 10^{-19} \left(\frac{m_\nu}{\mathrm{eV}}\right) \mu_B, \tag{2.23}$$

where e is the electric charge of the electron, G_{F} is the Fermi constant, m_ν is the neutrino mass, and μ_B is the Bohr magneton.

Because of the scale of the neutrino mass ($m_\nu < 1$ eV), the neutrino magnetic moment in this minimally extended SM is impossible to observe with the currently available technologies.

2.3.2 BSM Neutrino Magnetic Moment

BSM theories can produce neutrino-magnetic-moment values many orders of magnitude larger than the SM prediction. The following are several such models and their predicted neutrino magnetic moments:

- left-right symmetric models of electroweak interactions suggest magnetic-moment values as large as $\mu_\nu \approx 10^{-10}\mu_B$ [Raj90];
- Minimal Supersymmetric Standard Models predict values $\mu_\nu < 10^{-12}\mu_B$ [AIIN14];
- arguments from "naturalness" result in upper bounds of $\mu_\nu < 10^{-14}\mu_B$ [BCRM$^+$05].

2.3.3 Current Experimental Constraints

A non-zero neutrino magnetic moment manifests itself as a distortion in the measured recoil spectrum. Most experiments search for an excess in electron recoils to constrain neutrino magnetic moments using electron antineutrinos from reactors, neutrinos of different flavors produced by accelerators, and electron neutrinos from the Sun.

Table 2.3 summarizes the direct experimental knowledge of neutrino magnetic moments. The best 90%-CL limits for each flavor are the following:

- electron neutrino – $\mu_{\nu_e} < 2.9 \cdot 10^{-11}\mu_B$;
- muon neutrino – $\mu_{\nu_\mu} < 6.8 \cdot 10^{-10}\mu_B$;
- tau neutrino – $\mu_{\nu_\tau} < 3.9 \cdot 10^{-7}\mu_B$.

Solar-neutrino experiments constrain an effective neutrino magnetic moment that can be written in terms of magnetic moments of neutrinos in the flavor basis as the following [A$^+$17b]:

$$\mu_S^2 = P^{3\nu}\mu_{\nu_e}^2 + \left(1 - P^{3\nu}\right)\left(\cos^2\theta_{23}\cdot\mu_{\nu_\mu}^2 + \sin^2\theta_{23}\cdot\mu_{\nu_\tau}^2\right), \tag{2.24}$$

where $P^{3\nu}$ is the ν_e survival probability, θ_{23} is a neutrino mixing angle. Therefore, the 90%-CL limit $\mu_S < 2.8\cdot 10^{-11}\mu_B$ results in the following constraints on the magnetic

Method	Experiment	Limit (μ_B)	CL
Reactor $\bar{\nu}_e$-e^-	Krasnoyarsk [VVG+92]	$\mu_{\nu_e} < 2.4 \cdot 10^{-10}$	90%
	Rovno [DCP+93]	$\mu_{\nu_e} < 1.9 \cdot 10^{-10}$	95%
	MUNU [D+05]	$\mu_{\nu_e} < 9 \cdot 10^{-11}$	90%
	TEXONO [W+07]	$\mu_{\nu_e} < 7.4 \cdot 10^{-11}$	90%
	GEMMA [BBE+12]	$\mu_{\nu_e} < 2.9 \cdot 10^{-11}$	90%
Accelerator ν_e-e^-	LAMPF [A+93]	$\mu_{\nu_e} < 1.1 \cdot 10^{-9}$	90%
Accelerator $(\nu_\mu, \bar{\nu}_\mu)$-e^-	BNL-E734 [A+90]	$\mu_{\nu_\mu} < 8.5 \cdot 10^{-10}$	90%
	LAMPF [A+93]	$\mu_{\nu_\mu} < 7.4 \cdot 10^{-10}$	90%
	LSND [A+01]	$\mu_{\nu_\mu} < 6.8 \cdot 10^{-10}$	90%
Accelerator $(\nu_\tau, \bar{\nu}_\tau)$-$e^-$	DONUT [S+01]	$\mu_{\nu_\tau} < 3.9 \cdot 10^{-7}$	90%
Solar ν_e-e^-	Super-Kamiokande [L+04]	$\mu_S(E_\nu \gtrsim 5 \text{ MeV}) < 1.1 \cdot 10^{-10}$	90%
	Borexino [A+08]	$\mu_S(E_\nu \lesssim 1 \text{ MeV}) < 2.8 \cdot 10^{-11}$	90%
Astrophysical ν	N. Viaux et al. [VCS+13]	$\mu_\nu \leq 4.5 \cdot 10^{-12}$	95%
	S. Arceo-Díaz et al. [ADSZJ15]	$\mu_\nu \leq 2.2 \cdot 10^{-12}$	68%

Table 2.3: Experimental constraints on neutrino magnetic moments (updated from C. Giunti and A. Studenikin [GS15]).

moments of the neutrino flavor states: $\mu_{\nu_e} < 3.9 \cdot 10^{-11}\mu_B$, $\mu_{\nu_\mu} < 5.8 \cdot 10^{-11}\mu_B$, and $\mu_{\nu_\tau} < 5.8 \cdot 10^{-11}\mu_B$.

In addition to neutrino scattering limits, astrophysical data can be used to constrain neutrino magnetic moments. G. G. Raffelt and D. S. P. Dearborn [DLSS19] suggested a method of estimating the neutrino magnetic moment by looking at the brightness of the tip of the red-giant branch, which would be increased by the non-zero magnetic moment. This type of measurement results in the strongest limit, which is currently $\mu_\nu < 2.2 \cdot 10^{-12}\mu_B$ at 68% CL.

2.3.4 Neutrino-Magnetic-Moment Contribution to CEνNS

The differential cross section of the electromagnetic neutrino-nucleus interaction for a spin-zero nucleus is [VE89]

$$\frac{d\sigma}{dT} = \frac{\pi\alpha^2\mu_\nu^2 Z^2}{m_e^2}\left(\frac{1 - T/E_\nu}{T} + \frac{T}{4E_\nu^2}\right), \tag{2.25}$$

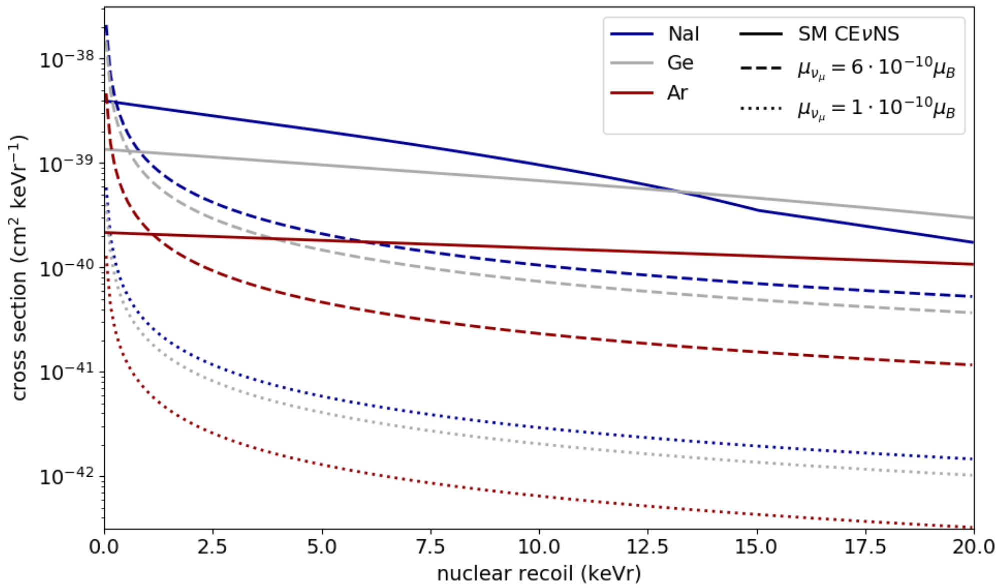

Figure 2.20: Differential CEνNS cross sections (solid lines) and electromagnetic cross sections for two non-zero neutrino-magnetic-moment values (dotted and dashed lines) as functions of nuclear recoil for three future COHERENT detectors (see Chapter 3).

where T is the nuclear recoil energy, α is the fine-structure constant, μ_ν is the neutrino magnetic moment, Z is the atomic number of the nucleus, m_e is the electron mass, and E_ν is the incoming neutrino energy. Because of the $\frac{1}{T}$ behavior of the cross section at low energy, the number of the predicted events drops as the detector threshold increases. CEνNS experiments combine very low thresholds with intense neutrino sources, thus making them also good for neutrino-magnetic-moment searches. Figure 2.20 shows πDAR flux-weighted electromagnetic cross sections alongside CEνNS cross sections for NaI, Ar, and Ge targets as functions of nuclear recoil energy.

Compared to elastic neutrino scattering on electrons, the electromagnetic neutrino cross section on nuclei is enhanced by a factor of Z. On the other hand, nuclear recoils are quenched relative to electron recoils in all detectors considered here with a quenching factor on the order of 10%. Therefore, depending on the target, a nuclear-recoil measurement can be comparable to (and even exceed) an electron-recoil one.

Chapter 3

COHERENT

The COHERENT experiment [A+a] has produced the data used in this work. The main goal of the experiment is the detection and characterization of CEνNS over a range of target nuclei. For that purpose, the COHERENT collaboration has installed multiple detectors at the Spallation Neutron Source (SNS) of the Oak Ridge National Laboratory.

Figure 3.1 shows the location of the CsI detector, as well as other current and future COHERENT detectors.

3.1 SNS

The SNS produces neutrons via a 1-GeV proton beam of high intensity impinging on a mercury target at 1.4 MW, which also generates on average 0.08–0.09 negative pions per proton, that in turn decay to muons, electrons, and neutrinos (Figure 3.2). Therefore, as a side effect, the SNS can also be used as a very intense source of neutrinos. In addition to the sheer number of neutrinos emitted by the SNS, the SNS target is thick enough for most of the pions to decay at rest, resulting in a highly isotropic source of muon neutrinos and antineutrinos and electron neutrinos with well-understood spectra (Figure 3.3).

The SNS beam bombards the target with the frequency of 60 Hz, with the resulting simulated neutrino time distributions shown in Figure 3.4. The short duty cycle of the facility allows to achieve suppression of beam-unrelated backgrounds on the order of 10^3–10^4.

ORNL provided the COHERENT collaboration with space for detectors 19–30 m

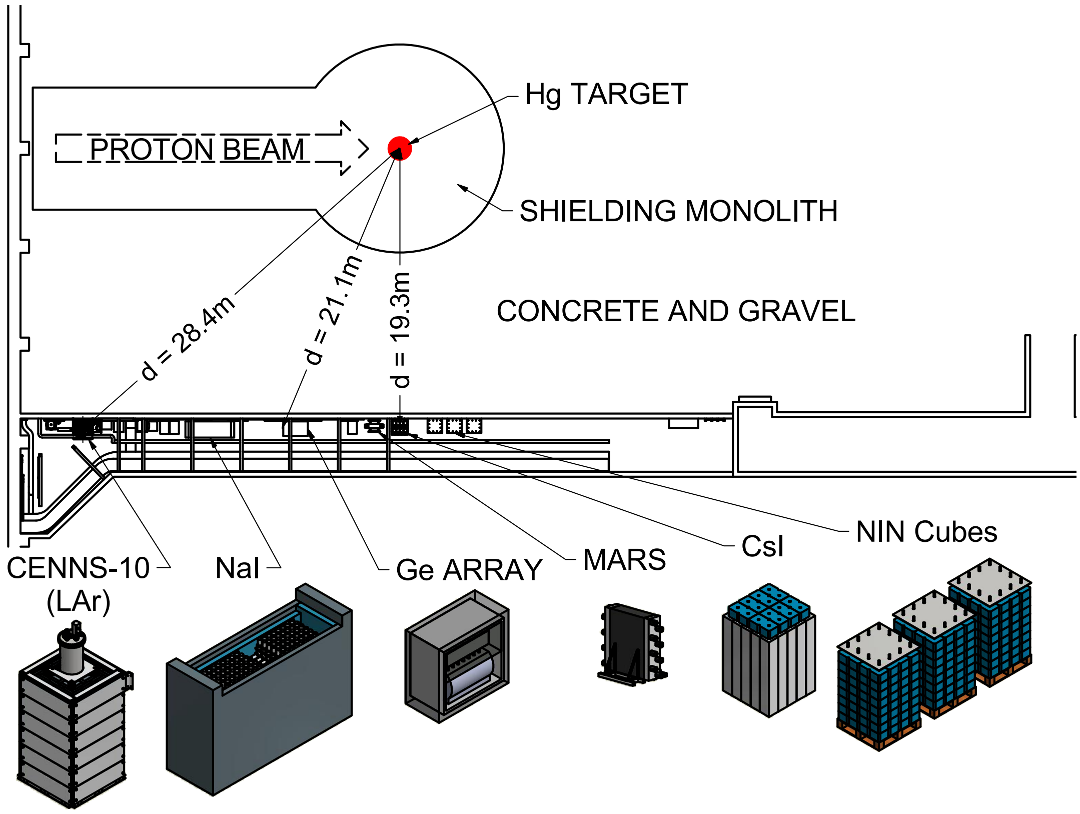

Figure 3.1: COHERENT detectors and their positon relative to the SNS [A+a].

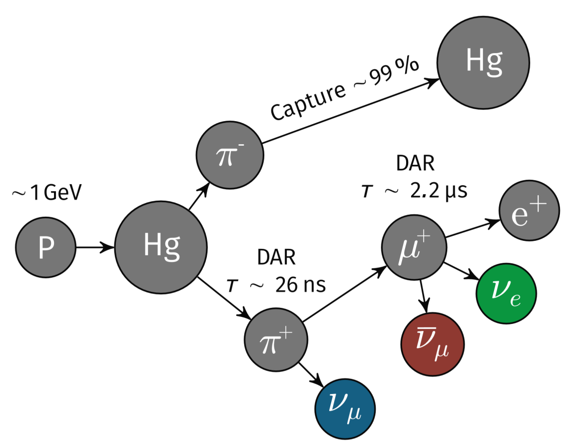

Figure 3.2: Neutrino production at the SNS [Sch17].

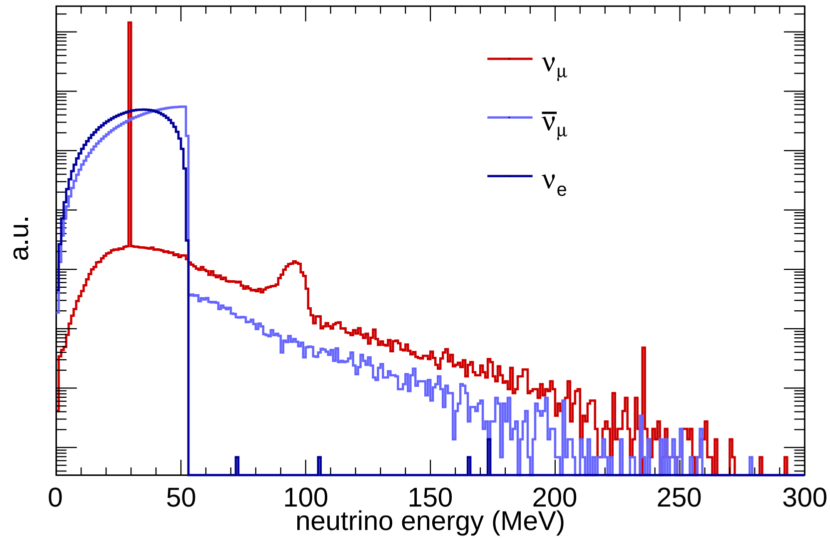

Figure 3.3: Simulated SNS neutrino energy distributions [A+a].

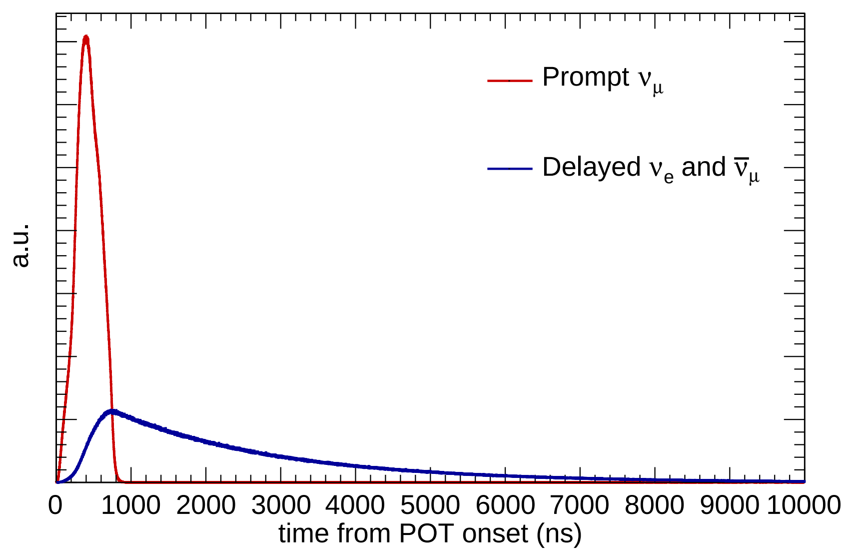

Figure 3.4: Simulated SNS neutrino timing distributions [A+a].

from the SNS target and excellent neutron shielding that has been used by the collaboration (Figure 3.1).

3.2 CsI

The first COHERENT CEνNS detector that was deployed at the SNS from 2015 to 2019 is a 14.6-kg CsI[Na] detector. The collaboration used its data to make a conclusive first observation of CEνNS in 2017 [A$^+$17c].

The detector was located 19.3 m from the SNS target. The light created inside of the CsI[Na] crystal by charged particles was read out by a PMT attached to its top face. In order to shield the detector, it was surrounded by high-density polyethylene (HDPE), lead, active muon veto, and water (schematically represented in Figure 3.5). The output from the muon veto was read out as a separate channel.

3.3 CENNS-10

CENNS-10 is the second COHERENT detector constructed for observing CEνNS. The detector was installed in a location 29 m away from the SNS target in 2016, underwent an upgrade to increase its light collection in 2017, and has been taking physics data since then [A$^+$a]. It uses argon scintillation to search for low-energy nuclear recoils.

CENNS-10 is read out by two PMTs located on the opposite sides of the cylinder containing 24 kg of the active fiducial liquid-argon mass. The detector is shielded by water, copper, and lead.

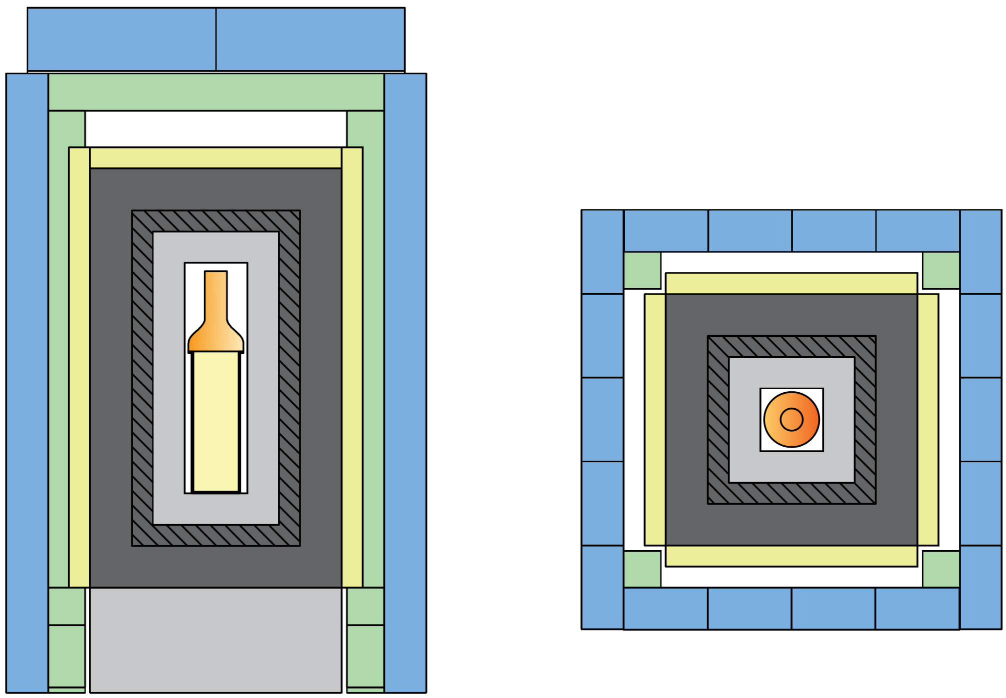

Figure 3.5: CsI detector and its shielding: light yellow is the CsI[Na] crystal, orange is the PMT, light grey is HDPE, hatched grey is low-background lead, grey is contemporary lead, yellow is the muon veto, green is aluminum, blue is water [Sch17].

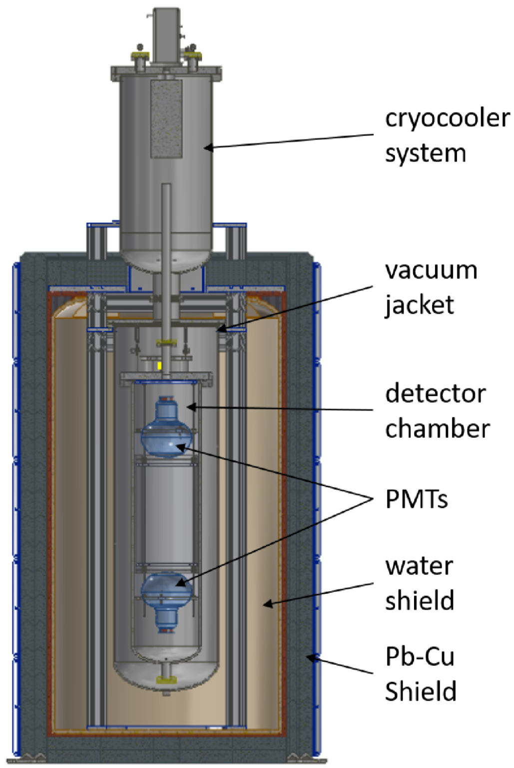

Figure 3.6: CENNS-10 detector and its shielding [A+a].

3.4 Future Detectors

COHERENT has secured funding to deploy two additional detectors, a 3388-kg NaI[Tl] detector and a 16-kg Ge detector, in the next two years and is developing a larger version of CENNS-10, CENNS-750, a 610-kg liquid-argon detector. Adding these detectors will allow COHERENT to detect CEνNS in a wide variety of isotopes (from the lightest nucleus, argon with $A = 40$, to the heaviest, cesium with $A = 133$) and start precision measurements on the scale of several years, making it a great facility for testing the Standard Model.

3.5 Backgrounds and Systematics

The backgrounds shared by all of the COHERENT detectors are usually divided into steady-state backgrounds and beam-related (or beam-on) backgrounds.

The first group affects the detectors no matter whether the beam is on or off and includes cosmic rays and 511-keV gammas from the hot-off-gas (HOG) pipe. These backgrounds are possible to measure when the beam is off and then subtract from the data. However, they still contribute to the statistical uncertainty and can flood the signal. The overburden of 8 meters of water equivalent reduces the cosmic-ray background and is not going to be changed; and to protect against the HOG-pipe background, ORNL is constructing a lead shield around the pipe that should significantly reduce the background.

The beam-on backgrounds are more complicated to mitigate. They are further divided into beam-related neutrons (BRN or prompt neutrons) and neutrino-induced neutrons (NINs). The former are generated by fast neutrons produced by the SNS and arrive shortly after the beam hits the target. Their timing is very similar to the prompt neutrinos (ν_μ), but the delayed neutrinos ($\bar{\nu}_\mu$ and ν_e) are mostly free of

Systematic	CsI	CENNS-10
Quenching factor	25%	1%
Neutrino flux	10%	10%
Form factor	5%	2%
Other	5%	9%

Table 3.1: Systematic uncertainties for the CsI and CENNS-10 measurements.

this background. Understanding this background better will help in using prompt neutrinos to study CEνNS. COHERENT has deployed several detectors (a two-plane neutron scatter camera, SciBath, and the currently running MARS detector) to measure BRN.

NINs are created by the same neutrinos that are detected via CEνNS in the target interacting in the shielding, so their timing is identical to CEνNS and cannot be used to reduce this background. In addition, the neutrino interaction itself that produces NINs in lead and iron has not been experimentally observed (the CsI neutron-background measurement [A$^+$17c] resulted in an indication of NINs in lead). To solve this problem, COHERENT has deployed the Neutrino Cubes – detectors that use liquid-scintillator cells to detect neutrons generated in the target surrounding them Currently there are two Neutrino Cubes: one with a lead target and one with an iron one. The collaboration is in the process of analyzing their data.

The systematic uncertainty that had the biggest contribution to the total error of the CsI measurement was the quenching-factor uncertainty (a comparison of several important sources of systematic uncertainties for the CsI and CENNS-10 measurements is presented in Table 3.1). The currently available data for CsI and other targets has significant variation, which motivates new measurements. The COHERENT collaboration is interested in such measurements and has several collaborators actively involved with creating and using a facility for determining quenching factors for a number of relevant isotopes at the Triangle Universities Nuclear Laboratory.

The next worst systematic uncertainty for CsI was the neutrino-flux error. The neutrino flux produced by the SNS is difficult to simulate and is known to about 10%. In order to reduce this uncertainty, the collaboration is designing a D_2O detector that is proposed to use a relatively well-known ν_e CC neutrino cross section on deuterium to independently determine the SNS neutrino flux.

All these efforts will eventually help to significantly reduce systematic uncertainties for CEνNS measurements.

Chapter 4

Data Acquisition and Processing

COHERENT has already collected a significant amount of data with many detectors. Figure 4.1 shows the evolution of statistics in terms of the number of protons on target (POT) available for each COHERENT detector. Each proton from the SNS beam hitting the target produces on average 0.08–0.09 neutrinos per flavor (this quantity depends on the average proton energy and has been slowly increasing at the SNS). Since the average proton energy and beam power are stored for each second of the time the SNS is operational, POT is easy to convert to the neutrino flux. Therefore, the black curve in Figure 4.1 is proportional to the number of neutrinos emitted by the SNS, and the curves corresponding to the COHERENT detectors are proportional to the number of neutrinos impinging upon each respective detector. Due to the SNS being a very intense source of protons, the POT delivered by the beam is orders of magnitude higher compared to other experiments detecting neutrinos produced by accelerators.

POT is plotted in Figure 4.1 for the following detectors that operated at the COHERENT site at the SNS:

- Neutron Scatter Camera – a detector that measured neutron backgrounds in 2013–2016;
- LS in CsI shield – two liquid-scintillator cells that measured neutron backgrounds directly in the CsI shielding and took data for several months before the CsI detector was installed there in 2015;
- CsI – a CsI[Na] CEνNS detector that took data in 2015-2019 and produced the

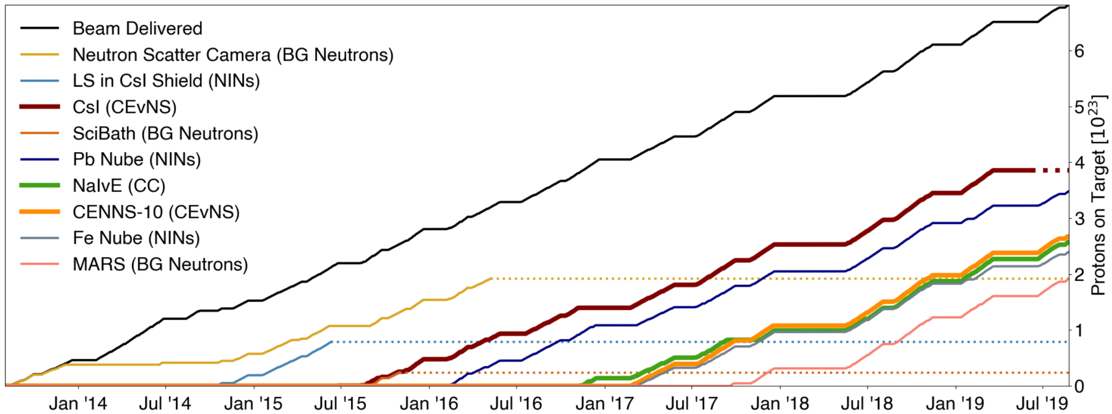

Figure 4.1: Number of protons on target recorded by different COHERENT detectors as a function of time as of August 2019. Dotted lines show detectors that have been removed. CEνNS detectors are represented by thick lines.

first observation of CEνNS;

- SciBath – a detector that measured neutron backgrounds in 2015;
- Pb Nube – the Lead Neutrino Cube, a detector measuring neutrino-induced neutrons (see Section 3.5) produced in lead, has been taking data since 2016;
- NaIvE – a NaI[Tl] detector measuring charged-current neutrino-^{127}I interactions and serving as a prototype for a larger CEνNS detector, started taking data in 2016;
- CENNS-10 – a liquid-argon CEνNS detector that has been taking data since 2017 and has produced its first CEνNS result;
- Fe Nube – the Iron Neutrino Cube, a detector measuring neutrino-induced neutrons produced in iron, has been taking data since 2017;
- MARS – a detector measuring neutron backgrounds since 2017.

4.1 Data Quality

The COHERENT collaboration implemented several systems to monitor the process of data acquisition and the status of each individual detector, as well as estimating the quality of the recorded data. The author of this work actively contributed to one such system, which is going to be described in this section.

The system has been daily processing all new data collected by the CsI, MARS, NaIvE, and Neutrino-Cube detectors, and injecting the resulting output (as well as voltages and currents for the NaIvE and Neutrino-Cube PMTs) into an InfluxDB database [inf]. Then the database is connected to Grafana [gra] that is used to visualize that information as dashboards with plots showing time evolution of the monitored parameters.

The dashboards are usually inspected daily to find and solve potential problems as quickly as possible, despite the plotted information lagging a day or two behind the data acquisition of the corresponding detectors. The simplest error that can be detected this way (and tends to happen several times a year) is an issue with the data being copied to the storage disk where it can be remotely accessed.

An example of that happening is a couple of data points missing around March 30 in Figure 4.3. That was caused by a problem with changing the data storage location and has been fixed since.

Event rates are the most useful values that are being monitored by the system and reflect well the condition of the detector and the experimental hall. Most of the rates are sensitive to the environmental gamma background and can be also used to monitor the beam activity that is correlated with the background. For instance, the beam started ramping up in the beginning of April, and that can be seen in the event rates of all of the monitored detectors (MARS, NaIvE, the Neutrino Cubes, and their corresponding Grafana dashboards).

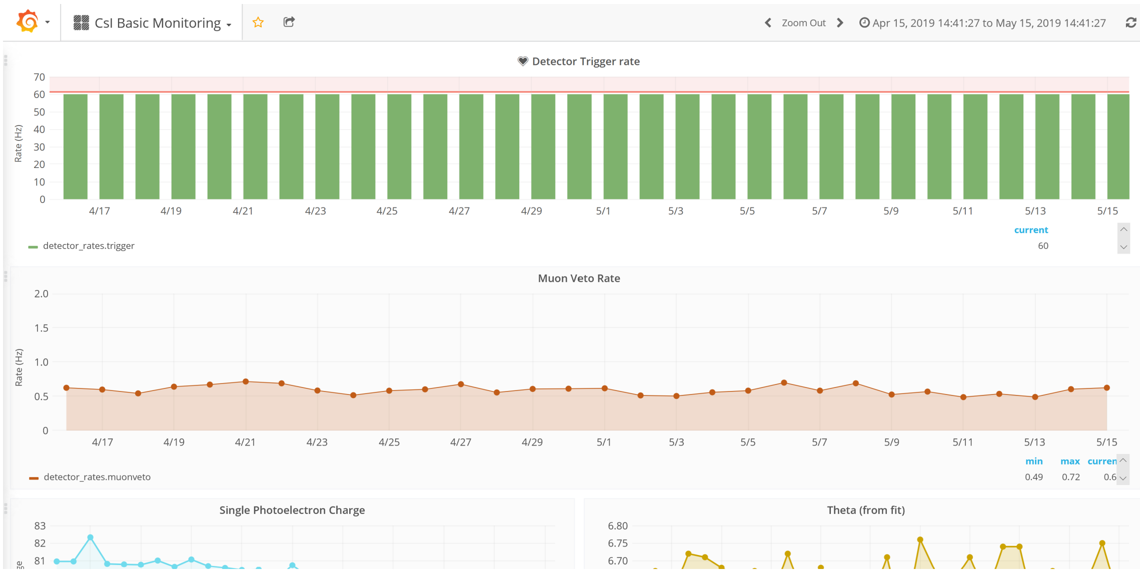

Figure 4.2: CsI Grafana dashboard.

When the event rate in one detector significantly changes independently of other detectors and the SNS beam, that may indicate a problem with this detector. In this case, looking at rates of individual PMTs or subsystems, as well as other monitored parameters such as baselines and voltages, can help understanding the issue.

4.1.1 CsI

The CsI detector has stopped taking data, and, therefore, the corresponding Grafana dashboard is no longer being updated. When it was still active, the monitored CsI values were the trigger rate, the muon-veto count rate, and two single-photoelectron fit parameters. Figure 4.2 shows the Grafana dashboard with a month of the CsI data from 2019. One data point was added every day to each plot in the dashboard.

4.1.2 MARS

The MARS Grafana dashboard (Figure 4.3) contains plots for the total trigger rate, as well as trigger rates, baselines, and baseline standard deviations for each PMT

Figure 4.3: MARS Grafana dashboard.

and timing channel ("event 39" and "event 61"). Every day a new data point with all of the monitored values is injected into the corresponding database.

4.1.3 NaIvE

The NaIvE Grafana dashboard (Figure 4.4) is used to monitor the individual-channel rates, baselines, baseline standard deviations, peak high indices (the waveform tick corresponding to the ADC maximum), and pile-up rates. Despite the NaIvE data being processed daily, the granularity of the injected data is 15 minutes.

Due to a yet-unidentified issue in the monitoring script, only about half of the data are currently being injected into the database, which manifests itself as regular several-hour-long gaps in the plots of the monitored values.

4.1.4 Neutrino Cubes

The dashboard for the Neutrino Cubes is shown in Figure 4.5 and plots the total trigger rate, run duration, and individual-channel baselines for each physics run. In

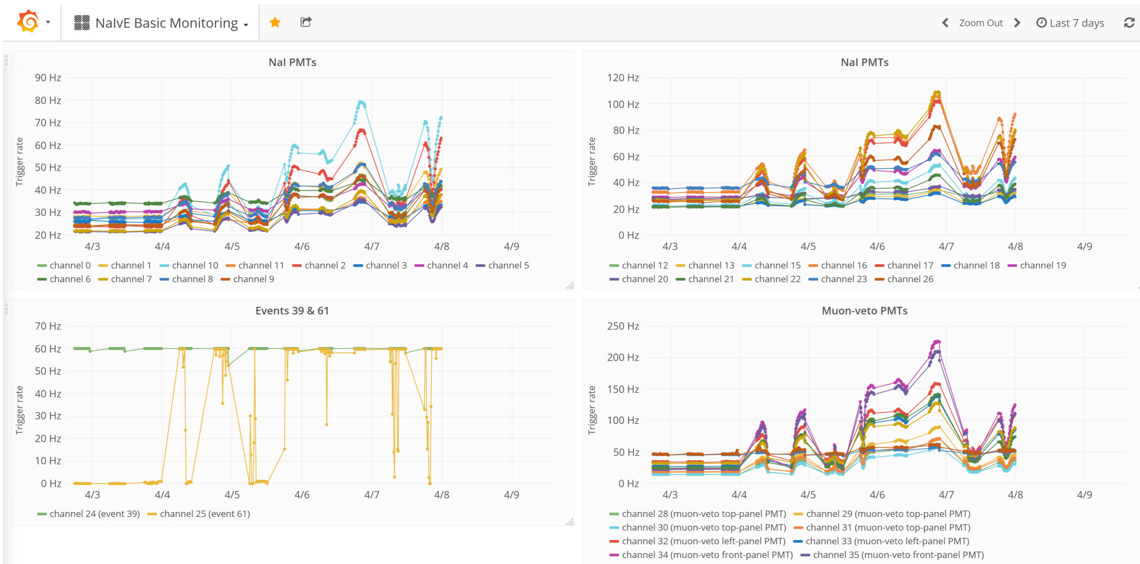

Figure 4.4: NaIvE Grafana dashboard.

addition to 24 physics runs, the Neutrino-Cube DAQ also takes three sets of check runs every day. These runs have a chance to run at the beginning of any hour and change the trigger to test each LS-cell and muon-veto channel and every muon-veto panel. The Grafana dashboard plots rates for these checks.

4.1.5 Voltages and Currents

Finally, there is a Grafana dashboard with voltages and currents for each channel of the Neutrino-Cube and NaIvE detectors (Figure 4.6). These values are being read out daily from the high-voltage supply used by the detectors and plotted for each hour.

4.2 CsI Data

Detailed information about the CsI data-taking procedures, data processing, and CEνNS analysis is available in B. J. Scholz's PhD thesis [Sch17] and G. C. Rich's PhD thesis [Ric17].

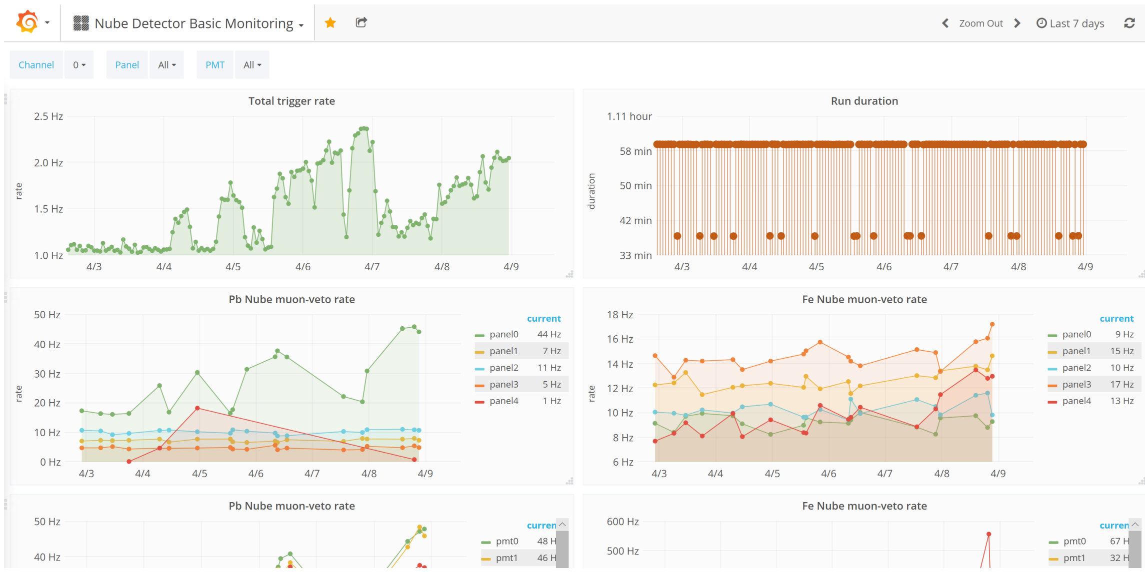

Figure 4.5: Neutrino-Cube Grafana dashboard.

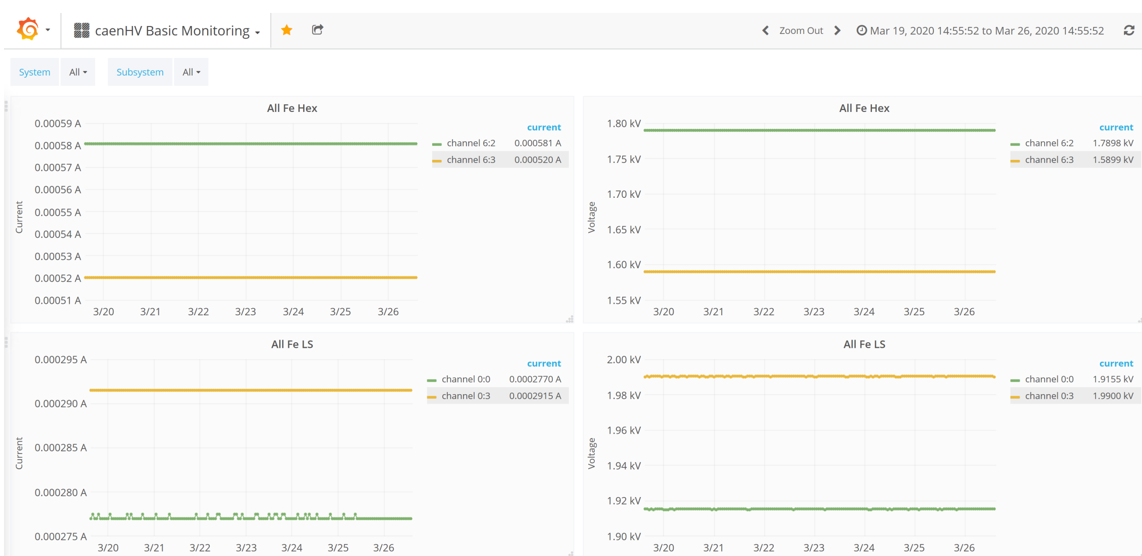

Figure 4.6: Grafana dashboard with channel voltages and currents.

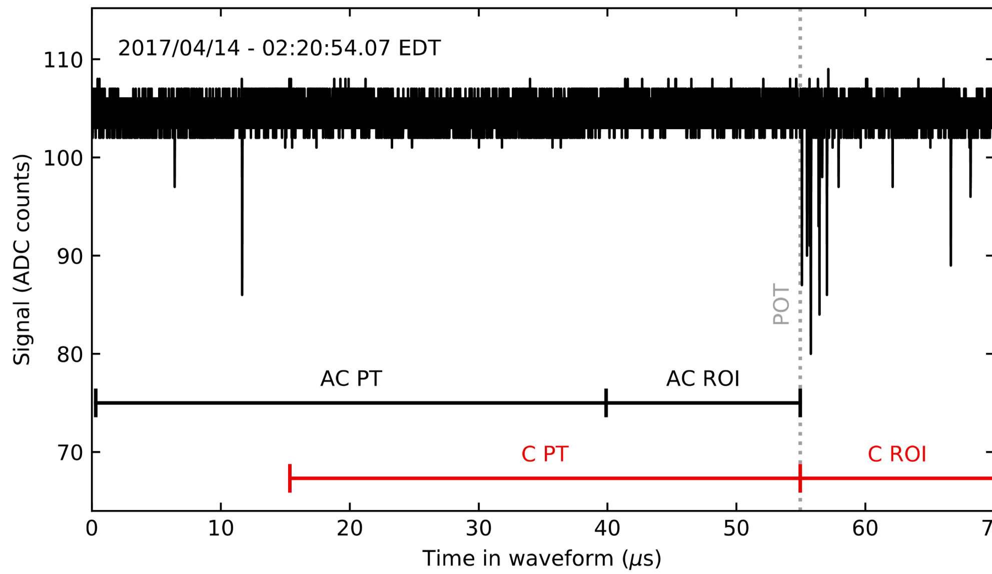

Figure 4.7: CsI waveform [Sch17]. POT is the external-trigger time, C (AC) PT is the "pretrace" region and C (AC) ROI is the region of interest for the "coincident" ("anti-coincident") analysis.

A NI-5153 digitizer was used to read out the CsI PMT (Hamamatsu R877-100) and sum the output of the muon veto. The two channels were recorded with the sampling frequency of 500 MS/s for 70-μs each time the external 60-Hz SNS trigger ("event 39") was received. The dynamic range of the electronics allowed it to process events starting with single photoelectrons to about 400 keV, with the digitizer reaching saturation around 60 keV. A linear gate was used to prevent the data acquisition from starting a 3-s reset when an event with more than 500 keVee energy deposition occurred by closing for 1.6 ms. An example of the recorded waveform is shown in Figure 4.7.

A set of cuts were applied to the data. Their effect is summarized in Figure 4.8. "Quality" cuts remove events with coincident muon-veto signals and events occurring during the dead time of the electronics or exceeding the digitizer range. The "afterglow" cut removes events with more than three peaks in the "pretrace" (a 40-μs window preceding the region of interest), reducing the number of events caused by

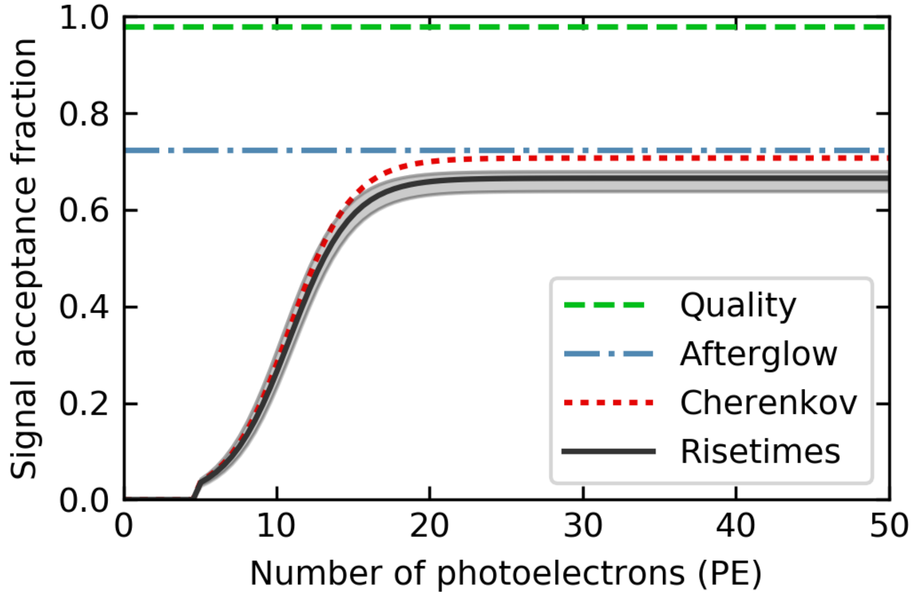

Figure 4.8: Fraction of events passing CsI cuts [A+17c]. The grey band is the uncertainty of the total acceptance curve.

a previous energy deposition. The "Cherenkov" cut requires at least 8 peaks in the regions of interest and is applied to remove events containing only Cherenkov light in the PMT window, PMT dark current and afterglow. The "Risetimes" cut uses an integrated scintillation curve constructed for each event to discard events based on their time profile.

The steady-state background was estimated by defining an additional ("anti-coincident" – AC) region of interest that ended where the primary ("coincident" – C) region of interest began, thus including none of the signal. Both regions of interest were processed in exactly the same way. The C analysis contained the signal and the steady-state background, while the AC analysis measured just the steady-state background (Figure 4.9).

The beam-related background was measured by two 1.5-liter liquid-scintillator (EJ-301) cells placed in the same shielding before the CsI detector was installed and recording 171.7 beam-on days of data. This measurement was used to constrain

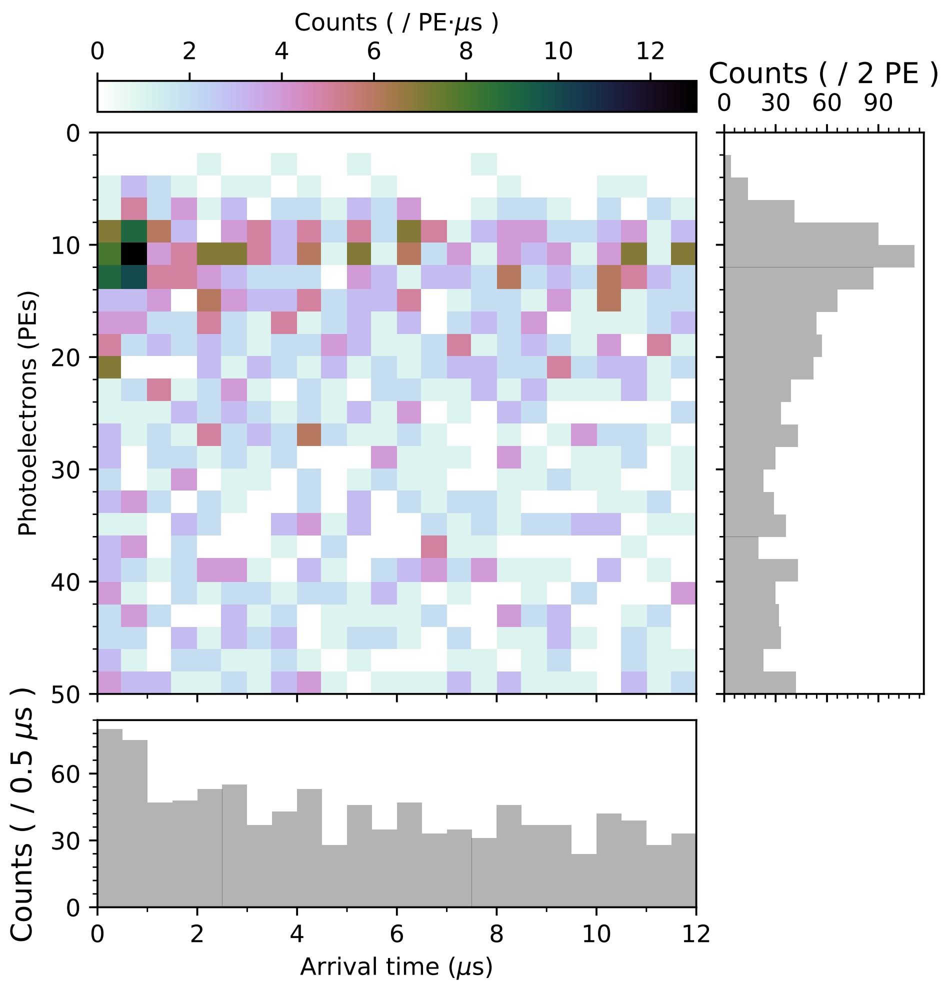

Figure 4.9: CsI steady-state background measured by looking at AC beam-on data (plotted using code and data from the COHERENT data release [A+b]).

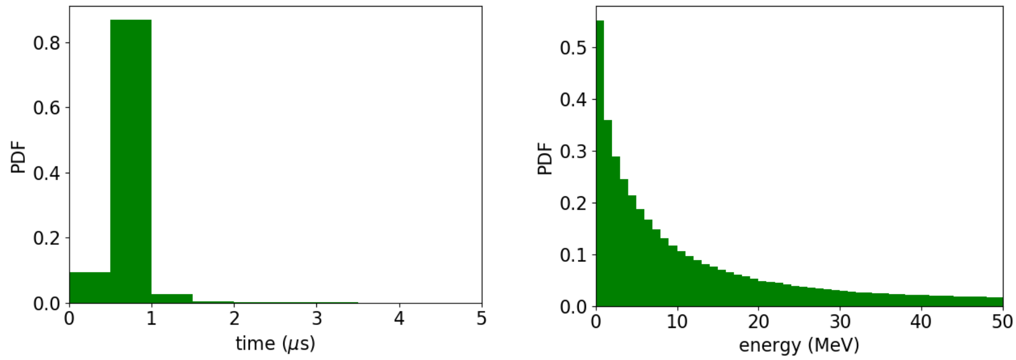

Figure 4.10: CsI beam-on-background time (left) and energy (right) distributions obtained from the EJ-301 measurement (taken from the COHERENT data release [A$^+$b]).

both prompt-neutron background (Figure 4.10) and NIN background, with the latter determined to contribute negligibly to the total background and removed from consideration for the CsI analysis. The measured prompt-neutron background was simulated in the CsI geometry and is predicted to be 0.92 ± 0.23 events/GWhr.

Subtracting the number of AC beam-on events (405) and the expected beam-on background (6) from the total count of C beam-on events (547), we obtain 136 CEνNS events. A two-dimensional likelihood fit was also performed, resulting in 134 ± 22 CEνNS events at a 6.7-σ confidence level. The fractional uncertainty of this measurement combines the flux (10%), form-factor (5%), QF (25%), and cut-acceptance (5%) uncertainties and adds up to a total of 28%. The predicted number of CEνNS events is 173.

In addition to the analysis described above, a part of the COHERENT collaboration performed another independent analysis of the same CsI data. Results obtained by that group confirmed the observation of CEνNS with similar statistical significance.

4.3 CENNS-10 Data

The first several months of data taking with the CENNS-10 detector constituted the engineering run [A+19], the data from which were used to characterize the detector and its backgrounds. After that run ended, the detector underwent an upgrade with the goal of increasing its light yield and reducing the backgrounds. The collected data were also used to constrain the CEνNS signal, resulting in a 68%-CL cross-section limit of $< 3.4 \cdot 10^{-39}$ cm^2 (about twice the SM prediction).

For the current data-taking period (after the upgrade), the CENNS-10 detector is recording 33-μs waveforms around the external trigger [A+20b]. A pulse-finding algorithm is used to find signals in the waveforms and assign them energy and timing information.

The time evolution of scintillation in argon depends on the particle ionizing it, which allows for determining the particle type based on the scintillation time profile. Therefore, in addition to integrating events to get an estimate for their energy, a fraction of energy in the first 90 ns (F_{90}) is used as a pulse-shape discrimination parameter (PSD) in this analysis. PSD makes distinguishing between nuclear and gamma recoils possible, as shown in Figure 4.11.

The event energy is reconstructed using the measured light yield of 4.6 ± 0.4 obtained from gamma calibrations with ^{83m}Kr, ^{241}Am, and ^{57}Co sources.

Events are selected for further processing based on a variety of criteria including cuts on baseline, saturation, pile-up, amount of light in each PMT, energy, time, and PSD. The acceptance curve after applying all of the cuts is shown in Figure 4.12.

The steady-state background is estimated by processing events that are recorded 14 ms after the beam trigger. Cosmogenic ^{39}Ar produces electrons inside the detector and has the largest contribution to this background component.

The beam-related-neutron background was estimated using the CENNS-10 engineering-

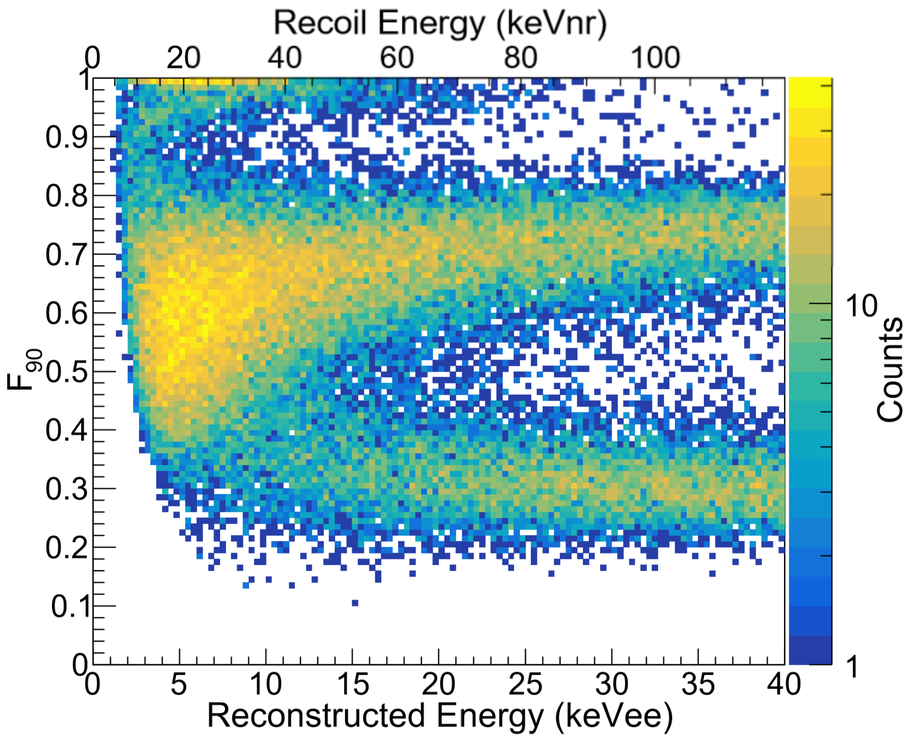

Figure 4.11: PSD distribution for CENNS-10 calibration with an AmBe source [A+20b]. Neutron recoils form a band around F_{90} of 0.7, and gammas result in F_{90} of approximately 0.3.

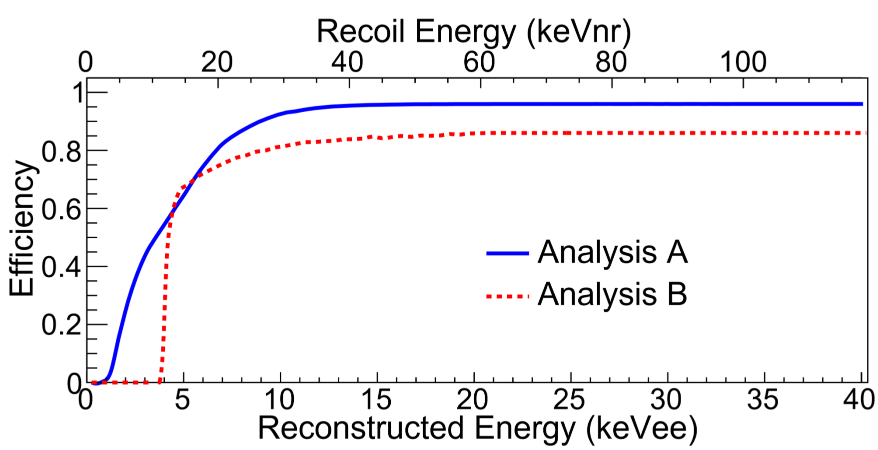

Figure 4.12: Acceptance of the two CENNS-10 analyses [A+20b]. The analysis used in this work is Analysis A.

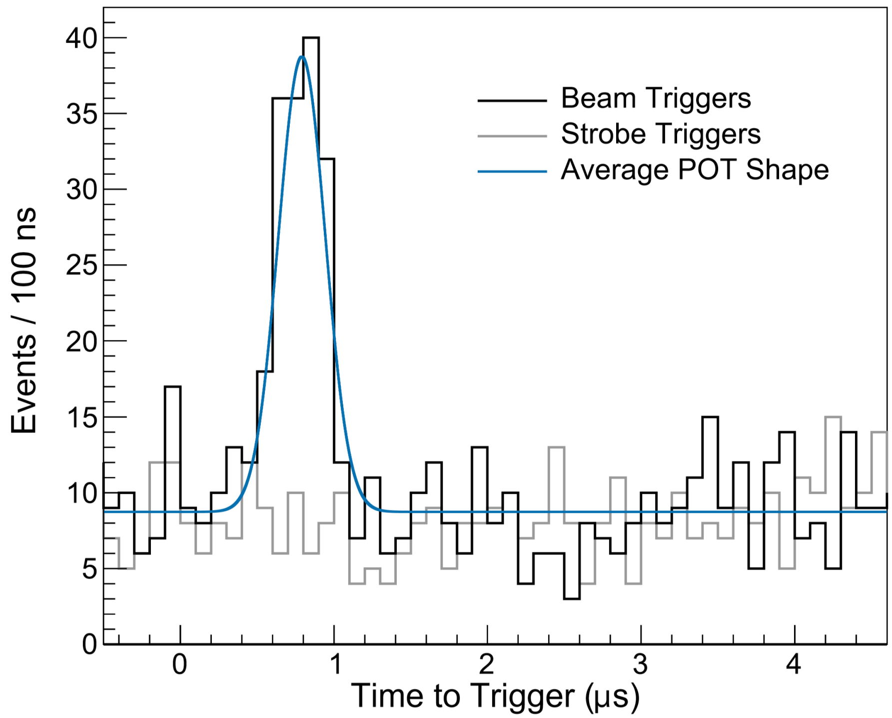

Figure 4.13: Neutron time distributions from the CENNS-10 engineering run [A+19]. Strobe triggers are events recorded with a constant time offset from the beam triggers and should not contain prompt neutrons. Average POT shape is the SNS-beam time profile.

run data [A+19], which resulted in Figure 4.13.

Unlike the CsI analysis, in which all systematic uncertainties were assigned to the measured value, the CENNS-10 analysis separates out the systematics affecting the prediction, assigning the rest to the CEνNS number calculated from the likelihood fit. The first group is divided into 1.0% from the value of the argon quenching factor, 0.8% from calibrations with gamma sources, 3.6% from the detector efficiency, 7.8% from the prompt light fraction, 2.0% due to the form-factor uncertainty, and 10% from the neutrino-flux uncertainty. The total CEνNS rate uncertainty is 13%.

The uncertainties affecting the fit result are 4.5% from the energy dependence of F_{90}, 2.7% from the neutrino arrival-time uncertainty, 5.8% from the BRN energy shape, 1.3% from the BRN arrival-time mean uncertainty, and 3.1% from the BRN arrival-time width uncertainty. The total fit uncertainty is 8.5%.

A likelihood analysis that includes the timing, energy, and PSD information from the processed data is then performed. Taking into account the aforementioned systematics, the fit result is then 159 ± 43 (stat) ± 14 (syst) CEνNS events. The expected number of CEνNS events is 128 ± 17.

As in the case of the CsI analysis, the COHERENT collaboration formed two groups to perform two CENNS-10 analyses ("A" and "B") independently of one another. The resulting CEνNS prediction, fit, and the values of uncertainties differ significantly between the two groups, but they produce similar measurements of the CEνNS cross section on argon. Only the Analysis A results were used in this work.

The B analysis prediction uncertainties are 1.0% from the value of the argon quenching factor, 4.6% from calibrations with gamma sources, 1.6% from the detector efficiency, 3.3% from the prompt light fraction, 2.0% due to the form-factor uncertainty, and 10% from the neutrino-flux uncertainty. The total CEνNS rate uncertainty is 12%.

The B analysis fit uncertainties are 3.1% from the energy dependence of F_{90}, 6.3% from the neutrino arrival-time uncertainty, 5.2% from the BRN energy shape, 5.3% from the BRN arrival-time mean uncertainty, and 7.7% from the BRN arrival-time width uncertainty. The total fit uncertainty is 13%. The fit result is 121 ± 36 (stat) ± 16 (syst) CEνNS events, while the predicted value is 101 ± 12 CEνNS events.

The CENNS-10 CEνNS measurement, like the CsI one, is within one σ of the SM prediction. However, the measured values fluctuate in the opposite directions relative to their corresponding predictions, as can be seen in Figure 4.14.

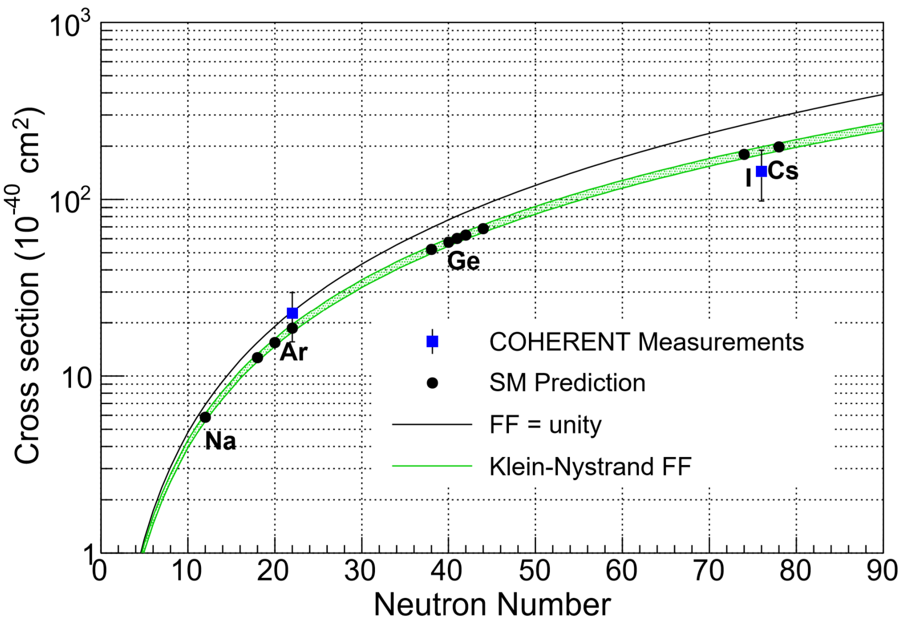

Figure 4.14: CEνNS cross sections averaged over the SNS neutrino spectrum measured by COHERENT [A$^+$20b].

Chapter 5

Physics Analysis

In this chapter, the statistical analysis used in this work is described, focusing on the definition of likelihood functions that the analysis is based on, followed by the Feynman-Cousins procedure implemented in the NSI study. Then, the NSI results are presented for the published COHERENT CsI and CENNS-10 data, as well as a combination of the produced limits. Finally, results of a sensitivity study for the future COHERENT Ge detector are presented.

5.1 Likelihood Approach

The likelihood function represents the probability of a certain set of theoretical parameters to produce the observed data. Usually it is convenient to consider the negative natural logarithm of that function instead, the negative log-likelihood (NLL). The global minimum of NLL corresponds to the set of parameters most consistent with the experimental data.

The most general NLL function used in this work combines Gaussian and Poisson bins, as well as Gaussian systematic pulls:

$$
\begin{aligned}
NLL = \min_{\{\xi_k\}} \Bigg[& \sum_{n=1}^{N} \left(\frac{R_n^{expt} - R_n^{theor} - \sum_{k=1}^{K} \xi_k c_n^k}{u_n} \right)^2 + \\
& 2 \sum_{m=N+1}^{N+M} \left(R_m^{theor} + \sum_{k=1}^{K} \xi_k c_n^k - R_m^{expt} + R_m^{expt} \log \frac{R_m^{expt}}{R_m^{theor} + \sum_{k=1}^{K} \xi_k} \right) + \\
& \sum_{k=1}^{K} \left(\frac{\xi_k}{\sigma_k} \right)^2 \Bigg]
\end{aligned}
\tag{5.1}
$$

where $\{\xi_k\}$ are the K systematic pulls [FLM$^+$02] (which follow Gaussian distributions parameterized by $(0, \sigma_k)$), $\{R_n^{expt}\}$ and $\{R_n^{theor}\}$ are the measured and predicted data bins, respectively, the first N of which are Gaussian values with the rest M following Poisson distributions, $\{u_n\}$ are the uncorrelated statistical uncertainties for the Gaussian bins, $\{c_n^k\}$ are correlations between bins, corresponding to the systematic pulls.

All theoretical parameters ($\{\theta_i\}$) consistent with the data to a certain confidence level (CL) satisfy $NLL(\{\theta_i\}) < NLL_{crit}$, where NLL_{crit} depends on the number of degrees of freedom of NLL and CL. NLL_{crit} is often assumed to be constant and, for Gaussian NLL, its values are tabulated as χ^2.

5.2 Feldman-Cousins Procedure

I followed the frequentist procedure described in G. J. Feldman and R. D. Cousins [FC98] to obtain a limit on the ϵ_{ee}^{dV} and ϵ_{ee}^{dV} NSI couplings consistent with the COHERENT CsI result [A$^+$17c]. In this section I will describe the procedure in detail and how it was used to constrain NSI.

First, I select a single set of the theoretical parameters being considered. These are the ϵ_{ee}^{dV} and ϵ_{ee}^{uV} couplings while other NSI couplings are set to 0.

The next step is to generate a possible distribution of observed number of events in the CsI detector. I assume that the observed values are distributed according to a Poisson distribution with the mean being the sum of the predicted CEνNS event rate and the total background.

After that, for each of the possible event-rate values (defined as the values lying within five standard deviations of the mean), I calculate NLL of that value being observed in the experiment with the chosen NSI couplings:

$$\begin{aligned} NLL = 2 \cdot \Bigg[& N_{exp} - \big(N_{theor}(\epsilon_{ee}^{dV}, \epsilon_{ee}^{uV}) + N_{CE\nu NS}(\epsilon_{ee}^{dV}, \epsilon_{ee}^{uV}) \cdot \alpha + B_{on} \cdot \beta \big) \\ & + N_{exp} \cdot \log \frac{N_{exp}}{N_{theor}(\epsilon_{ee}^{dV}, \epsilon_{ee}^{uV}) + N_{CE\nu NS}(\epsilon_{ee}^{dV}, \epsilon_{ee}^{uV}) \cdot \alpha + B_{on} \cdot \beta} \Bigg] \\ & + \left(\frac{\alpha}{\sigma_\alpha} \right)^2 + \left(\frac{\beta}{\sigma_\beta} \right)^2 , \end{aligned} \tag{5.2}$$

where N_{exp} is the total number of measured events, $N_{theor}(\epsilon_{ee}^{dV}, \epsilon_{ee}^{uV})$ is the total number of predicted events, $N_{CE\nu NS}(\epsilon_{ee}^{dV}, \epsilon_{ee}^{uV})$ is the CEνNS prediction, B_{on} is the beam-on background, α is the systematic parameter modifying the normalization of $N_{CE\nu NS}(\epsilon_{ee}^{dV}, \epsilon_{ee}^{uV})$, σ_α is its standard deviation, β is the systematic parameter modifying the normalization of B_{on}, and σ_β is its standard deviation. The NLL is minimized with respect to α and β.

In addition, the best possible NLL for the event-rate value is calculated by varying the NSI couplings being constrained. The latter NLL is subtracted from the former and the resulting quantity is weighted by the Poisson probability of the event rate for which it was calculated.

Thus, I get the statistical NLL distribution, which is then integrated to obtain its CDF. The NLL value for which that CDF crosses the confidence level (90% in this work) is the one that is compared to the NLL calculated for the same NSI couplings and the measurement. If the former exceeds the latter, this set of NSI couplings is allowed by the data; otherwise it is excluded.

Finally, I repeat all of these steps for every point of the parameter space being tested and obtain the allowed region at the selected confidence level.

For the CENNS-10 detector, I follow the same procedure, except the event rate is assumed to follow a Gaussian distribution with the mean defined by the predicted number of CEνNS events and the sigma being the total uncertainty of the measurement. This also necessitates using a different form for the NLL:

$$NLL = \frac{\left(N_{exp} - N_{theor}(\epsilon_{ee}^{dV}, \epsilon_{ee}^{uV})\right)^2}{\sigma^2}, \tag{5.3}$$

where N_{exp} is the observed event rate, $N_{theor}(\epsilon_{ee}^{dV}, \epsilon_{ee}^{uV})$ is the prediction, and σ is the total uncertainty.

The same steps are followed when combining the results of the two detectors as well, with the corresponding event rates assumed independent for both measurements for each set of NSI couplings and following the previously defined statistical distributions. Therefore, the combined NLL is just a sum of the individual NLLs:

$$\begin{aligned} NLL = 2 \cdot \Bigg[& N_{exp}^{CsI} - \left(N_{theor}^{CsI}(\epsilon_{ee}^{dV}, \epsilon_{ee}^{uV}) + N_{CE\nu NS}(\epsilon_{ee}^{dV}, \epsilon_{ee}^{uV}) \cdot \alpha + B_{on} \cdot \beta\right) \\ & + N_{exp}^{CsI} \cdot \log \frac{N_{exp}^{CsI}}{N_{theor}^{CsI}(\epsilon_{ee}^{dV}, \epsilon_{ee}^{uV}) + N_{CE\nu NS}(\epsilon_{ee}^{dV}, \epsilon_{ee}^{uV}) \cdot \alpha + B_{on} \cdot \beta} \Bigg] \\ & + \left(\frac{\alpha}{\sigma_\alpha}\right)^2 + \left(\frac{\beta}{\sigma_\beta}\right)^2 \\ & + \frac{\left(N_{exp}^{LAr} - N_{theor}^{LAr}(\epsilon_{ee}^{dV}, \epsilon_{ee}^{uV})\right)^2}{\sigma^2}, \end{aligned} \tag{5.4}$$

where $N_{exp}^{CsI,LAr}$ are the observed event rates and $N_{theor}^{CsI,LAr}(\epsilon_{ee}^{dV}, \epsilon_{ee}^{uV})$ are the predicted event rates for the CsI and LAr detectors, respectively, with the rest of the parameters being defined under equations 5.2, 5.3.

5.3 Results

5.3.1 NSI with Feldman-Cousins Procedure

CsI

The predicted SM rate for the 2017 CsI data, N_{SM}, is 173. The two considered NSI couplings, ϵ_{ee}^{dV} and ϵ_{ee}^{uV}, modify it in a way shown in Figure 2.14. The black solid lines denote NSI values that result in the same rate as the SM prediction. This figure also defines the NSI parameter space I will be working with in this section.

The next step is calculating NLL for each point of the parameter space:

$$NLL = \min_{\alpha,\beta} \Bigg\{ 2 \cdot \Bigg[N_{exp} - \Big(N_{theor}(\epsilon_{ee}^{dV}, \epsilon_{ee}^{uV}) + N_{CE\nu NS}(\epsilon_{ee}^{dV}, \epsilon_{ee}^{uV}) \cdot \alpha + B_{on} \cdot \beta \Big) \\ + N_{exp} \cdot \log \frac{N_{exp}}{N_{theor}(\epsilon_{ee}^{dV}, \epsilon_{ee}^{uV}) + N_{CE\nu NS}(\epsilon_{ee}^{dV}, \epsilon_{ee}^{uV}) \cdot \alpha + B_{on} \cdot \beta} \Bigg] \\ + \left(\frac{\alpha}{\sigma_\alpha} \right)^2 + \left(\frac{\beta}{\sigma_\beta} \right)^2 \Bigg\}, \tag{5.5}$$

where N_{exp} is the total number of measured events, 547; $N_{theor}(\epsilon_{ee}^{dV}, \epsilon_{ee}^{uV}) = N_{CE\nu NS}(\epsilon_{ee}^{dV}, \epsilon_{ee}^{uV}) + B_{on} + B_{ss}$ is the total number of predicted events; B_{on} is the number of beam-on background events, 6; B_{ss} is the total number of steady-state background events, 405; σ_α is the RMS of the CEνNS normalization systematic uncertainty, 0.28; σ_β is the RMS of the B_{on} normalization systematic uncertainty, 0.25. The resulting values are plotted in Figure 5.1.

Next, the FC procedure is followed to obtain NLL_{crit} at 90% CL, shown in Figure 5.2; and, finally, the NSI couplings allowed by the data at 90% CL (for which $NLL(\epsilon_{ee}^{dV}, \epsilon_{ee}^{uV}) < NLL_{crit}(\epsilon_{ee}^{dV}, \epsilon_{ee}^{uV})$) are plotted in Figure 5.3. The resulting band of allowed values is significantly narrower than the published NSI result, which repre-

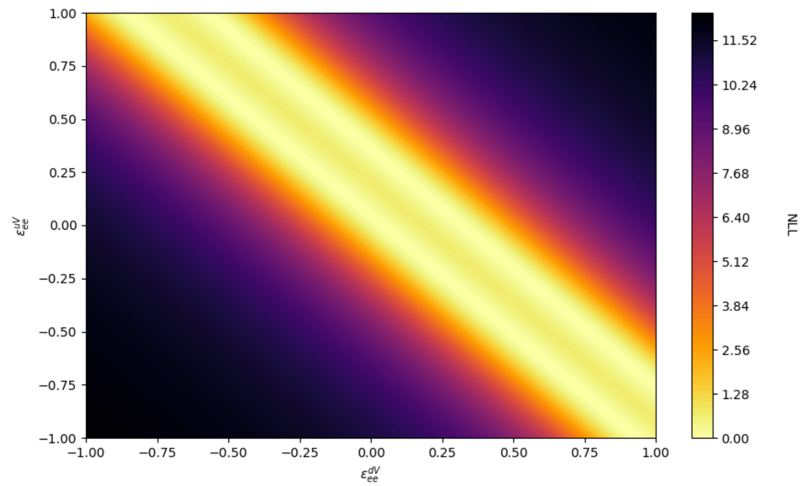

Figure 5.1: NLL dependence on the NSI couplings for the COHERENT CsI detector.

sents the power of the Feldman-Cousins technique.

CENNS-10

The same procedure is followed for the COHERENT CENNS-10 detector. Figure 5.4 shows the CEνNS rate modification for natural argon, with N_{SM} assumed to be 128. This plot is slightly different from Figure 2.14 because of different numbers of up and down quarks in argon isotopes compared to cesium and iodine.

The likelihood form in this case is the following:

$$NLL = \frac{\left(N_{SM} - N_{CE\nu NS}(\epsilon_{ee}^{dV}, \epsilon_{ee}^{uV})\right)^2}{\sigma^2}, \tag{5.6}$$

where σ is the total measurement uncertainty, 46.2. Figure 5.5 shows the calculated NLL values.

FC-calculated 90% NLL_{crit} values are plotted in Figure 5.6, which, due to simplicity of equation 5.6 are easy to interpret and transition from around 2.7 (critical χ^2 value for one degree of freedom and 10% p-value) in the regions of the parameter

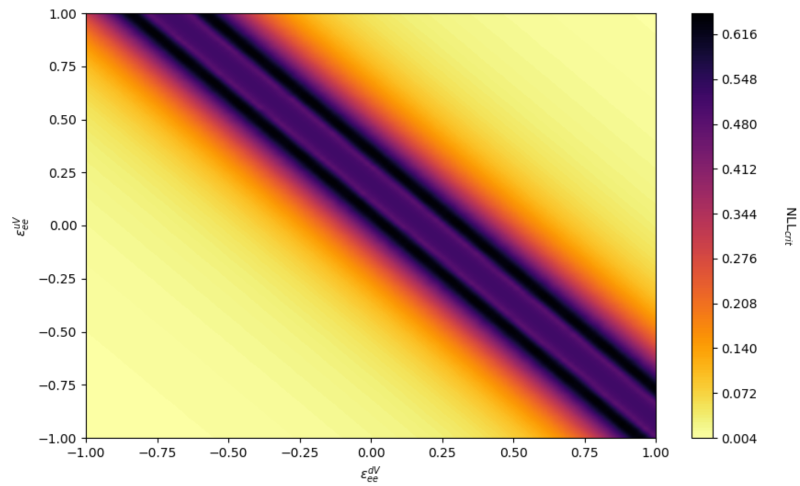

Figure 5.2: 90%-CL NLL_{crit} dependence on the NSI couplings for the COHERENT CsI detector.

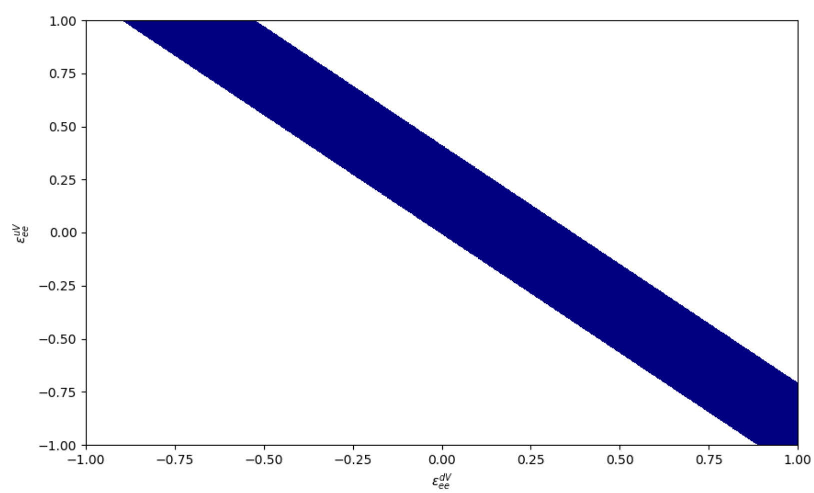

Figure 5.3: The NSI couplings allowed by the COHERENT CsI measurement at 90% CL.

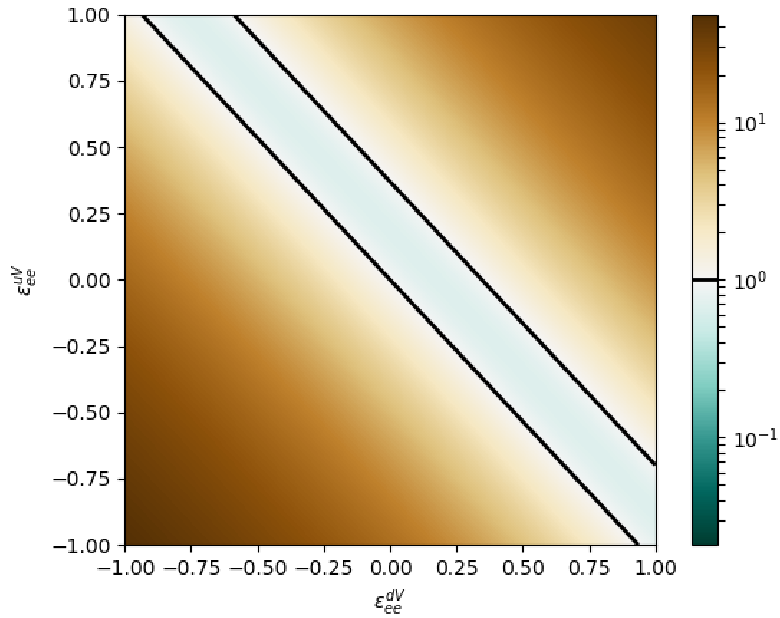

Figure 5.4: Rate modification dependence on the NSI couplings for the COHERENT CENNS-10 detector. Solid lines correspond to the values producing the SM rate.

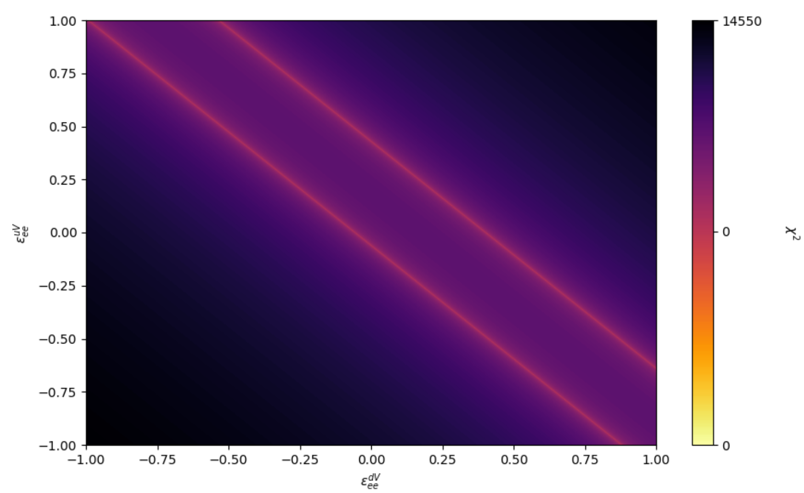

Figure 5.5: NLL dependence on the NSI couplings for the COHERENT CENNS-10 detector.

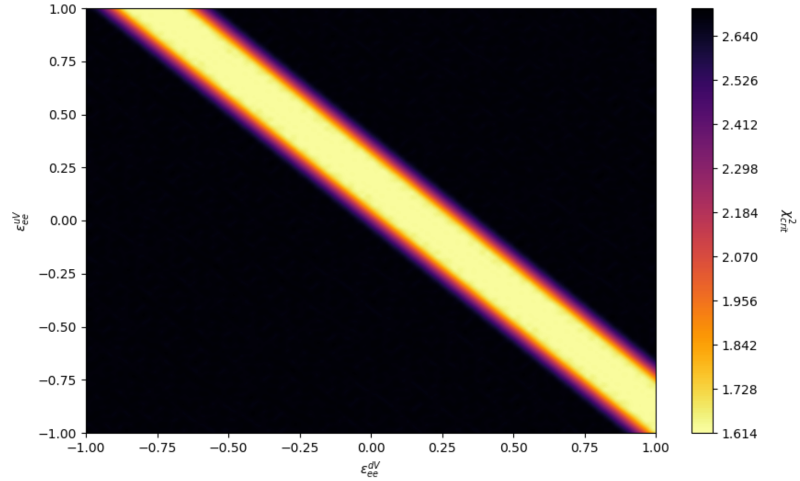

Figure 5.6: 90%-CL NLL_{crit} dependence on the NSI couplings for the COHERENT CENNS-10 detector.

space where NSI enhance the rate to about 1.6 (critical χ^2 value for one degree of freedom and 20% p-value) where NSI maximally suppress it.

$NLL(\epsilon_{ee}^{dV}, \epsilon_{ee}^{uV}) < NLL_{crit}(\epsilon_{ee}^{dV}, \epsilon_{ee}^{uV}))$ again represents the NSI parameter space region allowed by the CENNS-10 measurement prediction at 90% CL. The area is larger than the CsI one due to the total uncertainty being bigger in this case.

Combining CsI and CENNS-10

The log-likelihood in this case is just the sum of individual NLL in equations 5.5 and 5.3:

$$\begin{aligned} NLL = \min_{\alpha,\beta} \Bigg\{ 2 \cdot \Bigg[& N_{exp}^{CsI} - \big(N_{theor}^{CsI}(\epsilon_{ee}^{dV}, \epsilon_{ee}^{uV}) + N_{CE\nu NS}^{CsI}(\epsilon_{ee}^{dV}, \epsilon_{ee}^{uV}) \cdot \alpha + B_{on} \cdot \beta\big) \\ & + N_{exp}^{CsI} \cdot \log \frac{N_{exp}^{CsI}}{N_{theor}^{CsI}(\epsilon_{ee}^{dV}, \epsilon_{ee}^{uV}) + N_{CE\nu NS}^{CsI}(\epsilon_{ee}^{dV}, \epsilon_{ee}^{uV}) \cdot \alpha + B_{on} \cdot \beta} \Bigg] \\ & + \left(\frac{\alpha}{\sigma_\alpha}\right)^2 + \left(\frac{\beta}{\sigma_\beta}\right)^2 \Bigg\} + \frac{\big(N_{SM}^{LAr} - N_{CE\nu NS}^{LAr}(\epsilon_{ee}^{dV}, \epsilon_{ee}^{uV})\big)^2}{\sigma^2}, \end{aligned} \tag{5.7}$$

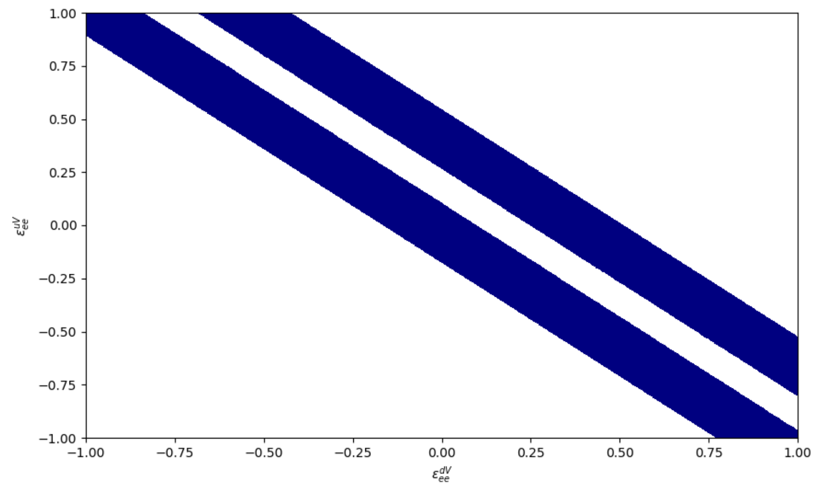

Figure 5.7: The NSI couplings allowed by the COHERENT CENNS-10 measurement at 90% CL.

where the CsI and LAr superscripts denote rates of the COHERENT CsI and CENNS-10 detectors, respectively.

Calculating two-bin 90%-CL NLL_{crit} using the FC method takes tens of hours rather than minutes in the single-bin case, making this method difficult to scale to add more detectors or bin data in energy or time. However, the FC result for NLL defined in equation 5.7 is shown in Figure 5.9. The resulting allowed NSI couplings are plotted in Figure 5.10.

Figure 5.11 shows the comparison between NSI couplings allowed by the individual detectors and the combination, all at 90% CL. The combination provides a weaker constraint than the individual limits due to the opposite fluctuations in the data relative to the SM predictions for the corresponding measurements.

5.3.2 Neutrino Magnetic Moment

This study uses information from a proposal for a COHERENT Ge detector to estimate its potential for measuring the neutrino magnetic moment.

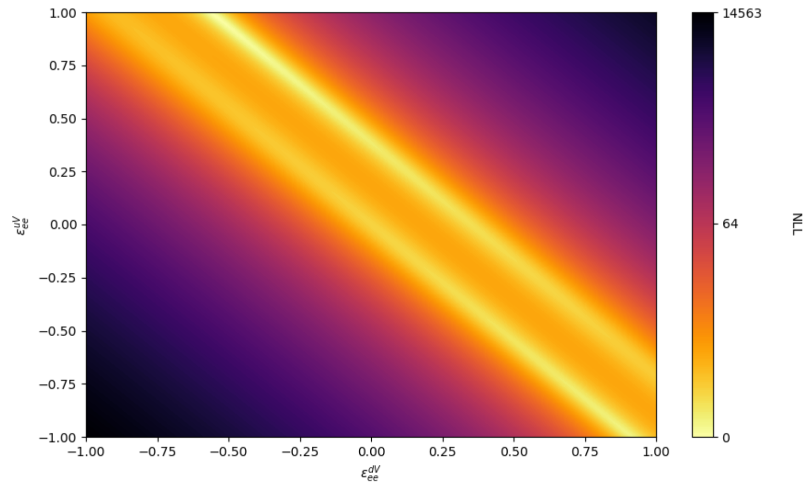

Figure 5.8: NLL dependence on the NSI couplings for the COHERENT CsI–CENNS-10 combination.

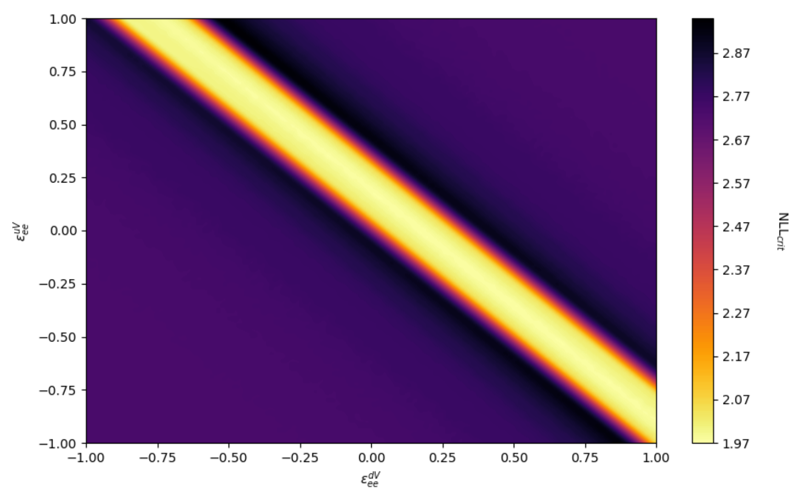

Figure 5.9: 90%-CL NLL_{crit} dependence on the NSI couplings for the COHERENT CsI-CENNS-10 combination.

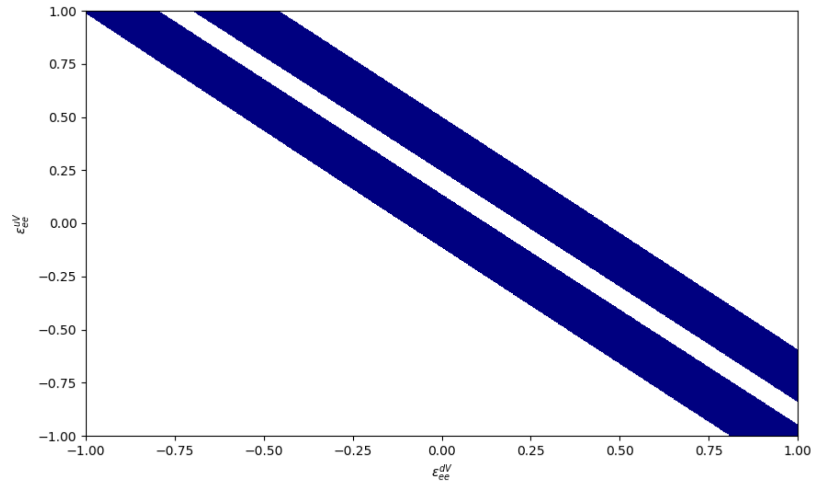

Figure 5.10: The NSI couplings allowed by the COHERENT combination of the CsI and CENNS-10 measurements at 90% CL.

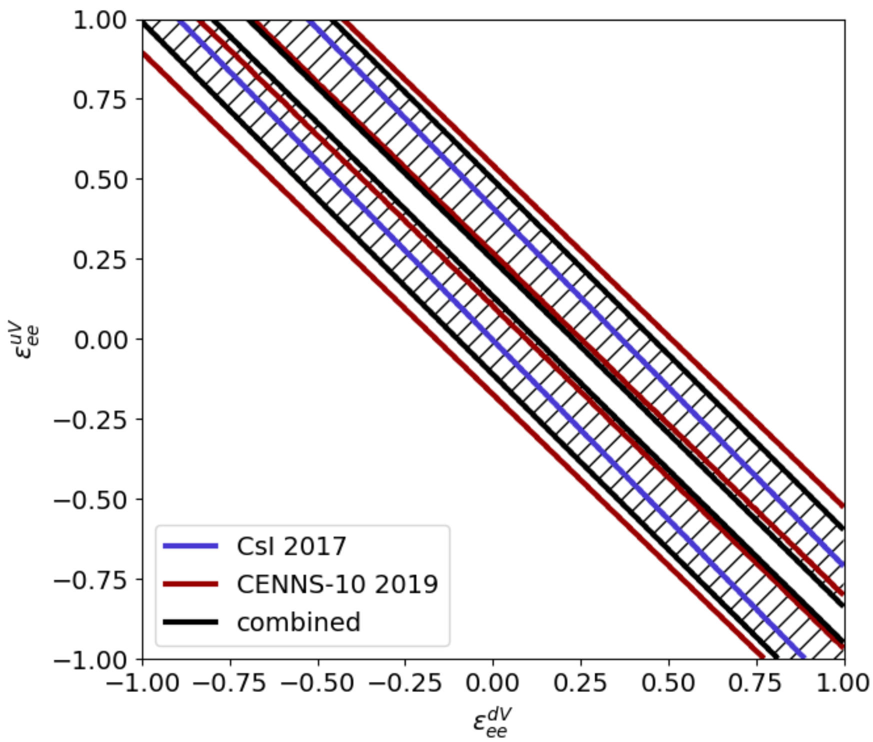

Figure 5.11: NSI couplings allowed by the COHERENT CsI and CENNS-10 measurements at 90% CL (the values between the corresponding lines for the individual limits and the hatched region for the combination).

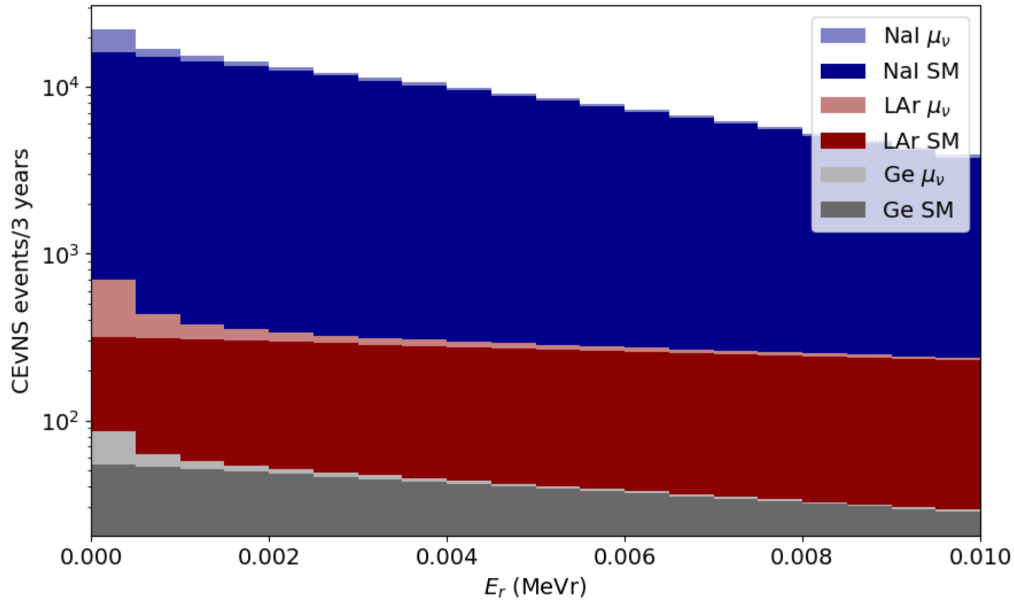

Figure 5.12: Calculated event rates for the COHERENT NaI, LAr, and Ge detectors for 3 years of data taking. μ_ν is the $\mu_{\nu_\mu} = \mu_{\bar{\nu}_\mu} = 6 \cdot 10^{-10}\mu_B$ contribution to the event rates, and SM is the SM CEνNS prediction.

Figure 5.12 shows the expected CEνNS spectra with and without the non-zero neutrino magnetic moment, $\mu_{\nu_\mu} = \mu_{\bar{\nu}_\mu} = 6 \cdot 10^{-10}\mu_B$ for several COHERENT detectors. Despite other detectors having significantly more predicted events, the Ge detector is designed to have the best energy resolution and lowest threshold, which would give it a better opportunity for observing the neutrino magnetic moment, so a more detailed magnetic-moment sensitivity study is presented in this section for that detector.

A three-year predicted energy spectrum for the COHERENT Ge detector is shown in Figure 5.13. The salmon-colored part of the spectrum is the predicted CEνNS signal, while the cyan is the contribution from $\mu_{\nu_\mu} = \mu_{\bar{\nu}_\mu} = 6 \cdot 10^{-10}\mu_B$ in the first several bins. The steady-state background is taken from G. K. Giovanetti et al. [G+15], and the beam-related-neutron background is estimated by COHERENT

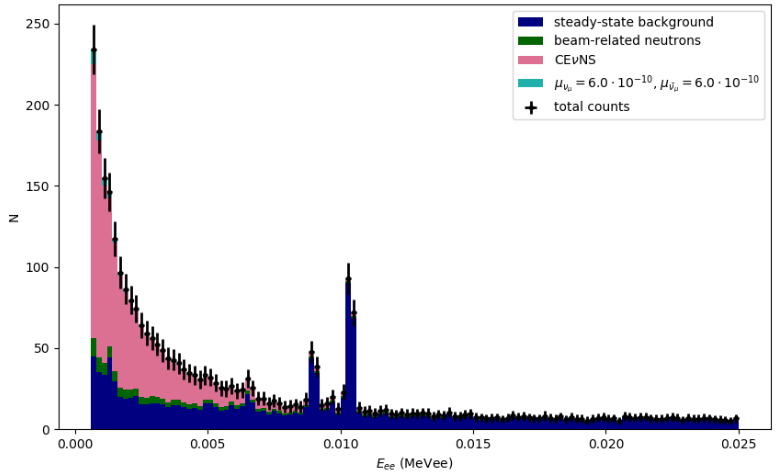

Figure 5.13: Predicted COHERENT Ge spectrum including the neutrino-magnetic-moment contribution.

from the CsI background measurement.

Because of that spectral dependence of the electromagnetic scattering, using the full spectrum should provide a significantly better measurement of the neutrino magnetic moment than a single-bin analysis. Therefore, the log-likelihood form used is

$$NLL = \min_{\phi,\beta,\rho,\kappa} \sum_{k=1}^{K} \Bigg\{ N_k^{exp} - \left[N_k^{theor}(\mu_\nu,\rho) + N_k^{CE\nu NS}(\mu_\nu,\rho)\cdot(\phi+\kappa) + B_k^{on}\cdot(\phi+\beta)\right]$$
$$+ N_k^{exp}\cdot\log\frac{N_k^{exp}}{N_k^{theor}(\mu_\nu,\rho) + N_k^{CE\nu NS}(\mu_\nu,\rho)\cdot(\phi+\kappa) + B_k^{on}\cdot(\phi+\beta)}$$
$$+ \left(\frac{\phi}{\sigma_\phi}\right)^2 + \left(\frac{\beta}{\sigma_\beta}\right)^2 + \left(\frac{\rho}{\sigma_\rho}\right)^2 + \left(\frac{\kappa}{\sigma_\kappa}\right)^2 \Bigg\}, \tag{5.8}$$

where K is the number of energy bins; $N_k^{exp} = N^{CE\nu NS}(\mu_{\nu,0},0) + B_k^{on} + B_k^{ss}$ is the k-th measurement bin, assuming $\mu_{\nu,0}$ to be the true value of the muon-neutrino magnetic moment; B_k^{ss} is the k-th steady-state-background bin; B_k^{on} is the k-th beam-on-

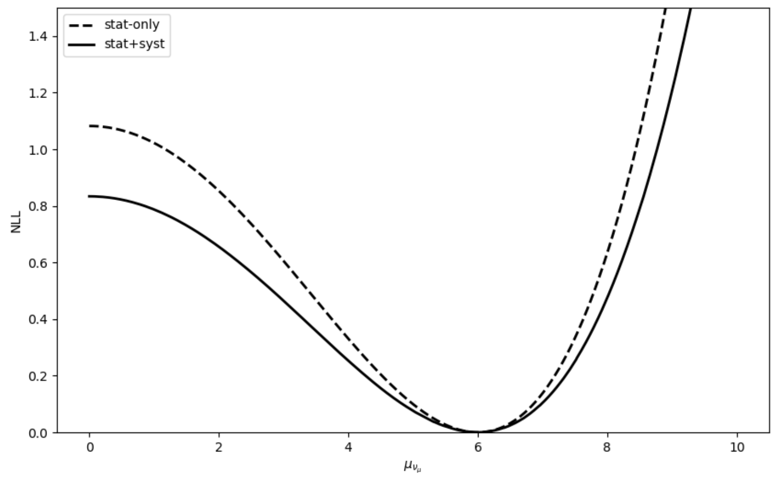

Figure 5.14: NLL dependence on neutrino-magnetic-moment values for the predicted COHERENT Ge spectrum assuming a non-zero neutrino magnetic moment.

background bin; $N_k^{theor}(\mu_\nu, \rho) = N^{CE\nu NS}(\mu_\nu, \rho) + B_k^{on} + B_k^{ss}$ is the prediction for the total rate in the k-th bin; σ_ϕ is the RMS of the flux systematic uncertainty, assumed to be 0.1; σ_β is the RMS of the beam-on-background normalization systematic uncertainty, taken to be 0.25; σ_ρ is the RMS of the form-factor systematic uncertainty obtained by varying the nuclear radius, it is assumed to be 0.03; σ_κ is the RMS of the energy-independent quenching-factor systematic uncertainty, which is assumed to be 0.039.

Varying the neutrino-magnetic-moment value, I get the solid curve shown in Figure 5.14 for NLL and taking the histogram from Figure 5.13 as the measured energy spectrum. 0 is within 1 σ of the NLL minimum, making a robust measurement of a neutrino magnetic moment on the order of 10^{-10}–$10^{-9}\mu_B$ impossible with the current assumptions.

Inverting the procedure and using 0 as the true value of the neutrino magnetic moment, the solid curve in Figure 5.15 is obtained. The value of the neutrino magnetic moment where that curve intersects with a constant NLL_{crit} value of 2.71 (the

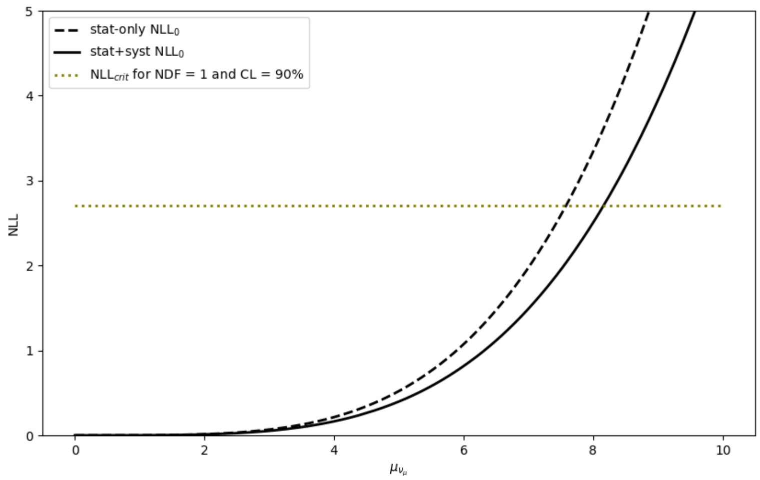

Figure 5.15: NLL dependence on neutrino-magnetic-moment values for the predicted COHERENT Ge spectrum assuming no neutrino magnetic moment.

χ^2 value for one degree of freedom and a p-value of 0.1) is the predicted 90%-CL constraint for the neutrino magnetic moment obtained from a possible COHERENT Ge measurement with the aforementioned assumptions. The resulting value is about $8 \cdot 10^{-10}\mu_B$.

Chapter 6

Conclusions

6.1 NSI

Applying the FC technique to the problem of constraining a pair of NSI couplings while other NSI couplings are set to 0 produces a significantly better result even with the same data and assumptions: the calculated band of allowed values is 1.4 times narrower than the published COHERENT CsI result [A+17c].

However, as the limit becomes stronger, the allowed values get closer to the order of other couplings, which invalidates the justification for assuming them to be 0 in the analysis. At that point, more NSI couplings have to be added, increasing the dimensionality of the problem. Because of that, just as for other possible improvements discussed later, the FC method quickly becomes too computationally expensive to use.

Performing the same procedure with the recently published COHERENT CENNS-10 CEνNS data [A+20b] results in two bands of allowed NSI values that are together 1.1 times narrower than the 2017 COHERENT NSI result [A+17c]. However, because of the qualitatively different double-band structure, the new limit allows some of the values that were excluded by previous constraint.

Using the FC procedure to combine the two measurements produces two allowed bands that are together 1.2 times narrower than the original constraint [A+17c] and look like the average of the two individual limits. This effect is likely caused by the opposite fluctuations relative to the SM predictions in the individual CEνNS measurements (see Figure 4.14). Obtaining the combined limit is also about 200 times slower than the individual constraints, which may make improving the constraint by adding more data prohibitively slow by this method.

The FC method implemented here performs a raster scan of the parameter space. The resulting plots show that this is not efficient, since a significant amount of processing power is used on calculating likelihood distributions for points in the parameter space that result in very similar critical values. A possibility for considerable optimization exists in varying the density of tested points in the parameter space, calculating critical values more often where the output quickly changes and interpolating more where it does not.

Another way forward is to split a single measurement into bins in time and energy. In addition to constraining light-mediator NSI, this will also result in a degree of separation for different neutrino flavors in πDAR experiments, affecting heavy-mediator NSI limits as well.

More careful treatment of systematic uncertainties can also improve the result. Several of the contributing systematics are correlated between different detectors in COHERENT, such as the uncertainty on the neutrino flux, nuclear radius, or beam-related backgrounds. The effects of correlation are expected to be small, but could be more important as precision improves.

6.2 Neutrino Magnetic Moment

CEνNS experiments provide a good opportunity to directly constrain neutrino magnetic moments. Unfortunately, this requires a capability of observing nuclear recoils at the low-energy end of CEνNS, and even CEνNS has not yet been observed by most detectors constructed to measure the interaction due to the difficulty of the task. However, the field of CEνNS detector development has been rapidly progressing, now boosted by the first measurement, so the possibility for competitive neutrino-magnetic-moment limits with CEνNS exists for future-generation detectors.

As for CEνNS detectors being deployed within about a year, the COHERENT Ge detector is one of the more promising projects for neutrino-magnetic-moment searches with CEνNS, and its expected 90%-CL limit calculated in this work is $\mu_{\nu_\mu} < 8 \cdot 10^{-10} \mu_B$, which is weaker than the best current constraint, $\mu_{\nu_\mu} < 5.8 \cdot 10^{-11} \mu_B$ from the Borexino measurement, but would represent a limit based on a different process.

On the other hand, performing a similar study for other COHERENT detectors is useful for estimating their capability for this measurement, and possibly designing a detector much better suited for it.

Bibliography

[A$^+$a] D. Akimov et al. COHERENT 2018 at the Spallation Neutron Source.

[A$^+$b] D. Akimov et al. COHERENT Collaboration data release from the first observation of coherent elastic neutrino-nucleus scattering.

[A$^+$c] Joshua Albert et al. SNOwGLoBES: SuperNova Observatories with GLoBES.

[A$^+$d] C.A. Argelles et al. White Paper on New Opportunities at the Next-Generation Neutrino Experiments (Part 1: BSM Neutrino Physics and Dark Matter).

[A$^+$90] L.A. Ahrens et al. Determination of electroweak parameters from the elastic scattering of muon-neutrinos and anti-neutrinos on electrons. *Phys.Rev.D*, 41:3297–3316, 1990.

[A$^+$93] R.C. Allen et al. Study of electron-neutrino electron elastic scattering at LAMPF. *Phys.Rev.D*, 47:11–28, 1993.

[A$^+$01] L.B. Auerbach et al. Measurement of electron - neutrino - electron elastic scattering. *Phys.Rev.D*, 63:112001, 2001.

[A$^+$08] C. Arpesella et al. Direct Measurement of the Be-7 Solar Neutrino Flux with 192 Days of Borexino Data. *Phys.Rev.Lett.*, 101:091302, 2008.

[A$^+$13] D.Yu. Akimov et al. Prospects for observation of neutrino-nuclear neutral current coherent scattering with two-phase Xenon emission detector. *JINST*, 8:P10023, 2013.

[A$^+$17a] G. Agnolet et al. Background Studies for the MINER Coherent Neutrino Scattering Reactor Experiment. *Nucl. Instrum. Meth. A*, 853:53–60, 2017.

[A$^+$17b] M. Agostini et al. Limiting neutrino magnetic moments with Borexino Phase-II solar neutrino data. *Phys.Rev.D*, 96(9):091103, 2017.

[A$^+$17c] D. Akimov et al. Observation of Coherent Elastic Neutrino-Nucleus Scattering. *Science*, 357(6356):1123–1126, 2017.

[A$^+$17d] E. Aprile et al. The XENON1T Dark Matter Experiment. *Eur. Phys. J. C*, 77(12):881, 2017.

[A$^+$18a] P. Agnes et al. Low-Mass Dark Matter Search with the DarkSide-50 Experiment. *Phys. Rev. Lett.*, 121(8):081307, 2018.

[A$^+$18b] C. Alduino et al. Study of Rare Nuclear Processes with CUORE. *Int.J.Mod.Phys.A*, 33(09):1843002, 2018.

[A$^+$18c] Q. Arnaud et al. First results from the NEWS-G direct dark matter search experiment at the LSM. *Astropart. Phys.*, 97:54–62, 2018.

[A$^+$19] D. Akimov et al. First Constraint on Coherent Elastic Neutrino-Nucleus Scattering in Argon. *Phys.Rev.D*, 100(11):115020, 2019.

[A$^+$20a] D.S. Akerib et al. The LUX-ZEPLIN (LZ) Experiment. *Nucl. Instrum. Meth. A*, 953:163047, 2020.

[A$^+$20b] D. Akimov et al. First Detection of Coherent Elastic Neutrino-Nucleus Scattering on Argon. 3 2020.

[A$^+$20c] D. Yu Akimov et al. First ground-level laboratory test of the two-phase xenon emission detector RED-100. *JINST*, 15(02):P02020, 2020.

[A$^+$20d] A. Aliane et al. First test of a Li_2WO_4(Mo) bolometric detector for the measurement of coherent neutrino-nucleus scattering. *Nucl.Instrum.Meth.A*, 949:162784, 2020.

[AA$^+$a] A.A. Aguilar-Arevalo et al. Fundamental Neutrino Physics at the Lujan Center.

[AA$^+$b] Alexis Aguilar-Arevalo et al. Search for light mediators in the low-energy data of the CONNIE reactor neutrino experiment.

[AA$^+$16] A. Aguilar-Arevalo et al. The CONNIE experiment. In *The CONNIE experiment*, volume 761, page 012057, 2016.

[AA$^+$19] Alexis Aguilar-Arevalo et al. Exploring low-energy neutrino physics with the Coherent Neutrino Nucleus Interaction Experiment. *Phys.Rev.D*, 100(9):092005, 2019.

[AALV18] Evgeny Akhmedov, Giorgio Arcadi, Manfred Lindner, and Stefan Vogl. Coherent scattering and macroscopic coherence: Implications for neutrino, dark matter and axion detection. *JHEP*, 10:045, 2018.

[ABB$^+$19] D.Yu. Akimov, V.A. Belov, A. Bolozdynya, Yu.V. Efremenko, A.M. Konovalov, A.V. Kumpan, D.G. Rudik, V.V. Sosnovtsev, A.V. Khromov, and A.V. Shakirov. Coherent elastic neutrino scattering on atomic nucleus: recently discovered type of low-energy neutrino interaction. *Phys.Usp.*, 62(2):166–178, 2019.

[ADD+18] Mohammad Abdullah, James B. Dent, Bhaskar Dutta, Gordon L. Kane, Shu Liao, and Louis E. Strigari. Coherent elastic neutrino nucleus scattering as a probe of a Z through kinetic and mass mixing effects. *Phys.Rev.D*, 98(1):015005, 2018.

[ADSZJ15] S. Arceo-Daz, K.-P. Schrder, K. Zuber, and D. Jack. Constraint on the magnetic dipole moment of neutrinos by the tip-RGB luminosity in ω-Centauri. *Astropart. Phys.*, 70:1–11, 2015.

[AE03] F.T. Avignone and Yu.V. Efremenko. Neutrino nucleus cross-section measurements at intense, pulsed spallation sources. *J.Phys.G*, 29:2615–2628, 2003.

[AIIN14] Amin Aboubrahim, Tarek Ibrahim, Ahmad Itani, and Pran Nath. Large Neutrino Magnetic Dipole Moments in MSSM Extensions. *Phys.Rev.D*, 89(5):055009, 2014.

[AP] I. Alikhanov and E.A. Paschos. A simple gauge model with Majorana neutrinos.

[ASDLS19] D. Aristizabal Sierra, Bhaskar Dutta, Shu Liao, and Louis E. Strigari. Coherent elastic neutrino-nucleus scattering in multi-ton scale dark matter experiments: Classification of vector and scalar interactions new physics signals. *JHEP*, 12:124, 2019.

[ASDRR18] D. Aristizabal Sierra, Valentina De Romeri, and N. Rojas. COHERENT analysis of neutrino generalized interactions. *Phys.Rev.D*, 98:075018, 2018.

[ASDRR19] D. Aristizabal Sierra, V. De Romeri, and N. Rojas. CP violating effects in coherent elastic neutrino-nucleus scattering processes. *JHEP*, 09:069, 2019.

[ASRT18] D. Aristizabal Sierra, N. Rojas, and M.H.G. Tytgat. Neutrino non-standard interactions and dark matter searches with multi-ton scale detectors. *JHEP*, 03:197, 2018.

[ATZ19] Wolfgang Altmannshofer, Michele Tammaro, and Jure Zupan. Non-standard neutrino interactions and low energy experiments. *JHEP*, 09:083, 2019.

[B+] D. Baxter et al. Coherent Elastic Neutrino-Nucleus Scattering at the European Spallation Source.

[B+14] S.J. Brice et al. A method for measuring coherent elastic neutrino-nucleus scattering at a far off-axis high-energy neutrino beam target. *Phys.Rev.D*, 89(7):072004, 2014.

[B+17] J. Billard et al. Coherent Neutrino Scattering with Low Temperature Bolometers at Chooz Reactor Complex. *J. Phys. G*, 44(10):105101, 2017.

[B+20] C. Buck et al. A novel experiment for coherent elastic neutrino nucleus scattering: CONUS. In *A novel experiment for coherent elastic neutrino nucleus scattering: CONUS*, volume 1342, page 012094, 2020.

[Bal18] A.B. Balantekin. Facets of Neutrino-Nucleus Interactions. In *Facets of Neutrino-Nucleus Interactions*, volume 49, page 221, 2018.

[BBC+06] C. Braggio, G. Bressi, G. Carugno, E. Feltrin, and G. Galeazzi. Massive silicon or germanium detectors at cryogenic temperature. In *Massive silicon or germanium detectors at cryogenic temperature*, volume 568, pages 412–415, 2006.

[BBE+12] A.G. Beda, V.B. Brudanin, V.G. Egorov, D.V. Medvedev, V.S. Pogosov, M.V. Shirchenko, and A.S. Starostin. The results of search for the neutrino magnetic moment in GEMMA experiment. *Adv.High Energy Phys.*, 2012:350150, 2012.

[BBFF+18] N. Bastidon, J. Billard, E. Figueroa-Feliciano, S. Heine, Z. Hong, and H.D. Pinckney. Optimizing Thermal Detectors for Low-Threshold Applications in Neutrino and Dark Matter Experiments. In *Optimizing Thermal Detectors for Low-Threshold Applications in Neutrino and Dark Matter Experiments*, volume 193, pages 1206–1213, 2018.

[BBG+] Adam Bernstein, Nathaniel Bowden, Bethany L. Goldblum, Patrick Huber, Igor Jovanovic, and John Mattingly. Neutrino Detectors as Tools for Nuclear Security.

[BBG+07] A. Bondar, A. Buzulutskov, A. Grebenuk, D. Pavlyuchenko, R. Snopkov, Y. Tikhonov, V.A. Kudryavtsev, P.K. Lightfoot, and N.J.C. Spooner. A Two-phase argon avalanche detector operated in a single electron counting mode. *Nucl.Instrum.Meth.A*, 574:493–499, 2007.

[BBH19] Jeffrey M. Berryman, Vedran Brdar, and Patrick Huber. Particle physics origin of the 5 MeV bump in the reactor antineutrino spectrum? *Phys.Rev.D*, 99(5):055045, 2019.

[BBR18] Heerak Banerjee, Pritibhajan Byakti, and Sourov Roy. Supersymmetric gauged U(1)$\_L\_\mu - L\_\tau$ model for neutrinos and the muon $(g-2)$ anomaly. *Phys.Rev.D*, 98(7):075022, 2018.

[BCDN+19] C. Bellenghi, D. Chiesa, L. Di Noto, M. Pallavicini, E. Previtali, and M. Vignati. Coherent elastic nuclear scattering of^{51} Cr neutrinos. *Eur.Phys.J.C*, 79(9):727, 2019.

[BCM+19] C. Bhm, D.G. Cerdeo, P.A.N. Machado, A. Olivares-Del Campo, E. Perdomo, and E. Reid. How high is the neutrino floor? *JCAP*, 01:043, 2019.

[BCRM+05] Nicole F. Bell, Vincenzo Cirigliano, Michael J. Ramsey-Musolf, Petr Vogel, and Mark B. Wise. How magnetic is the Dirac neutrino? *Phys.Rev.Lett.*, 95:151802, 2005.

[BCT07] P.S. Barbeau, J.I. Collar, and O. Tench. Large-Mass Ultra-Low Noise Germanium Detectors: Performance and Applications in Neutrino and Astroparticle Physics. *JCAP*, 09:009, 2007.

[BD+19] P.S. Bhupal Dev et al. Neutrino Non-Standard Interactions: A Status Report. In *Neutrino Non-Standard Interactions: A Status Report*, volume 2, page 001, 2019.

[BDN+20] Nicole F. Bell, James B. Dent, Jayden L. Newstead, Subir Sabharwal, and Thomas J. Weiler. Migdal effect and photon bremsstrahlung in effective field theories of dark matter direct detection and coherent elastic neutrino-nucleus scattering. *Phys.Rev.D*, 101(1):015012, 2020.

[BFJ20] Martin Bauer, Patrick Foldenauer, and Joerg Jaeckel. Hunting All the Hidden Photons. *JHEP*, 18:094, 2020.

[BHM] Carlos Blanco, Dan Hooper, and Pedro Machado. Constraining Sterile Neutrino Interpretations of the LSND and MiniBooNE Anomalies with Coherent Neutrino Scattering Experiments.

[BJK18] Julien Billard, Joseph Johnston, and Bradley J. Kavanagh. Prospects for exploring New Physics in Coherent Elastic Neutrino-Nucleus Scattering. *JCAP*, 11:016, 2018.

[BMR05] J. Barranco, O.G. Miranda, and T.I. Rashba. Probing new physics with coherent neutrino scattering off nuclei. *JHEP*, 12:021, 2005.

[BMR07] J. Barranco, O.G. Miranda, and T.I. Rashba. Low energy neutrino experiments sensitivity to physics beyond the Standard Model. *Phys.Rev.D*, 76:073008, 2007.

[BN19] Vadim A. Bednyakov and Dmitry V. Naumov. On coherent neutrino and antineutrino scattering off nuclei. *Phys.Part.Nucl.Lett.*, 16(6):638–646, 2019.

[BR19] Ingolf Bischer and Werner Rodejohann. General neutrino interactions from an effective field theory perspective. *Nucl.Phys.B*, 947:114746, 2019.

[BRX18a] Ingolf Bischer, Werner Rodejohann, and Xun-Jie Xu. Loop-induced Neutrino Non-Standard Interactions. *JHEP*, 10:096, 2018.

[BRX18b] Vedran Brdar, Werner Rodejohann, and Xun-Jie Xu. Producing a new Fermion in Coherent Elastic Neutrino-Nucleus Scattering: from Neutrino Mass to Dark Matter. *JHEP*, 12:024, 2018.

[BSFF14] J. Billard, L. Strigari, and E. Figueroa-Feliciano. Implication of neutrino backgrounds on the reach of next generation dark matter direct detection experiments. *Phys. Rev. D*, 89(2):023524, 2014.

[CA13] V. Chepel and H. Araujo. Liquid noble gas detectors for low energy particle physics. *JINST*, 8:R04001, 2013.

[CAL] G. Co', M. Anguiano, and A.M. Lallena. Nuclear structure uncertainties in coherent elastic neutrino-nucleus scattering.

[CD19] Matteo Cadeddu and Francesca Dordei. Reinterpreting the weak mixing angle from atomic parity violation in view of the Cs neutron rms radius measurement from COHERENT. *Phys.Rev.D*, 99(3):033010, 2019.

[CDG+19] M. Cadeddu, F. Dordei, C. Giunti, K.A. Kouzakov, E. Picciau, and A.I. Studenikin. Potentialities of a low-energy detector based on ^{4}He evaporation to observe atomic effects in coherent neutrino scattering and physics perspectives. *Phys.Rev.D*, 100(7):073014, 2019.

[CDGG+17] Pilar Coloma, Peter B. Denton, M.C. Gonzalez-Garcia, Michele Maltoni, and Thomas Schwetz. Curtailing the Dark Side in Non-Standard Neutrino Interactions. *JHEP*, 04:116, 2017.

[CEAA17] Marisol Chvez-Estrada and Alexis A. Aguilar-Arevalo. Potential of CCDs for the study of sterile neutrino oscillations via Coherent Neutrino-Nucleus Elastic Scattering. In *Potential of CCDs for the study of sterile neutrino oscillations via Coherent Neutrino-Nucleus Elastic Scattering*, volume 912, page 012031, 2017.

[CEFT18] Emilio Ciuffoli, Jarah Evslin, Qiang Fu, and Jian Tang. Extracting nuclear form factors with coherent neutrino scattering. *Phys.Rev.D*, 97(11):113003, 2018.

[CEGGM] Pilar Coloma, Ivan Esteban, M.C. Gonzalez-Garcia, and Michele Maltoni. Improved global fit to Non-Standard neutrino Interactions using COHERENT energy and timing data.

[CFH+15] J.I. Collar, N.E. Fields, M. Hai, T.W. Hossbach, J.L. Orrell, C.T. Overman, G. Perumpilly, and B. Scholz. Coherent neutrino-nucleus scattering detection with a CsI[Na] scintillator at the SNS spallation source. *Nucl.Instrum.Meth.A*, 773:56–65, 2015.

[CGGMS17] Pilar Coloma, M.C. Gonzalez-Garcia, Michele Maltoni, and Thomas Schwetz. COHERENT Enlightenment of the Neutrino Dark Side. *Phys.Rev.D*, 96(11):115007, 2017.

[CGK+] Matteo Cadeddu, Carlo Giunti, Konstantin A. Kouzakov, Yufeng Li, Alexander I. Studenikin, and Yiyu Zhang. Constraints on neutrino millicharge and charge radius from neutrino-atom scattering. In *Constraints on neutrino millicharge and charge radius from neutrino-atom scattering*.

[CGK+18] M. Cadeddu, C. Giunti, K.A. Kouzakov, Y.F. Li, A.I. Studenikin, and Y.Y. Zhang. Neutrino Charge Radii from COHERENT Elastic Neutrino-Nucleus Scattering. *Phys.Rev.D*, 98(11):113010, 2018.

[CGLZ18a] M. Cadeddu, C. Giunti, Y.F. Li, and Y.Y. Zhang. Average CsI neutron density distribution from COHERENT data. *Phys.Rev.Lett.*, 120(7):072501, 2018.

[CGLZ18b] Matteo Cadeddu, Carlo Giunti, Yufeng Li, and Yiyu Zhang. Average CsI neutron density distribution from COHERENT data. In *Average CsI neutron density distribution from COHERENT data*, volume NuFACT2018, page 144. SISSA, 2018.

[CGMP18] B.C. Caas, E.A. Garcs, O.G. Miranda, and A. Parada. Future perspectives for a weak mixing angle measurement in coherent elastic neutrino nucleus scattering experiments. *Phys.Lett.B*, 784:159–162, 2018.

[CGN] Debajyoti Choudhury, Kirtiman Ghosh, and Saurabh Niyogi. Non-Standard Neutrino Interactions : Obviating Oscillation Experiments.

[CGN18] Debajyoti Choudhury, Kirtiman Ghosh, and Saurabh Niyogi. Probing nonstandard neutrino interactions at the LHC Run II. *Phys.Lett.B*, 784:248–254, 2018.

[Ciu] Emilio Ciuffoli. Measuring the Neutron Distribution from Coherent Elastic Neutrino Nucleus Scattering. In *Measuring the Neutron Distribution from Coherent Elastic Neutrino Nucleus Scattering*.

[CJWZ19] Wei Chao, Jian-Guo Jiang, Xuan Wang, and Xing-Yu Zhang. Direct Detections of Dark Matter in the Presence of Non-standard Neutrino Interactions. *JCAP*, 08:010, 2019.

[CKW85] Blas Cabrera, Lawrence M. Krauss, and Frank Wilczek. Bolometric Detection of Neutrinos. *Phys.Rev.Lett.*, 55:25, 1985.

[CN] We-Fu Chang and John N. Ng. KeV scale new fermion from a hidden sector.

[CPP18] Yanou Cui, Maxim Pospelov, and Josef Pradler. Signatures of Dark Radiation in Neutrino and Dark Matter Detectors. *Phys.Rev.D*, 97(10):103004, 2018.

[CS16] Pilar Coloma and Thomas Schwetz. Generalized mass ordering degeneracy in neutrino oscillation experiments. *Phys.Rev.D*, 94(5):055005, 2016. [Erratum: Phys.Rev.D 95, 079903 (2017)].

[CV18] Amlie Chatelain and Maria Cristina Volpe. Neutrino propagation in binary neutron star mergers in presence of nonstandard interactions. *Phys.Rev.D*, 97(2):023014, 2018.

[D$^+$86] J. Dorenbosch et al. Experimental Verification of the Universality of ν_e and ν_μ Coupling to the Neutral Weak Current. *Phys.Lett.B*, 180:303–307, 1986.

[D$^+$05] Z. Daraktchieva et al. Final results on the neutrino magnetic moment from the MUNU experiment. *Phys.Lett.B*, 615:153–159, 2005.

[DCP$^+$93] A.I. Derbin, A.V. Chernyi, L.A. Popeko, V.N. Muratova, G.A. Shishkina, and S.I. Bakhlanov. Experiment on anti-neutrino scattering by electrons at a reactor of the Rovno nuclear power plant. *JETP Lett.*, 57:768–772, 1993.

[DDL$^+$17] James B. Dent, Bhaskar Dutta, Shu Liao, Jayden L. Newstead, Louis E. Strigari, and Joel W. Walker. Probing light mediators at ultralow threshold energies with coherent elastic neutrino-nucleus scattering. *Phys.Rev.D*, 96(9):095007, 2017.

[DDL$^+$18] James B. Dent, Bhaskar Dutta, Shu Liao, Jayden L. Newstead, Louis E. Strigari, and Joel W. Walker. Accelerator and reactor complementarity in coherent neutrino-nucleus scattering. *Phys.Rev.D*, 97(3):035009, 2018.

[DDL+19] Alakabha Datta, Bhaskar Dutta, Shu Liao, Danny Marfatia, and Louis E. Strigari. Neutrino scattering and B anomalies from hidden sector portals. *JHEP*, 01:091, 2019.

[DFS18] Peter B. Denton, Yasaman Farzan, and Ian M. Shoemaker. Testing large non-standard neutrino interactions with arbitrary mediator mass after COHERENT data. *JHEP*, 07:037, 2018.

[DG20] Sacha Davidson and Martin Gorbahn. Charged lepton flavor change and nonstandard neutrino interactions. *Phys.Rev.D*, 101(1):015010, 2020.

[DLSS19] Bhaskar Dutta, Shu Liao, Samiran Sinha, and Louis E. Strigari. Searching for Beyond the Standard Model Physics with COHERENT Energy and Timing Data. *Phys.Rev.Lett.*, 123(6):061801, 2019.

[DMSW16] Bhaskar Dutta, Rupak Mahapatra, Louis E. Strigari, and Joel W. Walker. Sensitivity to Z-prime and nonstandard neutrino interactions from ultralow threshold neutrino-nucleus coherent scattering. *Phys.Rev.D*, 93(1):013015, 2016.

[DPGRS03] S. Davidson, C. Pena-Garay, N. Rius, and A. Santamaria. Present and future bounds on nonstandard neutrino interactions. *JHEP*, 03:011, 2003.

[DPR91] A.C. Dodd, E. Papageorgiu, and S. Ranfone. The Effect of a neutrino magnetic moment on nuclear excitation processes. *Phys.Lett.B*, 266:434–438, 1991.

[dPR15] Patrick deNiverville, Maxim Pospelov, and Adam Ritz. Light new physics in coherent neutrino-nucleus scattering experiments. *Phys.Rev.D*, 92(9):095005, 2015.

[DS84] A. Drukier and Leo Stodolsky. Principles and Applications of a Neutral Current Detector for Neutrino Physics and Astronomy. In *Principles and Applications of a Neutral Current Detector for Neutrino Physics and Astronomy*, pages 395–396, 1984.

[DS19] Bhaskar Dutta and Louis E. Strigari. Neutrino physics with dark matter detectors. *Ann.Rev.Nucl.Part.Sci.*, 69:137–161, 2019.

[EGGM+18] Ivan Esteban, M.C. Gonzalez-Garcia, Michele Maltoni, Ivan Martinez-Soler, and Jordi Salvado. Updated Constraints on Non-Standard Interactions from Global Analysis of Oscillation Data. *JHEP*, 08:180, 2018.

[EGGM19] Ivan Esteban, M.C. Gonzalez-Garcia, and Michele Maltoni. On the Determination of Leptonic CP Violation and Neutrino Mass Ordering in Presence of Non-Standard Interactions: Present Status. *JHEP*, 06:055, 2019.

[ESY18] Rouven Essig, Mukul Sholapurkar, and Tien-Tien Yu. Solar Neutrinos as a Signal and Background in Direct-Detection Experiments Searching for Sub-GeV Dark Matter With Electron Recoils. *Phys.Rev.D*, 97(9):095029, 2018.

[ESZ19] H. Ejiri, J. Suhonen, and K. Zuber. Neutrinonuclear responses for astro-neutrinos, single beta decays and double beta decays. *Phys.Rept.*, 797:1–102, 2019.

[Far] Y. Farzan. A model for lepton flavor violating non-standard neutrino interactions.

[FC98] Gary J. Feldman and Robert D. Cousins. A Unified approach to the classical statistical analysis of small signals. *Phys.Rev.D*, 57:3873–3889, 1998.

[FGM18] L.J. Flores, E.A. Garcs, and O.G. Miranda. Exploring NSI degeneracies in long-baseline experiments. *Phys.Rev.D*, 98(3):035030, 2018.

[FLM$^+$02] G.L. Fogli, E. Lisi, A. Marrone, D. Montanino, and A. Palazzo. Getting the most from the statistical analysis of solar neutrino oscillations. *Phys.Rev.D*, 66:053010, 2002.

[FLN19] Francesco Forastieri, Massimiliano Lattanzi, and Paolo Natoli. Cosmological constraints on neutrino self-interactions with a light mediator. *Phys.Rev.D*, 100(10):103526, 2019.

[FLRX18] Yasaman Farzan, Manfred Lindner, Werner Rodejohann, and Xun-Jie Xu. Probing neutrino coupling to a light scalar with coherent neutrino scattering. *JHEP*, 05:066, 2018.

[Fre74] Daniel Z. Freedman. Coherent Neutrino Nucleus Scattering as a Probe of the Weak Neutral Current. *Phys.Rev.D*, 9:1389–1392, 1974.

[FT18] Y. Farzan and M. Tortola. Neutrino oscillations and Non-Standard Interactions. *Front.in Phys.*, 6:10, 2018.

[G$^+$15] G.K. Giovanetti et al. A Dark Matter Search with MALBEK. *Phys. Procedia*, 61:77–84, 2015.

[GCMP17] Estela Garcs, Blanca Caas, Omar Miranda, and Alexander Parada. Neutrino scattering and the reactor antineutrino anomaly. In *Neutrino scattering and the reactor antineutrino anomaly*, volume 934, page 012004, 2017.

[GG19] M.C. Gonzalez-Garcia. Neutrino Masses and Mixing: A Little History for a Lot of Fun. In *Neutrino Masses and Mixing: A Little History for a Lot of Fun*, 2019.

[GGG+17] A. Giganon, I. Giomataris, M. Gros, I. Katsioulas, X.F. Navick, G. Tsiledakis, I. Savvidis, A. Dastgheibi-Fard, and A. Brossard. A multiball read-out for the spherical proportional counter. *JINST*, 12(12):P12031, 2017.

[GGMPGZF18] M.C. Gonzalez-Garcia, Michele Maltoni, Yuber F. Perez-Gonzalez, and Renata Zukanovich Funchal. Neutrino Discovery Limit of Dark Matter Direct Detection Experiments in the Presence of Non-Standard Interactions. *JHEP*, 07:019, 2018.

[Giu] C. Giunti. General COHERENT Constraints on Neutrino Non-Standard Interactions.

[GR18] Andrea Gallo Rosso. Searching for supernova neutrinos with dark matter detectors. In *Searching for supernova neutrinos with dark matter detectors*, volume NEUTEL2017, page 075. SISSA, 2018.

[gra] https://grafana.com/grafana/.

[GS15] Carlo Giunti and Alexander Studenikin. Neutrino electromagnetic interactions: a window to new physics. *Rev.Mod.Phys.*, 87:531, 2015.

[GS18] Shao-Feng Ge and Ian M. Shoemaker. Constraining Photon Portal Dark Matter with Texono and Coherent Data. *JHEP*, 11:066, 2018.

[GTW18] Graciela B. Gelmini, Volodymyr Takhistov, and Samuel J. Witte. Casting a Wide Signal Net with Future Direct Dark Matter Detection Experiments. *JCAP*, 07:009, 2018. [Erratum: JCAP 02, E02 (2019)].

[GTW19] Graciela B. Gelmini, Volodymyr Takhistov, and Samuel J. Witte. Geoneutrinos in Large Direct Detection Experiments. *Phys.Rev.D*, 99(9):093009, 2019.

[HC19] Xu-Run Huang and Lie-Wen Chen. Neutron Skin in CsI and Low-Energy Effective Weak Mixing Angle from COHERENT Data. *Phys.Rev.D*, 100(7):071301, 2019.

[HCM03] Charles J. Horowitz, K.J. Coakley, and D.N. McKinsey. Supernova observation via neutrino - nucleus elastic scattering in the CLEAN detector. *Phys.Rev.D*, 68:023005, 2003.

[HKM12] Roni Harnik, Joachim Kopp, and Pedro A.N. Machado. Exploring nu Signals in Dark Matter Detectors. *JCAP*, 07:026, 2012.

[HLLM19] Tao Han, Jiajun Liao, Hongkai Liu, and Danny Marfatia. Non-standard neutrino interactions at COHERENT, DUNE, T2HK and LHC. *JHEP*, 11:028, 2019.

[HLRV19] Julian Heeck, Manfred Lindner, Werner Rodejohann, and Stefan Vogl. Non-Standard Neutrino Interactions and Neutral Gauge Bosons. *SciPost Phys.*, 6(3):038, 2019.

[inf] https://www.influxdata.com/products/influxdb-overview/.

[J+a] I. Jaegle et al. Compact, directional neutron detectors capable of high-resolution nuclear recoil imaging.

[J+b] A. Juillard et al. Low-noise HEMTs for Coherent Elastic Neutrino Scattering and Low-Mass Dark Matter Cryogenic Semiconductor Detectors. In *Low-noise HEMTs for Coherent Elastic Neutrino Scattering and Low-Mass Dark Matter Cryogenic Semiconductor Detectors*.

[JVDN19] Natalie Jachowicz, Nils Van Dessel, and Alexis Nikolakopoulos. Low-energy neutrino scattering in experiment and astrophysics. *J.Phys.G*, 46(8):084003, 2019.

[KFK19] Tetiana Kozynets, Scott Fallows, and Carsten B. Krauss. Sensitivity of the PICO-500 Bubble Chamber to Supernova Neutrinos Through Coherent Nuclear Elastic Scattering. *Astropart.Phys.*, 105:25–30, 2019.

[KM73] Makoto Kobayashi and Toshihide Maskawa. CP Violation in the Renormalizable Theory of Weak Interaction. *Prog. Theor. Phys.*, 49:652–657, 1973.

[KMP+15] T.S. Kosmas, O.G. Miranda, D.K. Papoulias, M. Tortola, and J.W.F. Valle. Probing neutrino magnetic moments at the Spallation Neutron Source facility. *Phys.Rev.D*, 92(1):013011, 2015.

[KN99] Spencer Klein and Joakim Nystrand. Exclusive vector meson production in relativistic heavy ion collisions. *Phys.Rev.C*, 60:014903, 1999.

[KPTV17] T.S. Kosmas, D.K. Papoulias, M. Tortola, and J.W.F. Valle. Probing light sterile neutrino signatures at reactor and Spallation Neutron Source neutrino experiments. *Phys.Rev.D*, 96(6):063013, 2017.

[Kra91] Lawrence M. Krauss. Low-energy neutrino detection and precision tests of the standard model. *Phys.Lett.B*, 269:407–411, 1991.

[L$^+$04] D.W. Liu et al. Limits on the neutrino magnetic moment using 1496 days of Super-Kamiokande-I solar neutrino data. *Phys.Rev.Lett.*, 93:021802, 2004.

[L$^+$18] A. Leder et al. Unfolding Neutron Spectrum with Markov Chain Monte Carlo at MIT Research Reactor with He-3 Neutral Current Detectors. *JINST*, 13(02):P02004, 2018.

[L$^+$19] B.G. Lenardo et al. Low-Energy Physics Reach of Xenon Detectors for Nuclear-Recoil-Based Dark Matter and Neutrino Experiments. *Phys.Rev.Lett.*, 123(23):231106, 2019.

[LA19] E. Lopez Asamar. SuperCDMS SNOLAB: status and prospects for measuring the coherent neutrino scattering. *J. Phys. Conf. Ser.*, 1216(1):012020, 2019.

[Lan19] Rafael F. Lang. Versatile Physics with Liquid Xenon Dark Matter Detectors. In *Versatile Physics with Liquid Xenon Dark Matter Detectors*, volume 56, pages 97–102, 2019.

[Li19] Yu-Feng Li. First average CsI neutron radius from the coherent elastic neutrino-nucleus scattering. In *First average CsI neutron radius from the coherent elastic neutrino-nucleus scattering*, volume ICHEP2018, page 341. SISSA, 2019.

[LM17] Jiajun Liao and Danny Marfatia. COHERENT constraints on nonstandard neutrino interactions. *Phys.Lett.B*, 775:54–57, 2017.

[LM18] Jiajun Liao and Danny Marfatia. Constraints on nonstandard neutrino interactions from the COHERENT experiment. In *Constraints on nonstandard neutrino interactions from the COHERENT experiment*, volume NuFact2017, page 142. SISSA, 2018.

[LMR$^+$16] Rafael F. Lang, Christopher McCabe, Shayne Reichard, Marco Selvi, and Irene Tamborra. Supernova neutrino physics with xenon dark matter detectors: A timely perspective. *Phys. Rev. D*, 94(10):103009, 2016.

[LV10] R. Lazauskas and C. Volpe. Low energy neutrino scattering measurements at future Spallation Source facilities. *J.Phys.G*, 37(12):125101, 2010. [Erratum: J.Phys.G 42, 059501 (2015)].

[M+11] Th.A. Mueller et al. Improved Predictions of Reactor Antineutrino Spectra. *Phys. Rev. C*, 83:054615, 2011.

[M+19] J.L. Ma et al. Study on cosmogenic activation in germanium detectors for future tonne-scale CDEX experiment. *Sci.China Phys.Mech.Astron.*, 62(1):11011, 2019.

[MDCSD19] Clio Marques, G.S. Dias, H.H. Chavez Sanchez, and Srgio Barbosa Duarte. Searching signature of neutrino-nucleus coherent scattering with Mssbauer Spectroscopy. In *Searching signature of neutrino-nucleus coherent scattering with Mssbauer Spectroscopy*, volume 1291, page 012018, 2019.

[MPTV] Omar G. Miranda, Dimitrios K. Papoulias, Mariam Trtola, and Jos W.F. Valle. Probing new neutral gauge bosons with CEvNS and neutrino-electron scattering.

[MPTV19] O.G. Miranda, D.K. Papoulias, M. Trtola, and J.W.F. Valle. Probing neutrino transition magnetic moments with coherent elastic neutrino-nucleus scattering. *JHEP*, 07:103, 2019.

[MRSV18] Alexander Millar, Georg Raffelt, Leo Stodolsky, and Edoardo Vitagliano. Neutrino mass from bremsstrahlung endpoint in coherent scattering on nuclei. *Phys.Rev.D*, 98(12):123006, 2018.

[MSGS19] O.G. Miranda, G. Sanchez Garcia, and O. Sanders. Coherent elastic neutrino-nucleus scattering as a precision test for the Standard Model and beyond: the COHERENT proposal case. *Adv.High Energy Phys.*, 2019:3902819, 2019.

[MTV06] O.G. Miranda, M.A. Tortola, and J.W.F. Valle. Are solar neutrino oscillations robust? *JHEP*, 10:008, 2006.

[MWL+] Yossi Mosbacher, Micha Weiss, Hagar Landsman, Nadav Priel, Ilan Eliyahu, Arik Kreisel, Offir Ozeri, David Hershkovich, Ori Cheshnovsky, and Ranny Budnik. Wide band spectroscopic response of monocrystallines to low dose neutron and gamma radiation.

[NBPR17] Kenny C. Y. Ng, John F. Beacom, Annika H. G. Peter, and Carsten Rott. Solar Atmospheric Neutrinos: A New Neutrino Floor for Dark Matter Searches. *Phys.Rev.D*, 96(10):103006, 2017.

[Ota18] Toshihiko Ota. Beyond Standard Neutrino Theory. In *Beyond Standard Neutrino Theory*, volume NuFact2017, page 026. SISSA, 2018.

[Par] Alexander Parada. Constraints on neutrino electric millicharge from experiments of elastic neutrino-electron interaction and future experimental proposals involving coherent elastic neutrino-nucleus scattering.

[PEMS12] Kelly Patton, Jonathan Engel, Gail C. McLaughlin, and Nicolas Schunck. Neutrino-nucleus coherent scattering as a probe of neutron density distributions. *Phys.Rev.C*, 86:024612, 2012.

[PK18] D.K. Papoulias and T.S. Kosmas. COHERENT constraints to conventional and exotic neutrino physics. *Phys.Rev.D*, 97(3):033003, 2018.

[PKK19] D.K. Papoulias, T.S. Kosmas, and Y. Kuno. Recent probes of standard and non-standard neutrino physics with nuclei. *Front.in Phys.*, 7:191, 2019.

[PKR19] Sujata Pandey, Siddhartha Karmakar, and Subhendu Rakshit. Strong constraints on non-standard neutrino interactions: LHC vs. IceCube. *JHEP*, 11:046, 2019.

[PKS+20] D.K. Papoulias, T.S. Kosmas, R. Sahu, V.K.B. Kota, and M. Hota. Constraining nuclear physics parameters with current and future COHERENT data. *Phys.Lett.B*, 800:135133, 2020.

[PSK+18] D.K. Papoulias, R. Sahu, T.S. Kosmas, V.K.B. Kota, and B. Nayak. Novel neutrino-floor and dark matter searches with deformed shell model calculations. *Adv.High Energy Phys.*, 2018:6031362, 2018.

[PSY18] P. Pirinen, J. Suhonen, and E. Ydrefors. Neutral-current neutrino-nucleus scattering off Xe isotopes. *Adv.High Energy Phys.*, 2018:9163586, 2018.

[Raj] Nirmal Raj. Neutrinos from Type Ia and failed core-collapse supernovae at dark matter detectors.

[Raj90] Subhash Rajpoot. DIRAC NEUTRINO MAGNETIC MOMENTS IN THE LEFT-RIGHT SYMMETRIC MODEL. *Phys.Lett.B*, 237:77–80, 1990.

[RD88] Georg G. Raffelt and David S.P. Dearborn. Bounds on Weakly Interacting Particles From Observational Lifetimes of Helium Burning Stars. *Phys. Rev. D*, 37:549–551, 1988.

[Ric17] Grayson Currie Rich. *Measurement of Low-Energy Nuclear-Recoil Quenching Factors in CsI[Na] and Statistical Analysis of the First Observation of Coherent, Elastic Neutrino-Nucleus Scattering*. PhD thesis, North Carolina U., 2017.

[Rit17] Adam Ritz. Probing light dark sectors with coherent neutrino-nucleus scattering. In *Probing light dark sectors with coherent neutrino-nucleus scattering*, volume NuFact2017, page 144. SISSA, 2017.

[Rot18] Johannes Rothe. CEνNS at the low-energy frontier in NU-CLEUS. In *CEνNS at the low-energy frontier in NU-CLEUS*, volume NOW2018, page 092. SISSA, 2018.

[RTW] Nirmal Raj, Volodymyr Takhistov, and Samuel J. Witte. Pre-Supernova Neutrinos in Large Dark Matter Direct Detection Experiments.

[S$^+$01] R. Schwienhorst et al. A New upper limit for the tau - neutrino magnetic moment. *Phys.Lett.B*, 513:23–29, 2001.

[S$^+$16] A.K. Soma et al. Characterization and Performance of Germanium Detectors with sub-keV Sensitivities for Neutrino and Dark Matter Experiments. *Nucl. Instrum. Meth. A*, 836:67–82, 2016.

[S$^+$17] R. Strauss et al. The ν-cleus experiment: A gram-scale fiducial-volume cryogenic detector for the first detection of coherent neutrino-nucleus scattering. *Eur. Phys. J. C*, 77:506, 2017.

[SBKC19] T. Suzuki, A.B. Balantekin, T. Kajino, and S. Chiba. Neutrino-13C Cross Sections at Supernova Neutrino Energies. *J.Phys.G*, 46(7):075103, 2019.

[Sch06] Kate Scholberg. Prospects for measuring coherent neutrino-nucleus elastic scattering at a stopped-pion neutrino source. *Phys.Rev.D*, 73:033005, 2006.

[Sch12] Kate Scholberg. Supernova Neutrino Detection. *Ann.Rev.Nucl.Part.Sci.*, 62:81–103, 2012.

[Sch17] Bjorn Jorg Scholz. *First Observation of Coherent Elastic Neutrino-Nucleus Scattering*. PhD thesis, Chicago U., 2017.

[Sch19] Marc Schumann. Direct Detection of WIMP Dark Matter: Concepts and Status. *J. Phys. G*, 46(10):103003, 2019.

[Ser16] Aldo Serenelli. Alive and well: a short review about standard solar models. *Eur. Phys. J. A*, 52(4):78, 2016.

[Sin13] V.V. Sinev. Experimental spectrum of reactor antineutrinos and spectra of main fissile isotopes. *Phys. Atom. Nucl.*, 76:537–543, 2013.

[snb] Made by Erin Conley for internal DUNE use based on information in https://arxiv.org/pdf/1712.05584.pdf.

[SRPS20] R. Strauss, J. Rothe, F. Petricca, and S. Schnert. The -cleus experiment: Gram-scale cryogenic calorimeters for a discovery of coherent neutrino scattering. In *The -cleus experiment: Gram-scale cryogenic calorimeters for a discovery of coherent neutrino scattering*, volume 1342, page 012132, 2020.

[Sta06] I. Stancu. Low-energy neutrino cross-section measurements at SNS. In *Low-energy neutrino cross-section measurements at SNS*, volume 155, pages 251–253, 2006.

[STK19] J. Sinatkas, V. Tsaktsara, and Odysseas Kosmas. Simulated neutrino signals of low and intermediate energy neutrinos on Cd detectors. *Front.in Phys.*, 7:42, 2019.

[Stua] Alexander Studenikin. Electromagnetic neutrinos: New constraints and new effects in oscillations. In *Electromagnetic neutrinos: New constraints and new effects in oscillations.*

[Stub] Alexander Studenikin. Electromagnetic properties of neutrinos. In *Electromagnetic properties of neutrinos.*

[SW20] Lakhwinder Singh and H.T. Wong. Studies of neutrino interactions at the Kuo-Sheng Neutrino Laboratory with sub-keV Ge-detectors. In *Studies of neutrino interactions at the Kuo-Sheng Neutrino Laboratory with sub-keV Ge-detectors*, volume 1342, page 012078, 2020.

[T$^+$18] M. Tanabashi et al. Review of Particle Physics. *Phys.Rev.D*, 98(3):030001, 2018.

[Tay18] R. Tayloe. The CENNS-10 Liquid Argon Detector to measure CEvNS at the Spallation Neutron Source. In *The CENNS-10 Liquid Argon Detector to measure CEvNS at the Spallation Neutron Source*, volume 13, page C04005, 2018.

[VCS$^+$13] Nicols Viaux, Mrcio Catelan, Peter B. Stetson, Georg Raffelt, Javier Redondo, Aldo A. R. Valcarce, and Achim Weiss. Particle-physics constraints from the globular cluster M5: Neutrino Dipole Moments. *Astron. Astrophys.*, 558:A12, 2013.

[VE89] P. Vogel and J. Engel. Neutrino Electromagnetic Form-Factors. *Phys.Rev.D*, 39:3378, 1989.

[VVG+92] G.S. Vidyakin, V.N. Vyrodov, I.I. Gurevich, Yu.V. Kozlov, V.P. Martemyanov, S.V. Sukhotin, V.G. Tarasenkov, E.V. Turbin, and S.Kh. Khakhimov. Limitations on the magnetic moment and charge radius of the electron-anti-neutrino. *JETP Lett.*, 55:206–210, 1992.

[W+07] H.T. Wong et al. A Search of Neutrino Magnetic Moments with a High-Purity Germanium Detector at the Kuo-Sheng Nuclear Power Station. *Phys.Rev.D*, 75:012001, 2007.

[Wan18] Tse-Chun Wang. *New Physics at the Neutrino Oscillation Frontier*. PhD thesis, Durham U., 2018.

[Won15] Henry Tsz-King Wong. Taiwan EXperiment On NeutrinO History and Prospects. *The Universe*, 3(4):22–37, 2015.

[Xu19] Xun-Jie Xu. Tensor and scalar interactions of neutrinos may lead to observable neutrino magnetic moments. *Phys.Rev.D*, 99(7):075003, 2019.

[YHP19] Junjie Yang, Jesse A. Hernandez, and J. Piekarewicz. Electroweak probes of ground state densities. *Phys.Rev.C*, 100(5):054301, 2019.